Research Square

Preprints are preliminary reports that have not undergone peer review.
They should not be considered conclusive, used to inform clinical practice,
or referenced by the media as validated information.

A periportal myeloid programme and a pericentral hepatocyte clock define spatially distinct axes of mouse liver ageing

Jinwei Li

1791605967@qq.com

Huazhong university of science and technology https://orcid.org/0009-0002-0171-020X

Article

Keywords:

Posted Date: November 26th, 2026

DOI: https://doi.org/10.21203/rs.3.rs-11805002/v1

License: This work is licensed under a Creative Commons Attribution 4.0 International License.
Read Full License

Additional Declarations: There is **NO** Competing Interest.

A periportal myeloid programme and a pericentral hepatocyte clock define spatially distinct axes of mouse liver ageing

Jinwei Li1,*

1Huazhong University of Science and Technology, Wuhan 430074, China

*e-mail: 1791605967@qq.com

Corresponding author: Jinwei Li (1791605967@qq.com). ORCID: 0009-0002-0171-020X.

Abstract

I found that liver myeloid ageing is spatially partitioned along the lobular axis in wild-type mice. In Stereo-seq sections, the myeloid module M06 was portal-enriched (donor-level rho −0.20, 95% CI −0.31 to −0.09, n=4; P=0.010), whereas the hepatocyte clock was central-enriched; the M06 gradient survived adjustment for myeloid abundance, cellularity and composition, and was strongest in aged portal bins. The hepatocyte clock ordered donors by age (leave-one-donor-out MAE 9.19 weeks, rho 0.949) and reproduced this ordering in independent cohorts (rho 0.895 and 0.928; meta r=0.911); it can serve as a relative age score but not as absolute age calibration. Its 310-gene signature mapped mainly to M01/M12, M08, M21, M03 and M14, tracked age in 13/15 brain regions, and was strongly associated with a late SASP programme tracked by M06 (r=0.96). The clock gradient was sensitive to spot cellularity. These results define a spatially organised myeloid–clock axis in mouse liver ageing.

Introduction

Ageing reshapes the liver through cell-intrinsic programmes and through shifts in cell-type composition [1–3], but how these changes are organised along the lobular axis remains incompletely resolved. Systemic and blood-based age clocks have been developed [4,5]. Human liver spatial and single-cell proteomic atlases have begun to resolve zonation [6–8,11,12]. The SASP is a candidate ageing programme, but its cellular source, module carrier and relation to clocks remain unresolved. Most liver clocks are tested in one cohort, whereas cell-type-specific brain clocks have been developed [9], and cross-organ transfer and layer specificity are rarely examined together. I reanalysed a single-nucleus RNA/ATAC atlas at the donor level across five ages, together with independent bulk cohorts and a 15-region mouse brain atlas, to separate three axes: a rank-accurate transcriptomic clock, a stable gene set containing the M08/M14 modules, and a late myeloid M06–SASP programme. I separated cell types and compared like with like; the conclusions are supported by functional enrichment, multi-omics and cross-organ projection. Pharmacological reachability is mapped as a boundary and has not reached clinical validation.

Results

M06 and the clock occupy distinct hepatic zones

Using the continuous GSE328448 zonation score (Layer1 = central vein, Layer9 = portal vein) [6–8,10], the myeloid inflammatory module M06 increased from central to portal bins in every section (per-donor rho -0.25, -0.22, -0.24 and -0.10 in Y1, Y2, O1 and O2; donor-level mean -0.20, 95%

CI -0.31 to -0.09, n=4 sections, P=0.010, Cohen's d=-2.9; within-section coordinate-permutation P=0.001; Moran's I 0.24-0.38, permutation P=0.002). The gradient survived adjustment for myeloid abundance (-0.20, P=0.008), spot cellularity (nCount/nFeature; -0.23, P=0.016) and full composition (-0.19, P=0.025), whereas the independent myeloid marker score was flat (-0.01, P=0.76). The hepatocyte-adjusted clock score was pericentral (per-donor rho +0.20, +0.31, +0.29 and +0.24; mean +0.26, 95% CI +0.18 to +0.34, P=0.002; Moran's I 0.07-0.24), but this attenuated after further adjustment for spot cellularity (+0.07, P=0.11). M06-myeloid coupling was strongest in aged portal bins (rho 0.22-0.24 vs 0.16-0.19 in central bins). GSE328448 is Stereo-seq bin200, a multi-cell binned assay; these data therefore provide direct spatial observation of M06-myeloid co-localization, replacing the earlier NNLS-based inference, but do not assign M06 expression to individual cells (Fig. 1a–g). This is the lead finding; the following sections describe how the two scores were constructed.

A five-age, donor-resolved liver atlas

I reanalysed the public same-nucleus resource GSE328206 [13]: 40 mice, eight per age (four female, four male), 295,364 RNA and 248,949 post-QC ATAC nuclei (ED1, ED2). Age, sex and batch are shown in a donor oncoprint (Supplementary Fig. 26a); Batch 1 covers 13, 81 and 121.5 weeks and Batch 2 covers 53 and 105 weeks. The batch design is audited in the Supplementary Information, where its interpretative boundaries are stated. The 70,000-nucleus UMAP resolves eight major cell classes, and composition is shown as a row-z dot-heat with exact BH q values (Supplementary Fig. 26b–d). Hepatocyte fraction decreases with age (rho = -0.70; -0.27% per week). Joint RNA-ATAC coverage was rho = 0.95 (Supplementary Fig. 26e–g).

The analysis proceeds in five layers—data, audit, clock, external validation and decision—summarized in Supplementary Fig. 7; Table 1 separates the three external-validation levels (direction, effect reproducibility and absolute calibration).

A hepatocyte transcriptomic clock

Hepatocyte pseudobulk profiles were modelled with ElasticNet using top-variance genes and outer leave-one-donor-out validation; all preprocessing and tuning were inside the outer training folds (Fig. 3a) [14–15]. The clock achieved MAE 9.19 weeks, rho = 0.949 and R2 = 0.915 (Fig. 3b); LivAge, a published murine transcriptomic clock, provides external context [16]. A tree-based model in the fast benchmark reached a lower MAE but produced step-like predictions and lower rank correlation (Fig. 3c). Bland-Altman analysis showed a small global bias and age-dependent residuals. Within-animal UMI thinning produced no systematic score shift: the within-donor Spearman correlation between score and retained fraction was near zero (mean 0.09, median 0.00; Fig. 3g).

To test whether the clock's gene-level and pathway-level directions generalize, I recomputed full-transcriptome age rankings in GSE302188 and GSE262290 and ran the same Hallmark GSEA. Of 18 pathways significant in discovery, 17/18 retained direction in GSE302188 and 18/18 in GSE262290 (NES Spearman 0.86/0.82; Fig. 3i). The concordant set comprised down-regulation of oxidative phosphorylation, fatty-acid metabolism, adipogenesis, bile-acid metabolism, peroxisome and xenobiotic metabolism, and up-regulation of inflammatory response, IFN-α/γ, IL6/JAK/STAT3, IL2/STAT5, complement, allograft rejection, TNFα/NF-κB, apoptosis, hypoxia and p53 signalling; only protein secretion was discordant, and it was not significant externally. 154/195 (79.0%) and 155/196 (79.1%) of measured 310-gene clock genes matched direction (binomial P<1e-16; within-batch and within-run permutation P=0.002 and 0.008). M14 module

genes were 69.3%/70.8% concordant (Fig. 3j). Mup11 declined with age in both external cohorts (rho −0.78/−0.73; Fig. 3k).

Cross-organ projection into the brain

To test whether the liver age axis is liver-specific, I used the Hahn et al. mouse brain bulk atlas (GSE212336; 847 samples, 15 regions, seven ages 3-28 months). Region-specific RidgeCV clocks predicted age with R2 0.62-0.94 and MAE 1.4-3.4 months; corpus callosum was best and entorhinal cortex worst (Fig. 4g; Supplementary Fig. 4a). Cross-region transfer was partial and asymmetric: median off-diagonal R2 was 0.43 and 59 of 210 pairs had R2<0; per-source median transfer ranged from 0.73 (choroid plexus, posterior hippocampus) to -0.16 (motor cortex), and corpus callosum was the most predictable destination (0.79) whereas hypothalamus was the least (0.00) (Fig. 4h). The 310-gene liver signature mapped to 210 brain genes and was age-associated in 13/15 regions (median rho 0.49, range 0.19-0.65; Fig. 4i; Supplementary Fig. 4b); medulla, choroid plexus, motor cortex and corpus callosum were strongest (0.60-0.65), whereas hypothalamus (0.26, P=0.053) and olfactory bulb (0.19, P=0.16) did not reach P<0.05. Of the 210 genes, 85 were also brain clock genes, with Ctss, C4b, Tyrobp and C1q up and Gpr17 down in all 15 regions (Fig. 4j; Supplementary Fig. 4c).

External transfer is rank-level and coverage-limited

Frozen and target-domain-standardised scores were tested in four external mouse liver datasets: GSE327303, Nikopoulou E-MTAB-12579, TMS 10x and TMS ss2 [2,17–18]. Pooled cell-level AUC for old-versus-young separation was 0.62-0.80; periportal/pericentral values were 0.892/0.795 (Fig. 4b,c). The donor-level forward leave-one-dataset result was R2 0.875 and MAE 8.58 weeks (6 donors, two ages, target-domain scaling). Pseudo-donor and reference-pool analyses are shown in Fig. 4e,f. Cell-level absolute calibration failed in all eight cohort x mode evaluations: fitted slope 1.04-2.21, intercept -140 to +49 weeks, and MAE at or above the median-age baseline (ED12d).

Leave-one-design-out validation

Leave-one-age-group-out gave MAE 24.4 weeks, rho 0.65, calibration slope 1.75/intercept −51.8 weeks and nearest-group accuracy 0.20; held-out young and geriatric groups were biased +29.9 and −34.9 weeks. Leave-one-sex-out gave MAE 31.8 weeks and R^2 −0.13 (female→male 50.2 weeks; male→female 13.4 weeks). Leave-one-batch-out gave 24.5 weeks. Leave-one-zone-out gave 2.1 weeks, but zones share donors across folds, so this is a within-donor transfer check rather than a donor-independent validation and is not comparable with the 9.19-week leave-one-donor-out value (Supplementary Fig. 16).

Donor hierarchy, age trajectories, signature stability and module concordance

Donor identity accounted for 6.4% of score variance overall; hepatocyte zones 24.7%, Kupffer 13.9% and cholangiocyte 69.1% (Fig. 5f; Supplementary Fig. 17a). All cell types rose under the clock, with hepatocyte +108.5 and cholangiocyte +46.2 steepest and Kupffer +16.7 shallowest (Supplementary Fig. 17b,c). Trajectories were trait-specific: linear~quadratic for the clock, M08 saturating/quadratic, and M14 best with age+sex (Supplementary Fig. 18). Bootstrap selection retained 71/310 and 79/310 genes; M08 63.0%, M12 41.5%, M14 18.2% (Fig. 5i; Supplementary Fig. 19). This stability refers to clock-feature selection: M08 was the most stable module and is clock-enriched, whereas only 4/22 M14 members were repeatedly selected as clock features; M14's age coherence is a module-level property supported by its eigengene age association, external gene-direction concordance and RNA-ATAC coupling, independently of clock-feature

stability. Human-mouse module direction concordance was partial (GTEx 18.2-85.7%, HLiCA 12.5-69.2%); M14 retained partial support, M08 did not in HLiCA (Supplementary Fig. 20). Cell-level donor-block variance was 9.5% for the clock, 28.5% for M08 and 10.6% for M14 (Fig. 5h; Supplementary Fig. 24). Earlier retained analyses are summarized in ED10 and Supplementary Figs. 1 and 2; exploratory SEM [19], WGCNA [20], HALO [21], motif [22–23], communication [24–26] and network [27] analyses are reported in ED3, ED4 and Supplementary Fig. 29 as exploratory context.

Disease specificity and nuisance probes

Disease comparisons gave an AUC of 0.484 at the cell level (HFD versus chow), with animal-like groups spanning 0.28-0.96 (Supplementary Fig. 27d,e). Nuisance probes pointed in different directions (Supplementary Fig. 27f).

The age association is mainly composition-adjusted, not uniquely compositional

In hepatocyte pseudobulk, composition-only models explained R2 = 0.56, whereas the hepatocyte-pseudobulk state reached R2 ~ 0.91; a combined model did not improve on state alone (Fig. 5a). In conditional regressions, the state age coefficient remained significant after adjusting for hepatocyte fraction (94% retained), while the hepatocyte-fraction coefficient became non-significant after adjusting for state. The ablation raincloud showed that removing the canonical panel reduced its age association (rho 0.90 vs 0.28; Fig. 5b), and the 300-gene BH waterfall placed Mup11 at the family floor (BH q = 0.010; Supplementary Fig. 31c). Downsampling to 500 cells or 1,000 UMIs changed scale more than rank (Supplementary Fig. 31d). Five cell subsets gave Mup11 significance in 4/5 and Mup1 in 2/5. Cross-species transfer was weak (Fig. 5d).

Additional controls: fixed composition, dataset transfer and cross-layer consistency

Fixed-young-composition reconstruction preserved the score (counts rho 0.954, CPM 0.945) and age association (rho ~0.956; Supplementary Fig. 3). GSE302188 replicated the age ordering (rho 0.895; batch-partial 0.794; within-batch permutation P=2e-4), and GSE262290 replicated cross-run effects (age-effect rho 0.863, permutation P=0.001). Human projection gave GTEx rho 0.071 (P=0.29), HLiCA unadjusted rho 0.445 (P=0.0015; study-adjusted 0.217, P=0.14), Guilliams rho 0.77 (P=0.072) and pooled rho 0.32 (I^2=76.5%) (Supplementary Fig. 13, 14, 25).

Table 1 | Three levels of external validation.

Level	Question	Cohort(s)	Result	What it does / does not establish
Level 1	Directional concordance of the signature	GSE302188 (83 livers); brain atlas (15 regions)	154/195 genes (79.0%; permutation P=0.002); 13/15 brain regions	Supports 'not a batch artefact'; does not establish calibration
Level 2	Effect-vector reproducibility	GSE262290 (9- and 30-month samples in two runs)	rho 0.863 (permutation P=0.001); 155/196 genes (79.1%) same direction	Supports repeatability; male, bulk, only 2/5 ages cross-run
Level 3	Absolute age calibration	All external cohorts (GSE327303, TMS, bulk)	Cell-level MAE at or above the mean-age baseline in all eight cohort x	Not supported; rank transfer is not calibrated age transfer

			mode evaluations; donor-level 6-donor forward transfer (R2 0.875) is separate and not comparable	

Literature context for selected features

To separate direct aging evidence from developmental or metabolic annotation, I curated PubMed-indexed reports for the top clock features and the brain-consensus genes (Supplementary Fig. 5). Most top features are not established liver-aging genes: Plag1 is a neuronal differentiation transcription factor, Ppm1h an ATF6-regulated phosphatase in liver cancer, Wls a Wnt-secretion factor, and Mup1/Hsf2bp hepatic metabolic or stress regulators. Direct aging reports exist for Lncbate1 (adipose lipid synthesis during aging), Ctss (age-dependent blood-CSF barrier disruption and neuroinflammation), C1qc (age-dependent microglial phenotype) and Gpr17 (aged hippocampus and oligodendrogenesis). Mup11 and Pcdhb9 have no aging-specific report. This is consistent with a data-driven clock: its selected features are mostly developmental or metabolic, while a subset of its genes and the brain-consensus module carry literature-supported aging roles.

Cell-type-resolved and zone-resolved age effects

To distinguish composition from cell-intrinsic state, I rebuilt donor-level pseudobulk for eight major cell types (40 donors; cholangiocyte 23) and for hepatocyte PP, PC and all compartments. Using limma-voom with age and sex, every cell type showed widespread age effects, with sex-by-age interactions concentrated in hepatocytes, myeloid and mesenchymal cells (Supplementary Fig. 8). Hepatocyte PP and PC each showed about 1,300 age-associated genes; 254 changed differently between paired PP and PC, and paired PC-PP module differences identified M09, M02, M14 and M11 (all negative). Removing immune marker genes left hepatocyte age t-statistics essentially unchanged (Spearman 0.9999999979; median |delta t| 5.4 x 10^-5).

RNA-ATAC module selection

To select modules for RNA-ATAC follow-up, I required batch-half sign stability, age association, an independent GSE302188 age direction matching the internal beta, at least 100 linked ATAC peaks, and RNA-ATAC coupling with the same age direction. Two modules passed: M08 (71 genes; GSE302188 rho +0.89; 405 peaks; coupling rho 0.43, P=0.005) and M14 (274 genes; rho -0.60; 1,169 peaks; coupling 0.56, P=1.9 x 10^-4; Supplementary Fig. 9). Adding ATAC to RNA gave a delta MAE of +0.14 weeks (95% CI -2.07 to 2.14).

Triple-signature drug reversal

Three drug signatures (ElasticNet, hepatocyte age DE, externally replicated) were weakly correlated (strict-Z Spearman 0.78/0.41/0.47), and no drug-module pair survived correction (0/315; 7 nominal P<0.05; Supplementary Fig. 10, 11).

Exploratory synthesis: SEM, module stability, pseudotime and RNA–ATAC coupling

An exploratory SEM gave composition-only R^2 0.56, state-only 0.91 and combined 0.83. WGCNA M08/M12 were stable across batches; M15/M18/M07 were not. RNA–ATAC module coupling was

module-specific (M01 rho 0.44 opposite direction; M08 0.43 same direction; Supplementary Fig. 29).

Peak-to-gene, TF activity and multi-omics factors

Among 1,642,253 motif–peak–gene edges, accessibility–expression direction concordance was 50.1% overall (hepatocyte 50.7%, endothelial 42.5%); M08 65.0%, M14 48.0%. TF activity ranked Hnf4a, Hnf1a, Ppara, Tead1 and Mef2a highest. MOFA2 identified an age-associated RNA–ATAC factor (Factor4 rho 0.57) distinct from SASP (Supplementary Fig. 21, 22).

Integrated evidence synthesis

Fig. 6 summarizes claim-level direct evidence and next tests: 6a, claim × evidence matrix; 6b, statistical units; 6c, evidence strength by layer; 6d, observed constraints; 6e, programme evidence; 6f, decision boundary; 6g, cross-organ evidence; 6h, evidence ceilings; 6i, inference limits. The matrix separates donor structure, internal rank clock, sampling-sensitive BH gene, protein clock, network proximity, batch/disease independence, cross-species portability and absolute calibration.

Cell-type-resolved internal clocks varied (hepatocyte rho 0.949, MAE 9.19 weeks; cholangiocyte 0.400, 28.33, n=23; other types 0.730-0.949). A frozen hepatocyte clock transferred to an independent Smart-seq3 cohort when matched to the cell population: periportal AUC 0.892 (rho 0.67), pericentral 0.795 (rho 0.50), pooled 0.744. Tabula Muris Senis reproduced rank-level transfer after target-domain standardisation (AUC 0.758 for 10x and 0.643 for Smart-seq2). The pre-specified disease gate (HFD versus chow; failure if AUC > 0.65) gave AUC 0.484 at the cell level. Cross-batch holdout gave AUC 1.000 and 0.852.

The clock's selected genes form a data-driven axis, and the transcriptome-wide age ranking is enriched for canonical ageing programmes (see the fgsea analysis below). Model-implied virtual knockout ranked Plag1 (-1.11 weeks), LncBate1 (-0.61), Olfr1030 (-0.54), Wls (-0.54) and Ppm1h (-0.51) as the strongest score modifiers, and 49 of the top 50 features were stably selected at frequency >=0.8. Among 28 literature-validated ageing genes, only Hsf2bp materially changed the score. Biology-anchored panel scores were interpretable but weaker externally (AUC 0.5-0.7), with the inflammaging panel best (Supplementary Fig. 1g–i).

Multiplicity was re-run within every reported family with both BH and BY [28–29], and permutation P values were right-censored at 1/(n_perm+1), never zero. Dependence-robust correction changed several counts: differential expression 26,283 (BH) to 5,037 (BY; effect-filtered archived table); proteome 2,804 to 1,686; lipidome 20 to 10; motif-dimension 963 to 474; subtype composition 16/35 to 10/35; cell-type-by-module 3/17 to 2/17 (endothelial ECM is BH-only); immune bulk 15/16 to 12/16; immune within 6/11 to 5/11. The nine-type composition (6/9), immune-subset (12/12) and HALO latent-age associations (34/40) are unchanged.

Donor-level pipeline and depth decomposition

Unified donor-level 5-fold × 5-repeat CV gave ElasticNet MAE 10.4 weeks (rho 0.94); baseline 34.3 (rho -0.28), depth+composition 35.3, expression+composition 12.4 (rho 0.92) (Supplementary Fig. 2a,b). Within-animal UMI thinning produced no systematic score shift (mean within-donor Spearman between score and retained fraction 0.09, median 0.00; Fig. 3g), whereas between-animal depth was associated with score (depth-age rho -0.43; depth-score -0.38; Fig. 3h). Depth is observational, and the display band is a descriptive guide.

Donor-level zone, composition and programme audits

Donor-fixed three-zone models are rank-deficient because age is constant within donor; paired PC-PP module differences were negative for M09, M02, M14 and M11. scCODA gave credible age effects for all non-reference types with model-dependent signs; CLR sensitivity was retained (Supplementary Fig. 8, 9 and 27).

A late myeloid M06–SASP programme and its functional robustness

Age-associated expression was widespread across cell classes (Fig. 2a), and module selection retained M08 and M14 (Fig. 2c). A SASP score from 95 measured SASP genes increased with age in discovery (rho=0.40, P=0.0097), GSE302188 (83 livers; rho=0.788, batch-partial 0.794, within-batch permutation P=2e-4) and GSE262290 (52 livers; rho=0.841, run-partial 0.879, P=2e-4). A SenMayo score reproduced the signal (partial rho 0.782 and 0.880). M06–SASP correlation was 0.957 and 0.958 vs clock–SASP 0.868 and 0.793 (Williams P=2.6e-6 and 1.1e-6); removing the 12 shared genes left the correlation essentially unchanged (Pearson 0.956/0.957; Spearman 0.913/0.912; age-adjusted partial 0.749/0.766). M06 explained SASP better than the clock after age and batch adjustment (partial r=0.918 vs 0.722 and 0.933 vs 0.628; source table); Pearson correlations are in Fig. 2d and SASP-age panels in Fig. 2b.

SASP transcript share was highest in endothelial (64.5 per 10k UMIs) and mesenchymal cells (59.1), followed by Kupffer (42.7) and hepatocytes (41.1) (Supplementary Fig. 31a); endothelial and mesenchymal cells were the top two classes under six score definitions (bootstrap top-2 probability 1.000; split-half ranking rho 0.998). Mesenchymal SASP rose with age (mean-log rho 0.561, 95% CI 0.333–0.740; rank 0.548; pseudobulk 0.443); endothelial SASP declined (rho -0.407; negative in four of five metrics). Hepatocyte mean-log increase was rho 0.463 (pseudobulk -0.014, rank 0.086, UMI-share 0.072) and correlated with detection fraction (rho 0.643; Fig. 2e).

M06 was predominantly myeloid [30]. In the 295,364-nucleus atlas, M06 transcript share was 9.45% in Kupffer, 9.37% in non-resident myeloid, 3.75% in endothelial and 0.13% in hepatocytes; the donor-paired myeloid-to-hepatocyte M06 share ratio was 84-fold (95% CI 72-98). NNLS deconvolution of the bulk cohorts attributed 43% of M06 transcripts to myeloid, 42% to lymphoid (likely an upper bound), 11% to endothelial and 1.8% to hepatocytes. In GSE328448 spatial sections, M06 score correlated with an independent, non-overlapping myeloid marker score (Spearman rho 0.17-0.20, permutation P<=0.001; bivariate Moran's I 0.03-0.09), and M06-high bins overlapped myeloid-high bins more strongly in aged than young sections (OR 2.35-2.61 vs 1.05-1.23; Fisher P<0.001 vs 0.39-0.89; ED12a,b). In independent TMS liver scRNA-seq, the donor-level myeloid-to-hepatocyte M06 share ratio was 7.9x (10x; 95% CI 5.2-11.1) and 10.3x (Smart-seq2; 5.8-17.8), lower than in the discovery atlas but consistently >1 (ED12c). Adjusting for all estimated cell fractions reduced the M06-SASP partial correlation from 0.766 to 0.541 (GSE302188) and from 0.671 to 0.553 (GSE262290), but did not abolish it (P<1e-3), indicating that composition contributes to, but does not fully explain, the M06-SASP coupling (Fig. 2f).

Functionally, SASP was dominated by inflammatory and chemokine signalling with a secondary ECM arm. Under an explicit expressed-gene background and library-wide FDR, GO inflammatory response (32/207; OR=37.1; q=8.3e-31), KEGG cytokine–cytokine receptor interaction (45/242; OR=29.1; q=8.1e-38), KEGG TNF (24/110; OR=25.2; q=1.1e-20) and Hallmark inflammatory response (29/195; OR=10.7; q=1.2e-15) were enriched; ECM organization was significant but secondary (12/169; OR=11.7; q=2.6e-7) and fell to q=0.092 under the WGCNA background (Supplementary Fig. 31b). Expression-matched permutation (10,000 draws) confirmed the inflammatory and ECM signals (observed 32 vs null 0.75 for inflammatory; 12 vs 0.64 for ECM),

split-half analyses retained enrichment in the SASP-positive half, and GSEA on the SASP-correlation ranking reproduced the inflammatory/cytokine programme (Supplementary Fig. 31b).

Orthogonal layers supported this model, with layer-specific differences. In the 16-channel proteome (PXD040722), 11 SASP proteins were measurable; all 11 changed in the same direction as RNA, 8/11 increased with age (OR=15.8; q=5.8e-5), and the curated protein score correlated with age at rho=0.861. Lipidomics showed TAG/PC/SM depletion and CL/DAG accumulation; PC+CL species were enriched (OR=5.09; P=0.0012), DGAT1/2 were down, and LPCAT2/PLA2G4A rose with age and SASP, consistent with Lands-cycle remodelling. Spatial communication (GSE328448) was axis-selective: Angpt1-Tek, Igf1-Igf1r, Vegfa-Flt1 and Tgfb1-Tgfbr1 increased, Jag1-Notch1 decreased, and CCL5-CCR5 was the only axis still rising at 121 weeks (ED5). In this study, promoter methylation (GSE225166) was not associated with SASP (0/70; delta vs RNA rho=-0.19), and SASP-linked chromatin accessibility was not more age-changing than matched peaks (P=0.19), whereas a clock/chromatin MOFA factor (Factor4) was age-associated (rho=0.57) and SASP-independent (Supplementary Fig. 22c).

Hepatocyte SASP increase was detection- and depth-dependent in this score and cohort; GSE327303 (six donors, age confounded with donor) gave exact P=0.133 (Fig. 2e).

Pharmacological interrogation and translation readiness

Fifteen compounds mapped to 175 drug-target pairs (148 genes) [31], and six of nine profiled targets were measurable in GTEx liver (n=214) [32]. LINCS (5,425 compounds) [33] showed a family-level reversal signal (max strict Z 4.30, FWER P=0.034) but no compound-level reversal or known-geroprotector enrichment survived correction (ED6, Supplementary Fig. 10, 11, 28).

Target reach, ortholog retention and intervention response

Target reach was cell-type-selective: most targets were measured in bulk liver; GLP1R was detectable in endothelial/T cells but not hepatocytes (0/46 >1 logCPM). Ortholog retention was 206/310 (66.5%) versus 68.1% background (P=0.56). In GSE280382 [34], the clock separated aged vs young (+1.87 SD; P=2.9e-9) and exenatide changed the score by +0.24 SD (P=0.215; MDE 0.50 SD).

Formal decision methods and design stress

Across 10 target classes, no class cleared all six gates (0/10; ED11b-h); module overlap (0/8) and clinical endpoint (0/10) were binding. Only the all-pass pattern cleared P>0.05 under the neutral encoding (0.262), and any single gate failure dropped the score to 0.016 (ED11c,d).

Sampling stress, platform transfer and intervention-design limits are shown in Fig. 7.

A pre-registered robustness protocol fixed the design matrix, VIF, MDE and Go/No-Go thresholds for anti-IL-11, PINK1 and OSK; these are prospective registrations for future experiments. Detailed audits of age–batch identifiability, depth, composition, disease, external calibration and stress tests are provided in Supplementary Notes 1–6 and ED1–ED12.

Discussion

I identify three separable axes in mouse liver ageing: a transcriptomic clock that ranks animals by age, a 310-gene signature that overlaps the M08/M14 modules, and a late SASP programme

tracked by the myeloid inflammatory module M06. The clock ranks age well; the M06–SASP axis runs largely independently of the clock; and the two axes correlate mainly because both change with age. The clock signature also projects into most brain regions, although transfer between brain regions is partial. I therefore treat the clock as a ranking instrument and the M06–SASP programme as a separate myeloid-centred inflammatory axis.

The clock is robust for age ordering. In discovery, leave-one-donor-out MAE was 9.19 weeks (rho 0.949), and the score–age association replicated in GSE302188 and GSE262290 (rho 0.895 and 0.928; five-cohort meta r=0.911, I2=0). The 310-gene signature mapped to 210 brain genes and tracked age in 13/15 regions (median rho 0.49); Ctss, C4b, Tyrobp and C1q rose and Gpr17 fell in all 15. Of these, 85 were also brain clock genes. Brain-region clocks transferred partially (median off-diagonal R2 0.43; 59/210 pairs <0), and the clock genes did not reproduce an IFN/apoptosis signature.

M06–SASP coupling is the most robust module-level association in the dataset and does not depend on shared genes. M06 contains 12 SASP genes (OR=5.91; q=2.0e-4); its eigengene correlates with SASP at rho=0.833 in discovery, and M06–SASP correlation is 0.957–0.958 externally. Removing the 12 shared genes left the correlation essentially unchanged (Pearson 0.956/0.957; Spearman 0.913/0.912; age-adjusted partial 0.749/0.766), so the coupling reflects the module as a whole, beyond the 12 shared genes. Deconvolution and atlas composition place its origin mainly in myeloid cells (43% of bulk M06 attribution; 84-fold higher donor-paired M06 share than hepatocytes, 95% CI 72-98; independent TMS liver scRNA-seq gives 8-10x). M06 is therefore a myeloid-centred inflammatory module. Adjusting for all cell fractions reduced but did not remove the correlation (0.54–0.55; P<1e-3).

Endothelial and mesenchymal cells had the highest SASP transcript share, stable across six scoring schemes and resampling. Mesenchymal SASP rose with age; endothelial SASP fell; the hepatocyte mean-log increase was sensitive to scoring. The data therefore support a mesenchymal increase, an endothelial decrease and a myeloid M06 association—an important distinction, because a hepatocyte-centred narrative would misassign the cellular origin.

The SASP programme is reproducible and differs across molecular layers. Cytokine/chemokine signalling and a secondary ECM arm survived two backgrounds, 10,000 expression-matched permutations, split-half analysis and GSEA. SenMayo reproduced the signal (Fig. 2g) with 61/95 shared genes. Other layers reinforce this signal: 11/11 measurable SASP proteins changed in the same direction as RNA and 8/11 rose with age; lipidomics showed TAG/PC/SM depletion and CL/DAG accumulation with Lands-cycle remodelling; spatial communication was axis-selective. In this study, promoter methylation and broad chromatin accessibility were not associated with SASP.

Limitations and translation

This study has several limitations. Age and batch are deterministically nested in the training cohort (Batch 1: 13, 81, 121.5 weeks; Batch 2: 53, 105 weeks). I audited this explicitly: the full design has rank 6 of 9 with three exact null vectors, batch adds zero rank to age, and the age–batch decomposition is likelihood-flat (delta RSS=0, delta logLik=0, R2=0.933). Batch-specific age slopes differed (0.885 vs 0.663 weeks per week; interaction P=0.034), and continuous, spline and batch-slope models are full rank only under functional-form assumptions. Batch-independent age effects are therefore not identifiable; leave-one-batch-out and leave-one-design-out analyses are stress tests, not independent validation. Where external cohorts cross batch or run, I report

batch-partial and within-batch/within-run permutation estimates (GSE302188 batch-partial 0.794, within-batch P=2e-4; GSE262290 run-partial 0.879). The clock ranks age but does not calibrate absolute age externally (MAE 42–63 weeks), and region-specific brain clocks transfer only partially (median off-diagonal R^2 0.43; 59/210 pairs <0). Between-animal depth is associated with the score, and depth-matched models increase MAE. Cell-type SASP scores are definition-sensitive; the hepatocyte SASP increase is detection- and depth-dependent, and GSE327303 (six donors, age confounded with donor) cannot adjudicate direction. M06–SASP coupling is robust but associational; macrophages can clear senescent cells or adopt a p21+TREM2+ state [35,40], and the M06 age trajectory is cohort-dependent. Promoter methylation covers a subset of SASP genes, ATAC links are nearest-TSS only, and proteome, lipidome, methylation and spatial cohorts are not the same animals. dN/dS could not be retrieved and does not affect the main conclusions; DoWhy/EconML [37–38] cannot identify age net of batch because the design is rank-deficient. The six-gate score is a decision aid under declared encodings, not a probability of validation, and stress tests quantify what n=40 can support. Low-coverage external samples lose separation (AUC 0.38–0.46), disease groups differ in HFD duration and size, and cross-batch holdout AUC is inflated by age nesting. Mup11 is not in the 310-gene signature and its discovery signal is preprocessing/sex-dependent. An MAE-based random-set null gave p=0.77, so the canonical panel has no demonstrated unique advantage, and macaque clock transfer was not established. Each of these boundaries was audited directly: design rank/nullity, likelihood-flat age–batch decomposition, within-batch permutation, leave-one-design-out, depth thinning, fixed-composition reconstruction, disease gate, external calibration and random-set nulls are reported in ED1–ED12 and Supplementary Notes 1–6. Fibrosis stage was not available in GSE328448, so independence from fibrosis remains untested; spatial zonation is also disrupted in acute-on-chronic liver failure [39]; clock transfer across organs was partial.

Pharmacology did not produce a validated liver-ageing candidate: 0/315 drug–module pairs and 0/5,425 LINCS compounds survived correction, no class passed all six gates, and known geroprotectors were not enriched. The six-gate score is a decision aid, not a validation probability; the 192-scenario analysis shows the zero result is structural. The pharmacological analysis is therefore hypothesis-generating only.

The central conclusion is spatial: in mouse liver, the myeloid inflammatory programme M06 is concentrated around the portal vein, whereas the hepatocyte clock is concentrated around the central vein. The M06 pattern is robust across four donors (mean rho −0.20, P=0.010) and remains after adjusting for myeloid abundance and spot cellularity; the clock pattern is weaker and sensitive to spot cellularity. The clock orders donors by age but does not measure absolute age; cross-cohort correlations (rho 0.895 and 0.928; meta r=0.911) support this relative ordering, not an absolute age calibration. The results define a spatial axis and a reachability map.

Recent work extends this: p21+TREM2+ macrophages were linked to MASLD inflammaging [40], CDK6 inhibition suppressed SASP and age-related decline [36], a quasi-spatial liver atlas defined an early ageing niche [41], hepatic SIRT6 counteracted chromatin ageing [42], senescent hepatocytes were targeted [43], and senolytics entered MASH testing [44]. These reinforce the separation but leave causality and translation unresolved.

Conclusion

I analysed the RNA/ATAC atlas at the donor level, together with independent bulk cohorts, a 15-region brain atlas and proteomic, lipidomic, methylation and spatial data. The main result is

spatial: M06 is concentrated around the portal vein and the hepatocyte clock around the central vein, and the M06 pattern survives myeloid-abundance and cell-density adjustment. Mouse liver ageing therefore separates into spatially distinct axes. The hepatocyte clock orders the sampled donors by age (MAE 9.19 weeks, rho 0.949) and replicates externally in age ordering (rho 0.895 and 0.928; meta r=0.911), but it does not calibrate absolute age. Its 310-gene signature overlaps the M08/M14 modules, projects into 13/15 brain regions, and sits alongside a SASP programme tracked by the myeloid module M06 (r=0.96), with cytokine/chemokine and ECM enrichment supported by proteomic, lipidomic and spatial data. Pharmacology reached liver-detectable targets and a family-level LINCS reversal signal (FWER P=0.034) but no compound-level validation. The main limits are age–batch nesting, failed absolute calibration, depth/coverage sensitivity, scoring-dependent cell-type SASP estimates, an associational M06–SASP link, non-matched cross-layer cohorts and a design that cannot separate age from batch. Prospective single-cell and spatial cohorts, donor-matched multi-omics, target-engagement experiments and independent age calibration are still needed.

Methods

Data source and ethics: public mouse liver same-nucleus multiome resource GSE328206 (training) and external mouse datasets GSE327303, E-MTAB-12579, TMS 10x and TMS ss2, plus GSE302188 (batch–age crossed), GSE225576 (bulk liver) and GSE262290 (cross-run); no new animals were used. Animal cohort: 40 C57BL/6JN mice, five ages, eight per age. RNA and ATAC profiles were processed into donor-by-gene and donor-by-peak pseudobulk matrices; RNA and ATAC nuclei counts are reported after the stated QC and are not interchangeable across filtering versions. Clocks used variance-filtered features and outer leave-one-donor-out validation with inner tuning; the fast benchmark used a different feature budget. External transfer used gene-ID mapping and frozen or target-domain standardisation; no target labels were used for tuning in frozen mode. Batch identifiability used full-dummy rank, nullity and condition number, with non-redundant alias checks; within-batch and batch-specific slopes were fitted separately. Composition was analysed at the donor level with descriptive conditional regressions and variance partitioning, not causal mediation. Gene-level and gene-peak tests are separate families (defined below). Protein TMT channels are nested with age; ATAC and cross-species analyses are reported with their confounds. Spatial donors were non-overlapping with the bulk and scRNA cohorts (n=4 mice, four Stereo-seq sections), collected in an independent study and processed on a different platform (Stereo-seq bin200); no spatial section was used in clock training. All code and source tables are archived (see Code availability); analyses were run on processed matrices derived from the public raw data.

Gene-set definitions and mapping chain. The primary clock used the top 3,000 variance genes as ElasticNet input. Of these, 310 had non-zero coefficients (180 positive, 130 negative; Fig. 3f) and form the clock signature. The 300-gene gene-peak family is a separate set defined by the 300 smallest gene-peak permutation P values; it is distinct from the 310 clock genes. For the 300-gene family, 3 replicates x 1,000 permutations gave 3,000 nulls per gene (effective 3,001); the 10-gene escalation used 3 x 10,000 permutations, giving 30,000 nulls per gene (effective 30,001). The P value is (1 + #{null >= observed})/(1 + n_null). Of the 310 signature genes, 216 have a human symbol, 213 mapped to an Ensembl human gene ID, 206 had an MGI 1:1 human–mouse pair, 124 fell in the LINCS universe, and 122 (69 up, 53 down) passed the final orientation/membership filter. Per-gene mapping and loss tables are in the source data.

Pharmacological integration and null calibration

Data sources. The liver-ageing signature was the non-zero P0 hepatocyte-clock predictor (ElasticNet; 310 genes, 180 up, 130 down), with WGCNA modules and batch-half sign stability. The drug–target map had 15 compounds and 175 pairs (148 human genes); compound signatures were LINCS L1000 consensus Up/Down sets (5,425 compounds; 9,525-gene universe). GTEx liver reach used donor-level mean log2 TPM and linear age β (n=214). Clinical candidates came from a 24-row table using only tier, design and endpoint columns [45]. GSE280382 AgedLT liver formed the intervention challenge set.

Orthologue mapping and null calibration. Mouse genes were mapped to human symbols via MGI HOM_MouseHumanSequence [46]; all sets were compared in human space. Drug–module overlap used an upper-tail hypergeometric test (M=3,853 human-mapped network symbols from 6,016 mouse genes) with BH across 315 pairs. Clock overlap used 10,000 size-matched draws from the same background, separately for up and down sets. Hub enrichment used the degree-matched null for the GTEx 426-gene signature.

LINCS reversal. Query was 69 clock-up and 53 clock-down symbols; strict $Z = \min(zA,zB) - \max(zC,zD)$, with 1,000 query-set permutations (seed 20261112), BH q and a family-maximum FWER null. Geroprotector enrichment was the AUC of strict Z for 15 labelled compounds.

GTEx and intervention scoring. Liver expression was mean log2 TPM and liver age association the linear β with its P; strict $Z \geq 1.96$ was an uncorrected screen and permutation q was reported separately. In GSE280382, only AgedLT liver samples were used (young n=8, aged n=9, aged+exenatide n=8; all batch 3). Counts were log1p(CPM), gene-wise z-scored, and scored with the frozen clock linear predictor standardised by training mean and scale. Module scores were the mean z of measured genes. Contrasts used Welch t-tests with Welch–Satterthwaite 95% CI and BH within contrast; cells were not replicates.

Constraint analyses

Human liver projection. GTEx liver bulk TPM (n=226 donors; age, sex, RIN, ischaemic time and centre as covariates) and HLiCA hepatocyte donor pseudobulk (48 health-tier-filtered donors) were projected with the 216 human symbols of the frozen signature. Expression was log2(TPM+1) for GTEx and log2(CPM+1) for HLiCA, gene-wise z-scored; the score was mean z of up genes minus mean z of down genes. GTEx models adjusted for age, sex, RIN, ischaemic time and centre; HLiCA for age, sex and study. Spearman correlations and 1,000 expression-matched permutations were reported; the analysis is rank-based.

Human failure modes. GTEx strata were sex, centre, RIN quartile and ischaemic-time quartile; HLiCA strata were study, sex and hepatocyte cell-number quartile (≥5 donors and ≥3 ages). Gene-level direction was conserved when the human age β matched the mouse clock coefficient in both datasets, partial in one, divergent in neither; module enrichment used Fisher exact tests.

Ortholog retention. Human–mouse orthologs came from MGI HOM_MouseHumanSequence (18,784 1:1 pairs). Sets were the 310-gene signature, the 2,690 zero-coefficient clock background, a housekeeping proxy and RPS/RPL symbols. Fractions carry Wilson 95% CIs; Fisher tests were BH-adjusted across 12 comparisons. Macaque 1:1 orthologs and protein identity came from Ensembl Compara. dN/dS was not computed (Compara returned null; transcript lookup too slow).

Reach map and detectability. Units were donor × cell type, never cells (345 primary units; hepatocyte restricted to subtype all). Human targets were mapped to the most highly expressed mouse ortholog. Hepatocyte expression required mean >1 logCPM and detection >50% of units; enrichment required ≥2× the highest non-hepatocyte mean. Detectability used the frozen clock score in SD units of the 25-sample distribution; MDE was the exact noncentral-t two-sample value (n1=8, ratio 9/8, α=0.05, power 0.8). The null used 20,000 label permutations × 21 modules (420,000 contrasts; seed 20261112). GLP1R was summarised under whole-hepatocyte (46 units) and zone-resolved (138 units) policies; zone units per donor were never treated as independent.

Methods: SASP, functional enrichment and multi-omic validation

SASP gene set and scoring. The primary SASP set contained 96 curated genes (95 measured in hepatocyte pseudobulk), combining canonical senescence-associated secretory genes with the SenMayo core. The published SenMayo set (118 unique mouse genes) was used as an external redefinition. Scores were the mean z-score of detected genes within each cohort; cell-type scores were computed per cell and aggregated to donor x cell-type units. Age associations used donor-level Spearman correlation with BH correction; external bulk cohorts used batch- or run-partial Spearman with 10,000 age-within-batch permutations. GSE302188 (83 liver samples, five ages, three fully crossed batches), GSE262290 (52 samples, five ages, two runs), GSE327303 (six donors, 13 vs 78 weeks) and the independent cohorts GSE209823, GSE221122 and GSE181797 were analysed with the same scoring pipeline. M06–SASP shared-gene sensitivity removed the 12 genes present in both sets and recomputed the module and SASP scores in GSE302188 and GSE262290; Pearson, Spearman and age-adjusted partial correlations were compared with the full module.

M06 and cell-type deconvolution. WGCNA modules were defined previously; M06 contains 403 genes. Module eigengenes were the first PC of z-scored module genes (mean z as fallback). M06–SASP correlations used donor-level Spearman with Williams tests for dependent correlations. Cell-type fractions in bulk liver were estimated by NNLS on log-CPM profiles using an eight-cell-type reference from the 295,364-nucleus snRNA atlas; marker-score correlations and atlas M06 density were used as orthogonal checks. Composition-adjusted partial correlations controlled age, batch and all estimated fractions.

Functional enrichment and multi-omic layers. Enrichr REST was queried for GO Biological Process 2023, MSigDB Hallmark 2020, KEGG 2021 Human and Reactome 2022. Hypergeometric tests used two backgrounds (all 30,279 expressed genes and the 6,016 WGCNA-mapped genes); 10,000 expression-decile-matched permutations calibrated enrichment; split-half analyses compared genes in the top and bottom 50% of SASP correlation; GSEA used weighted Kolmogorov–Smirnov with 1,000 permutations. Proteome, lipidome, methylation, spatial (COMMOT/scDiffCom) and ATAC analyses are described in the source reports; all cross-layer comparisons are gene- or module-level because the cohorts are not sample-matched.

Methods: formal decision and identifiability analyses

Six-gate encoding. Gates g1–g6 were expression, liver age association, module overlap, LINCS reversal, clinical endpoint and safety; states were pass, partial, fail or unknown. Encodings were optimistic (1.00, 0.50, 0), neutral (0.80, 0.40, 0.05) and conservative (0.50, 0.25, 0.02); unknown took p0=0.28 (12/43). The joint score was a declared-probability noisy-AND $P=\Pi p_g$ (conditional independence given class); no likelihood or posterior was computed. Veto rules were none, any-fail, k=2, k=3 and a weighted product; sensitivity crossed encodings × rules and p0 ∈ {0.15, 0.45}.

The counterfactual set gates 1–4 to pass or best observed state; ceiling=p5×p6. Reach was p_reach=1/(1+e^{−(log2TPM−1)/0.8}), with ≥0.80 reachable.

Binary gate tree and stress. All 64 pass/fail patterns were enumerated under the three encodings; the all-pass and one-fail contrasts quantify gate necessity; no resampling. Stress simulations used the measured 40-donor pseudobulk and frozen clock (top-3,000 variance genes, ElasticNet α=0.01, l1_ratio=0.5). Refit-holdout fitted n=4–30 donors (100 draws); the design grid crossed young-heavy/balanced/old-heavy compositions with n=4–30 (60 draws/cell); age imbalance used 200 draws. The positive control implanted β×SD×z(age) into 200 genes against 800 null genes. Nonlinear batch added a stationary RBF Gaussian-process field over age to 1,000 null genes under balanced or confounded splits. Platform noise was cohort donor residual SD divided by internal LODO residual SD.

Identifiability. X was intercept, five age indicators, two batch indicators and sex (n=40). Rank was computed by SVD; null vectors were age indicators summing to the intercept and batch_01 = ages 13+81+121.5, batch_02 = ages 53+105. Supports are disjoint, so a batch-adjusted age contrast is not estimable non-parametrically (rank 6/9, nullity 3). DoWhy/EconML cannot identify age net of batch without additional assumptions.

Spatial zonation and statistics. GSE328448 Stereo-seq bin200 sections were scored for the continuous zonation axis (Layer1, central vein; Layer9, portal vein) using published liver-zonation markers [6–8,10]. M06, myeloid-marker, hepatocyte and endothelial scores were mean log-normalized expression over measured genes. Within each section, I computed Spearman rho with the zonation score, 6-nearest-neighbour Moran's I and bivariate spatial lags; null distributions used 1,000 coordinate/label permutations and 500 value permutations. Donor-level tests used one-sample t-tests across four sections (n=4), not spot counts; M06 was residualized on myeloid score, nCount, nFeature, hepatocyte and endothelial scores where stated. Disease-zonation context and spatial-method scope are discussed in refs [39,47].

Drug-module completeness and power. All 15×21=315 pairs used the upper-tail hypergeometric null with BH. LINCS signature dependence used Kendall tau and Jaccard overlap of top 20/50/100/500 strict-Z sets. Synthetic effects 0.24–2.0 SD were added to aged-control scores (n=9; SD 0.343); 20,000 Monte Carlo Welch tests per design and noncentral-t power were computed. This is a design calculation on the score scale.

Peak-to-gene, TF, MOFA, cell-level. The precomputed motif–peak–gene table (1,642,253 edges) was summarized by cell type, contrast and module; concordance was the fraction of same-sign dAccess/dExpr edges. TF activity was the maximum absolute age effect (descriptive). MOFA2 used RNA/ATAC logCPM, top 2,000 variable features per view and eight factors. Cell-level donor-block variance used 179,655 hepatocytes; a MixedLM was attempted but the donor random-effect variance hit the boundary, so the donor-block partition is reported.

Additional cohorts and zone models. Guilliams human liver h5ad was aggregated to donor pseudobulk and scored with the 216-symbol signature; random-effects meta used Fisher-z and DerSimonian–Laird. Open Targets/ChEMBL tractability was queried for 12 targets. scCODA [48] used donor×cell-type counts (hepatocyte reference; continuous age; NUTS 10,000/5,000); fixed-composition reconstruction used observed or fixed young (13-week) weights; real fgsea [49] used fgseaMultilevel with 1,000 permutations. External GSE302188/GSE262290 and brain GSE212336 scoring followed the same frozen-signature rules; cross-region brain transfer applied

each region's fitted SelectKBest–StandardScaler–RidgeCV pipeline and masked the in-sample diagonal. ATAC peaks were processed with Signac [50].

Cross-dataset pathway direction. Full-transcriptome age rankings were computed as Spearman rho (GSE302188, n=83) or age effect (GSE262290, n=52) per gene, and fgseaMultilevel was run with the same mouse Hallmark sets (minSize 15, maxSize 500, eps=0, 1,000 permutations). For the 18 discovery-significant pathways, NES signs and Spearman NES were compared across cohorts. Clock-gene direction was the sign of the frozen clock coefficient versus external age rho; M14 genes used the discovery full-ranking rho. Binomial tests assessed concordance, and within-batch and within-run label permutations (1,000 draws, gene covariance preserved) gave P=0.002 (GSE302188) and P=0.008 (GSE262290); Mup11 was evaluated separately because it is not in the 310-gene signature.

Methods: donor hierarchy, trajectories and stability

Donor-level variance partition, trajectory comparison and stability selection. Cell-type pseudobulk units were scored with the frozen clock; donor variance share was estimated from a donor-block OLS model with age, sex and cell type. No random-effects model was fitted. Trajectories were compared with linear, quadratic, B-spline (df=3), plateau, segmented and sex-interaction models using AIC/BIC and leave-one-donor-out RMSE; five ages limit spline and segmented inference. Stability selection resampled donors or age strata 200 times, refit ElasticNet on the frozen 3,000-gene budget, and recorded selection frequency and sign stability for the 310 signature genes. Module concordance used the signature module assignments and human gene-level age effects.

Methods: donor-level zone, composition and programme audits

Software and reproducibility: analyses used Python 3.12 (numpy 2.1, pandas 3.0, scikit-learn 1.9, statsmodels 0.15, semopy, matplotlib 3.8), scCODA 0.1.9 with TensorFlow 2.19, and R 4.6.1 with fgsea. Random seeds were 20261112 (LINCS/permutations), 20261113 (fgsea/GSE262290) and 0 (brain CV). Processed tables and code are archived at Zenodo (10.5281/zenodo.24381654 and 10.5281/zenodo.24381798).

Figure legends

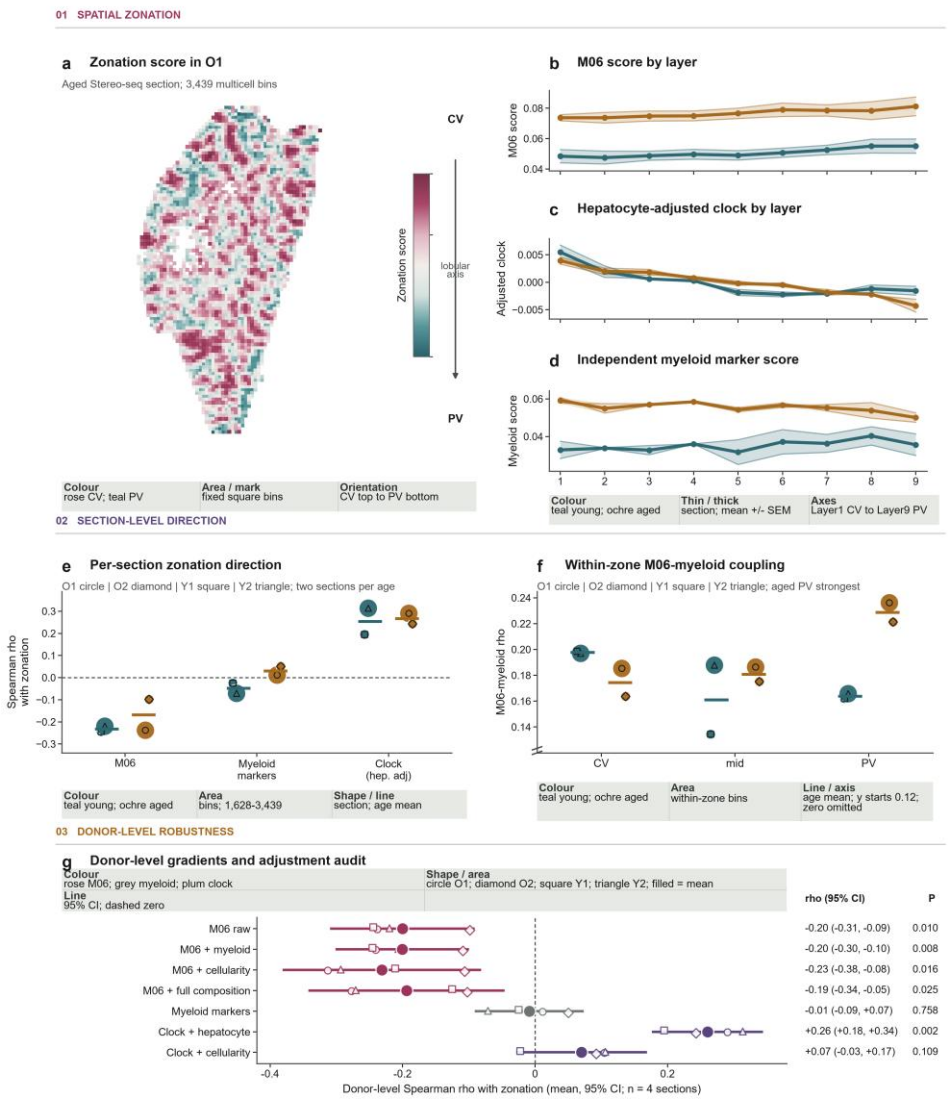

609

610 Fig. 1 | Zonation separates M06 from clock. a, Zonation score, GSE328448 Stereo-seq section,
611 CV to PV. b, M06 score by Layer1-9 in young and aged sections. c, Hepatocyte-adjusted clock
612 and d, myeloid markers by layer. e, Per-section rho versus zonation. f, Within-zone M06-myeloid
613 rho, CV/mid/PV bins. g, Donor-level rho (95% CI; n=4) for M06, abundance-/composition-
614 adjusted M06, myeloid markers, hepatocyte- and cellularity-adjusted clock; one-sample P versus
615 zero. Cross-section permutation P=0.001; Moran's I 0.24-0.38 (M06), 0.07-0.24 (clock), P=0.002.

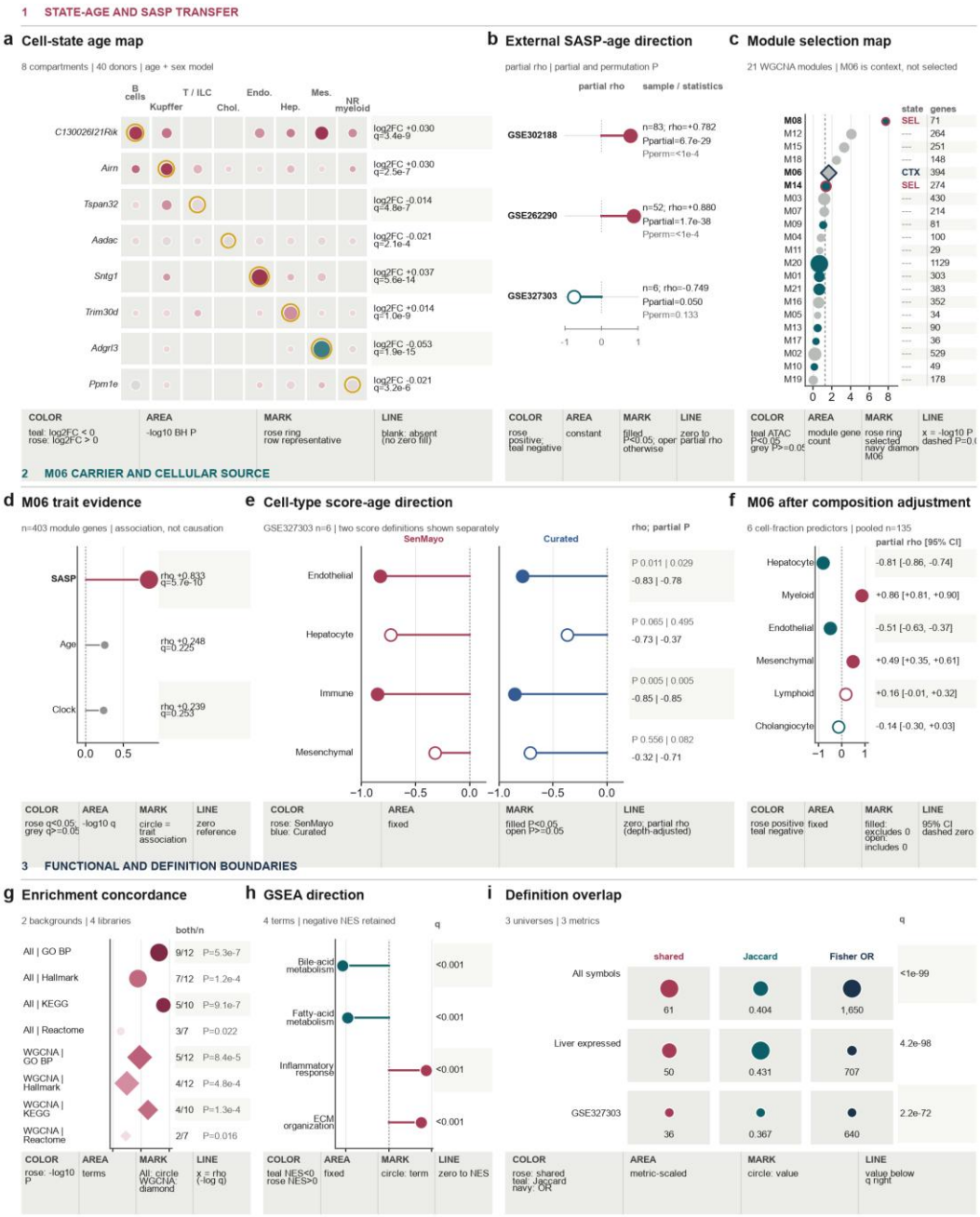

Fig. 2 | Cell-state age mapping and M06-SASP. a, Cell-state age map, eight compartments (73,481 tests; 40 donors; age + sex). b, Age-SenMayo partial Spearman rho, three cohorts. c, Age association, 21 WGCNA modules. d, M06-SASP/age/clock associations (n=403 genes; rho, q). e, GSE327303 cell-type direction audit (six donors; confounded). f, Composition-adjusted M06 associations, six cell fractions (n=135; partial rho, 95% CI). g, SASP-SenMayo enrichment concordance. h, GSEA NES, four prespecified terms. i, SenMayo-Curated overlap (shared genes, Jaccard, Fisher OR).

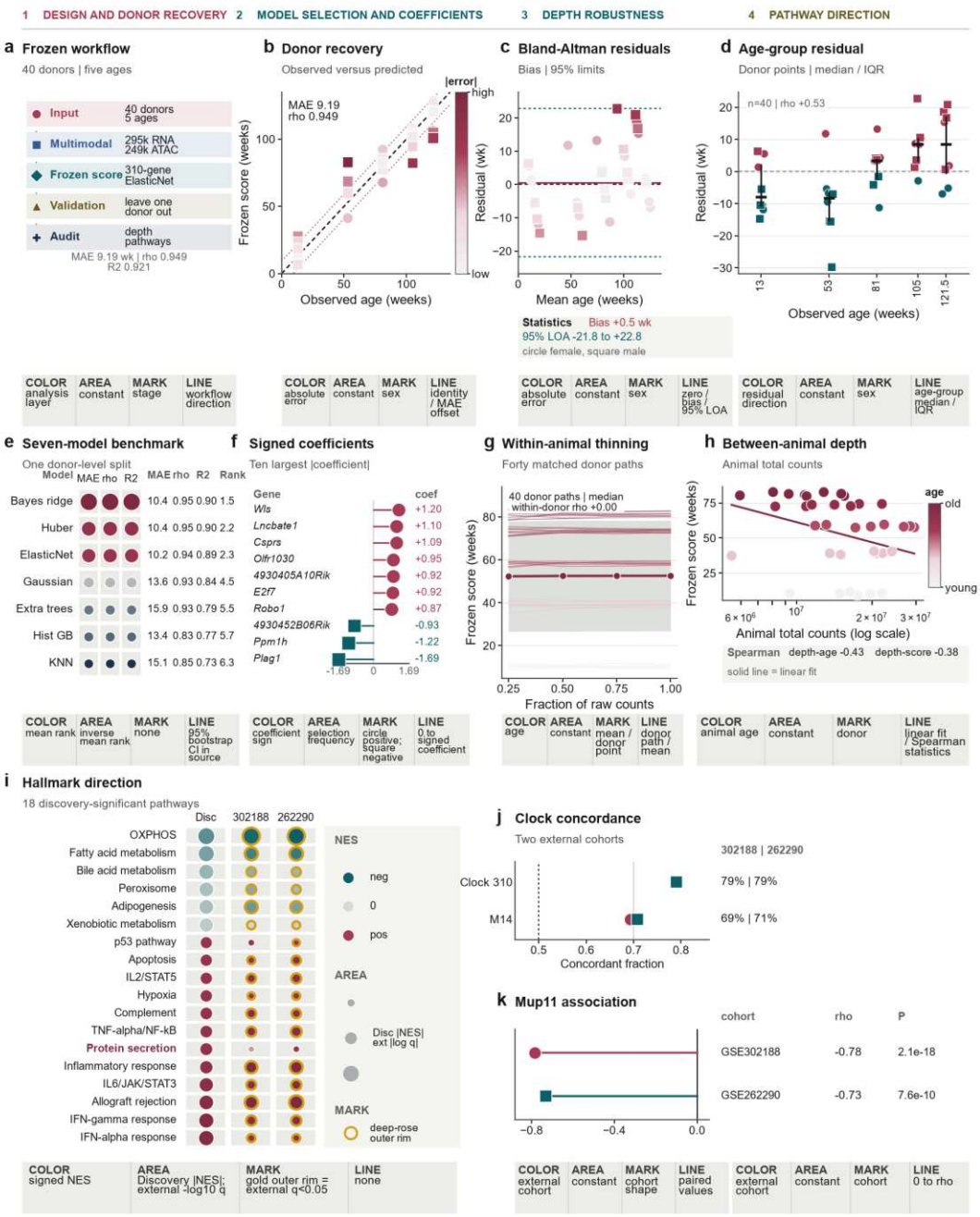

624

625 Fig. 3 | A rank-accurate hepatocyte clock. a, Frozen workflow: 40 donors, five ages, RNA/ATAC,
626 310-gene ElasticNet. b, Observed versus predicted age, held-out donors, MAE. c, Bland–Altman
627 residuals: bias, 95% limits. d, Residuals by age, medians, IQRs. e, Seven-model benchmark:
628 MAE, rho, R^2. f, Ten largest signed coefficients. g, Depth thinning; median within-donor rho. h,
629 Between-animal depth; depth-score correlation. i, Hallmark direction, discovery, GSE302188,
630 GSE262290; external P<0.05. j, Clock versus M14 concordance. k, Mup11 age association rho
631 and P.

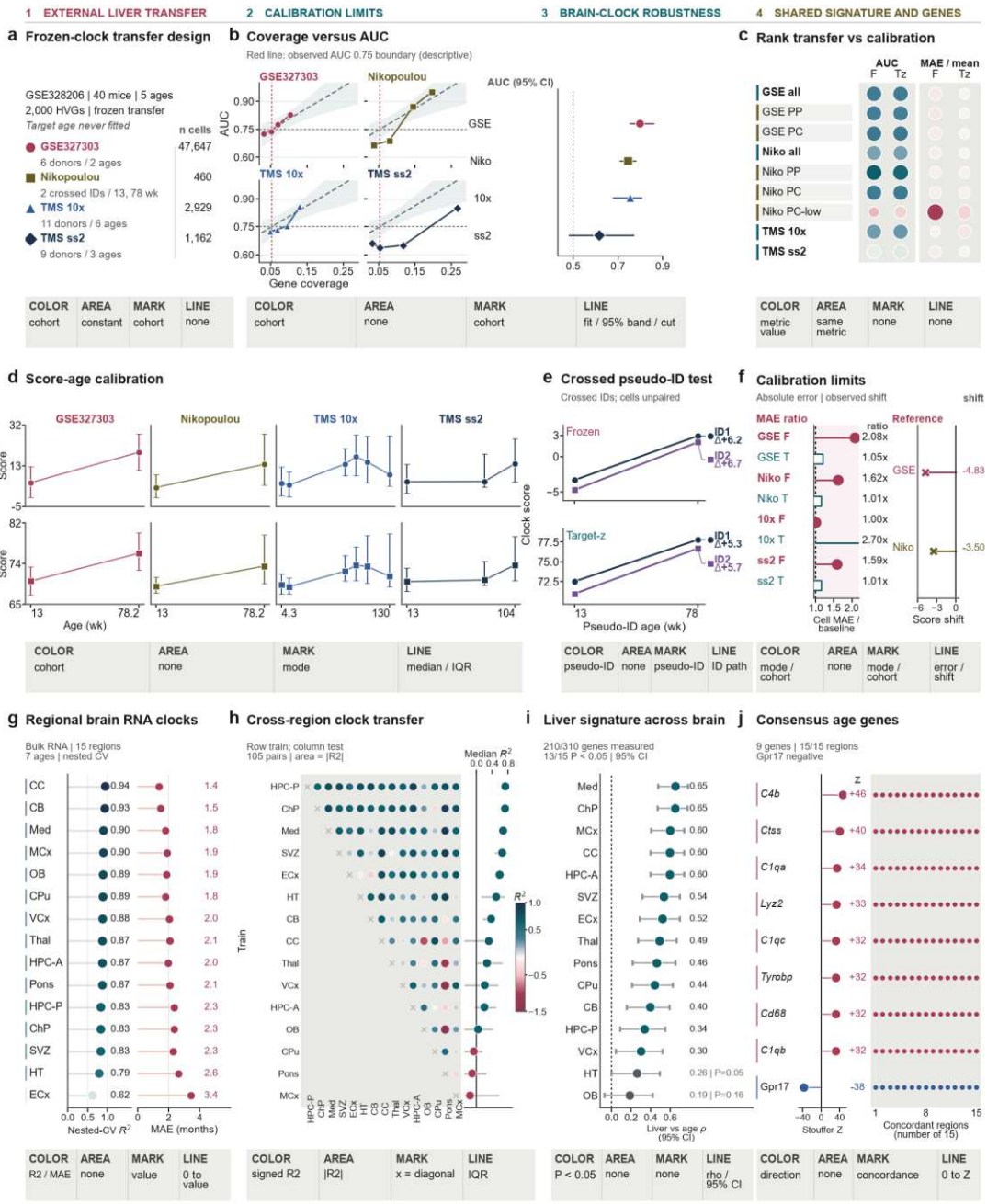

632

633 Fig. 4 | Partial frozen liver-age transfer; region-dependent brain clocks. a, External liver validation
634 (GSE327303, Nikopoulou, TMS 10x/ss2), frozen scores. b, Coverage versus cell AUC (0.75);
635 whole-cohort AUC, 95% CI. c, Transfer AUC, cell-MAE ratio; frozen versus target-z. d, Score-age
636 medians, IQR. e, Crossed pseudo-ID test. f, Calibration limits; old-minus-young pool shift. g,
637 Nested cross-validated R2 and MAE, 15 regions, seven ages. h, Cross-region transfer R2. i,
638 Liver-signature rho by region; P<0.05. j, Stouffer Z, concordant regions, nine genes.

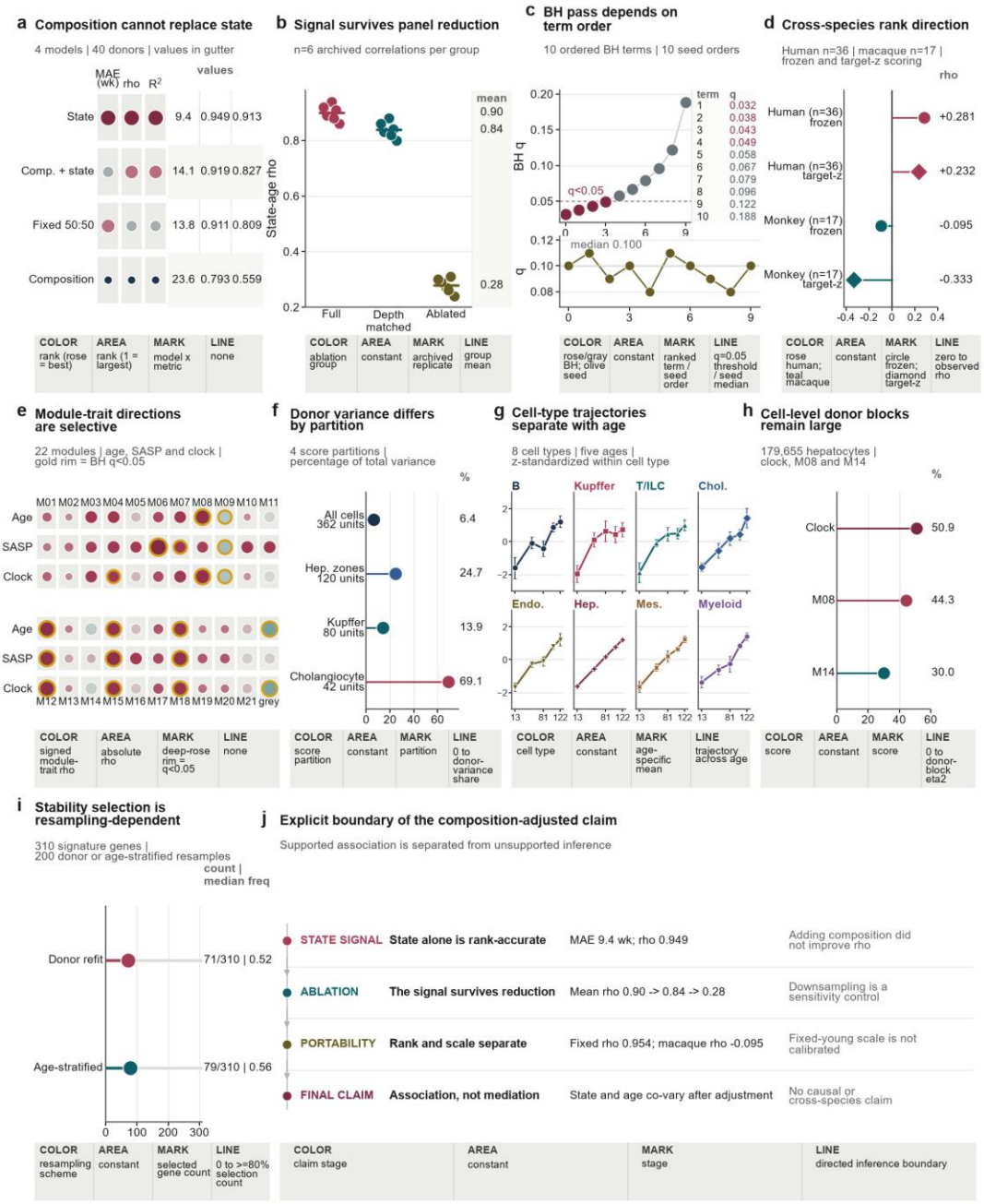

Fig. 5 | Composition adjustment preserves a state-age signal. a, Four prespecified composition/state models, 40 donors; MAE, rho, R^2. b, Six state-age rho per set: full, depth-matched, ablated. c, BH q, ten terms; seed-order medians. d, Human (n=36), macaque (n=17) rho, frozen/target-z. e, 22 module-trait rho; BH q<0.05. f, Donor-block variance share, four partitions. g, Eight cell-type trajectories; age-specific means ± SEM. h, Donor-block eta², clock/M08/M14; 179,655 hepatocytes. i, 310-gene selection, 200 donor/age-stratified resamples, >=80%. j, Claim-evidence boundary.

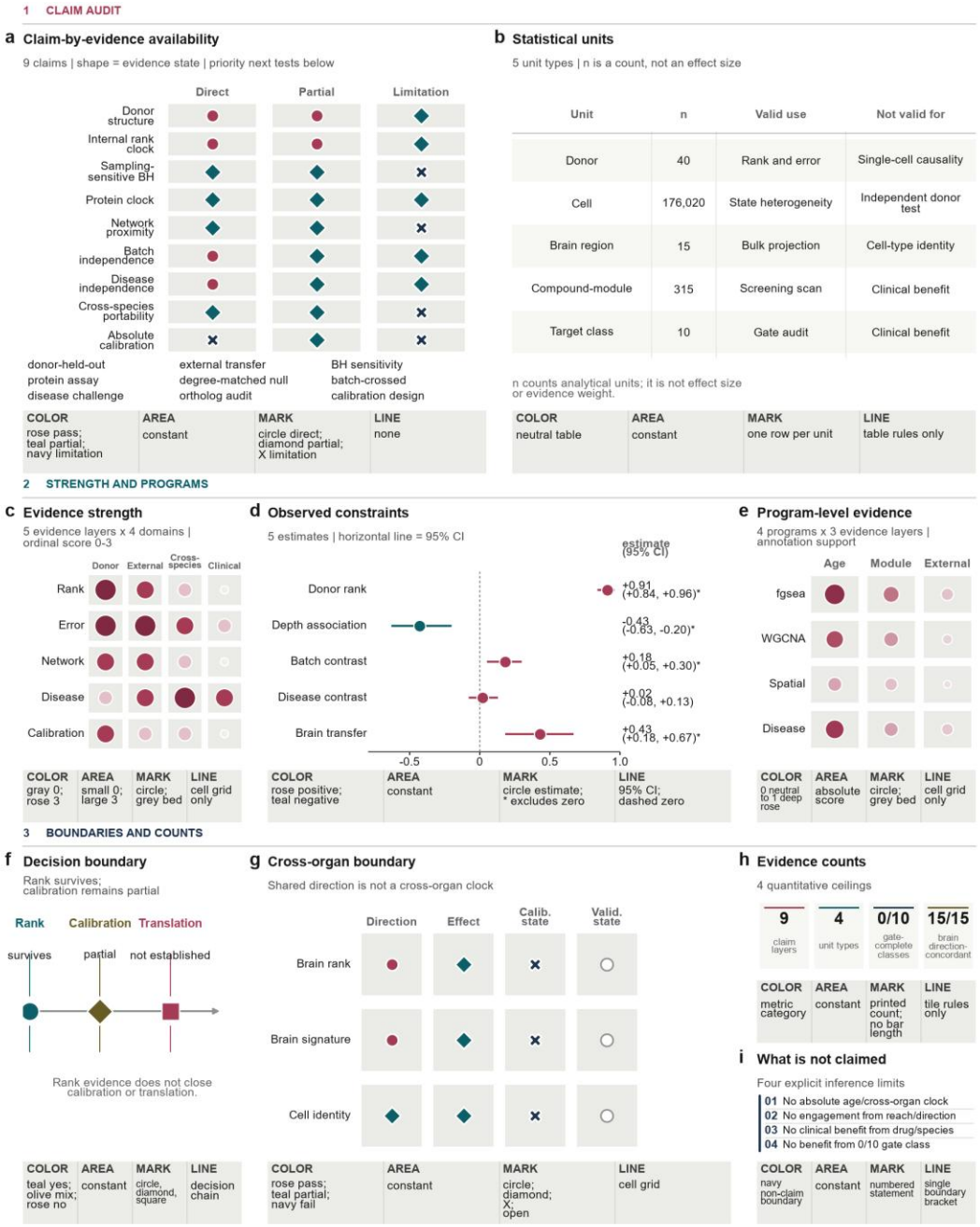

Fig. 6 | Evidence availability and limits. a, Claim-by-evidence availability, nine claim layers, next tests. b, Units: donor 40, cell 176,020, region 15, module 315, class 10. c, Evidence strength: five-layer/four-domain 0-3. d, Five constraints, 95% CI; asterisk, excludes zero. e, Program evidence: four-program/three-layer 0-1. f, Decision boundary: rank evidence, partial calibration, translation. g, Cross-organ boundary: direction, effect, calibration, validation. h, Ceilings: nine layers, four units, 0/10 gate-complete, 15/15 brain-concordant. i, Inference limits: absolute age, cross-organ transfer and clinical benefit.

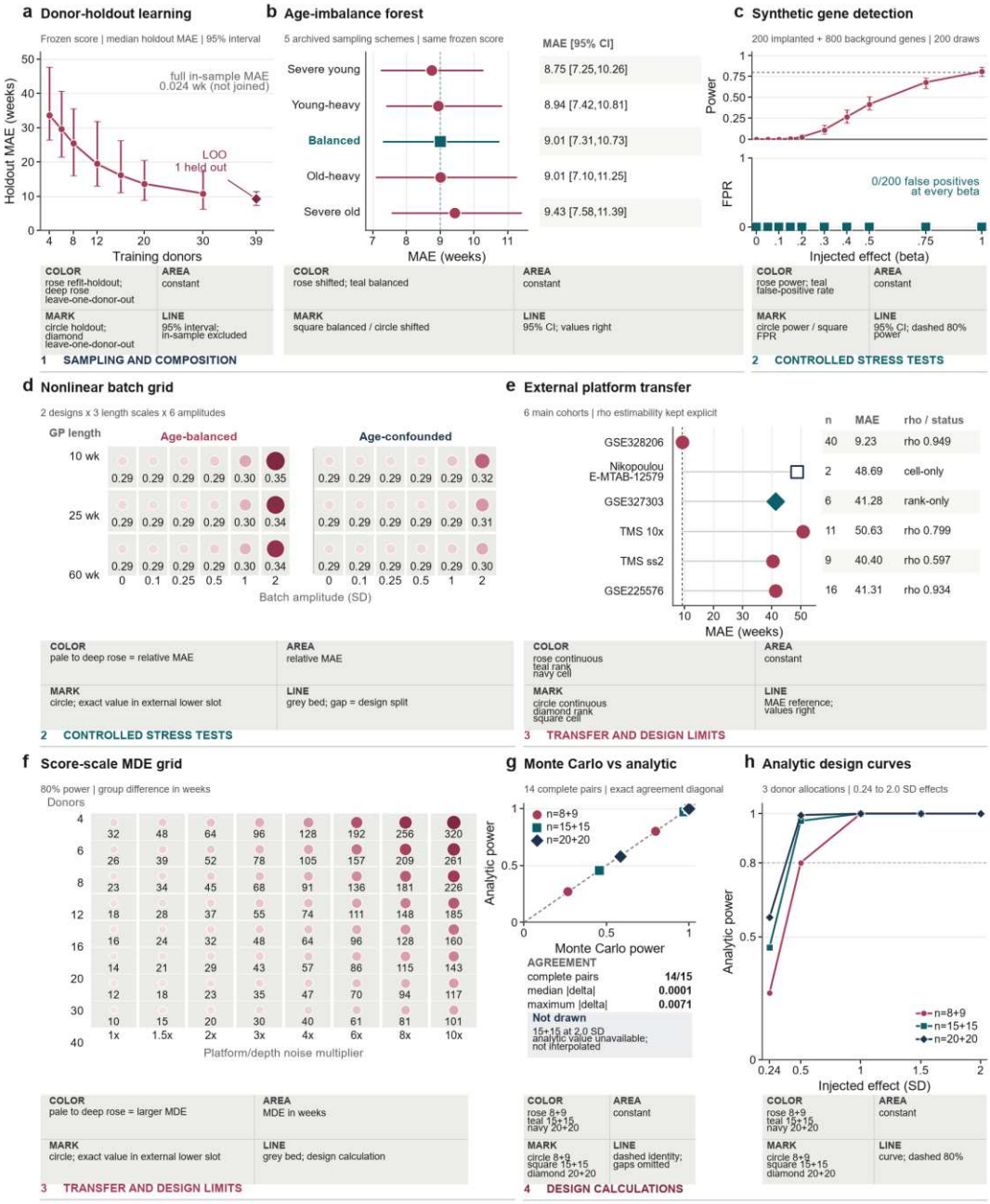

Fig. 7 | Sampling, transfer and intervention-design limits. a, Donor-holdout MAE learning curve; diamond, leave-one-out (39 training, 1 held out). b, MAE across age-imbalance schemes (medians, 95% intervals). c, Synthetic detection power; FPR 0/200. d, Relative MAE, six batch amplitudes x three length scales. e, External transfer: donor-level rho, rank-only cohorts, one cell-level-only cohort. f, Minimum detectable effect, 4-40 donors x 1-10-fold noise. g, Monte Carlo vs analytic power, 14 complete pairs. h, Power, 8+9, 15+15, 20+20 designs; 80% threshold.

Extended Data legends

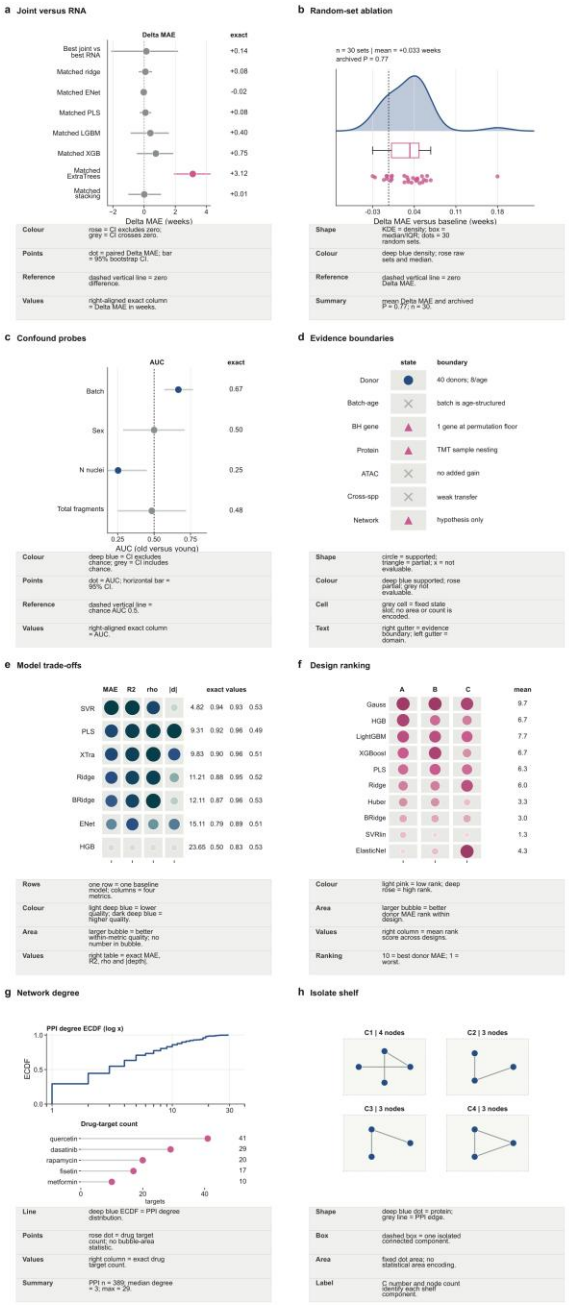

664

665 Extended Data Fig. 1 | Data overview and ceilings. a, RNA versus ATAC nuclei (rho=0.95, 95%
666 CI 0.89-0.97). b, Donor composition (n=40): age, batch, cell-type fractions. c, Old-versus-young
667 AUC versus gene coverage; 0.75 threshold. d, Depth correlation versus MAE across models; A/B
668 regimes. e, Score shift, young- versus old-majority cells. f, P values, 3,000 versus 10,000 nulls;
669 Mup1, Mup11. g, Human and macaque rho, AUC. h, Protein clock (n=16 TMT): cross-validated
670 MAE in months, eight models.

671

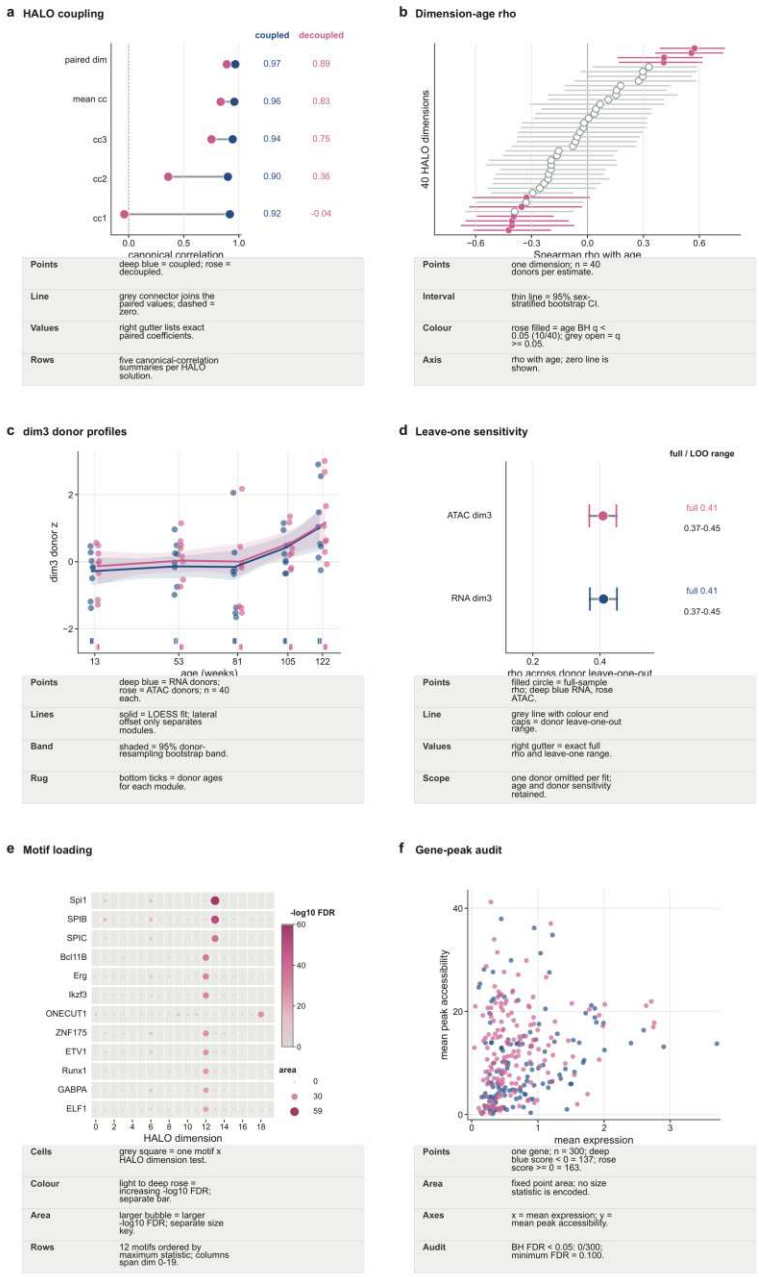

672

673 Extended Data Fig. 2 | Ablation, confounds, benchmarks and networks. a, Joint RNA+ATAC delta
674 MAE versus RNA-only, eight models; positive, worse. b, 30 random gene sets, delta MAE (mean
675 +0.03 weeks; P=0.77). c, Old-versus-young AUC, batch, sex, nuclei number, fragments; 0.5
676 reference. d, Claim versus boundary codes across seven analyses. e, MAE, R2, rho, depth score,
677 six models. f, Mean rank, ten models, three criteria. g, PPI degree ECDF (n=389); drug target
678 counts. h, PPI modules, four drugs.

679



Extended Data Fig. 3 | Exploratory HALO, motif loading and gene–peak audit. a, HALO coupling: canonical correlations, cc1–cc3, mean and paired coupled/decoupled dimension. b, Dimension–age Spearman rho, 40 HALO dimensions; filled, coupled; open, decoupled; 95% CI. c, Dimension-3 donor profiles, RNA and ATAC (z-score versus age; LOESS). d, Leave-one-donor-out rho range, dimension 3 (0.41). e, Transcription-factor by HALO-dimension loading (−log10 FDR). f, Peak accessibility versus expression, 300 genes; negative-score fraction 0.46.

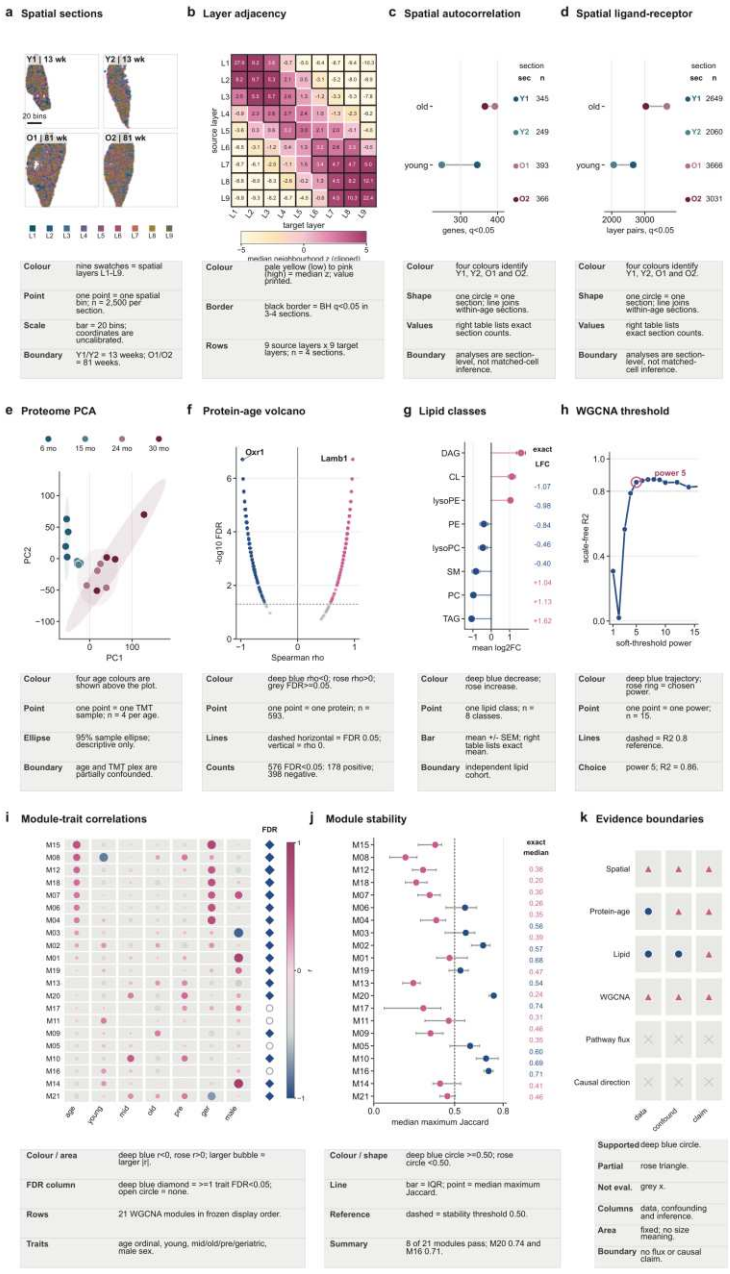

Extended Data Fig. 4 | Communication annotations and exploratory evidence matrix. a, CellChat and matched-cell totals as percentage of young values across ages; 100% and 50% references. b, CellPhoneDB significant ligand-receptor pairs across ages. c, CPDB-squidpy, CC-squidpy and CC-CPDB concordance across age groups. d, Delta information flow (geriatric minus young) by pathway. e, Claim-evidence matrix for five analyses: HALO donor-level; motif enrichment descriptive; communication dataset-dependent; spatial section-level; direction open.

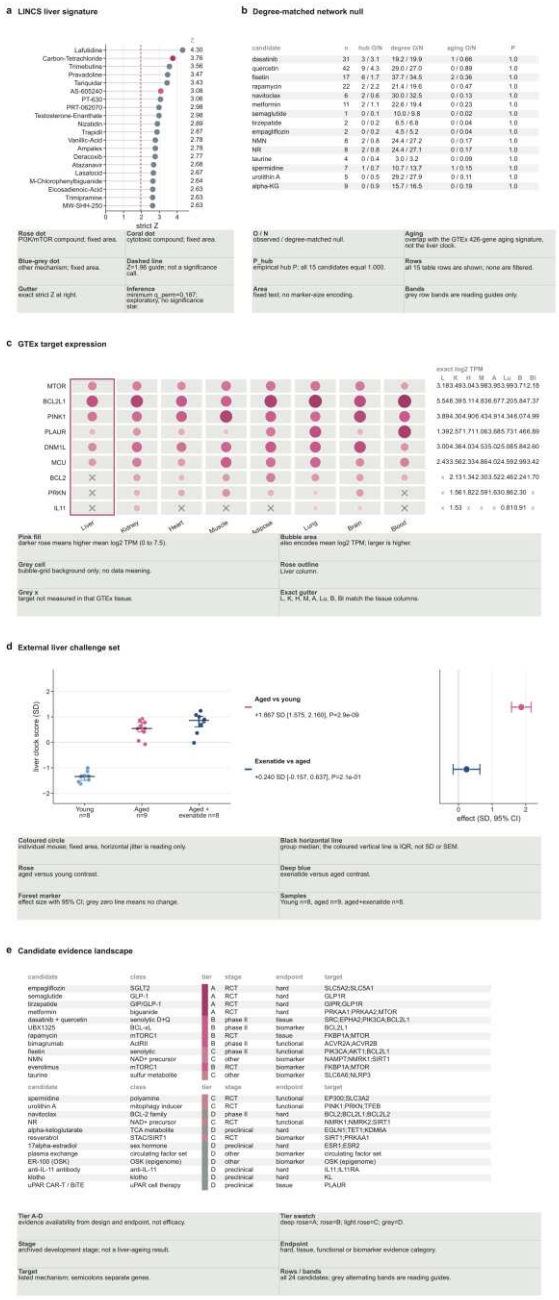

Extended Data Fig. 5 | Spatial, omics and WGCNA. a, Sections O1, O2, Y1, Y2, 10-um. b, Layer neighbourhood z, L1-L9. c, Autocorrelated genes (q<0.05). d, Spatial ligand-receptor layer pairs. e, Proteome PCA, age (6, 15, 24, 30 months). f, FDR versus age rho. g, Lipid log2FC, old minus young. h, Soft-threshold R2 versus power; 0.8. i, Module-trait correlations. j, Module Jaccard stability (median, IQR). k, Evidence class: section-level spatial; TMT-nested protein; independent lipid; 8/21 modules stable.

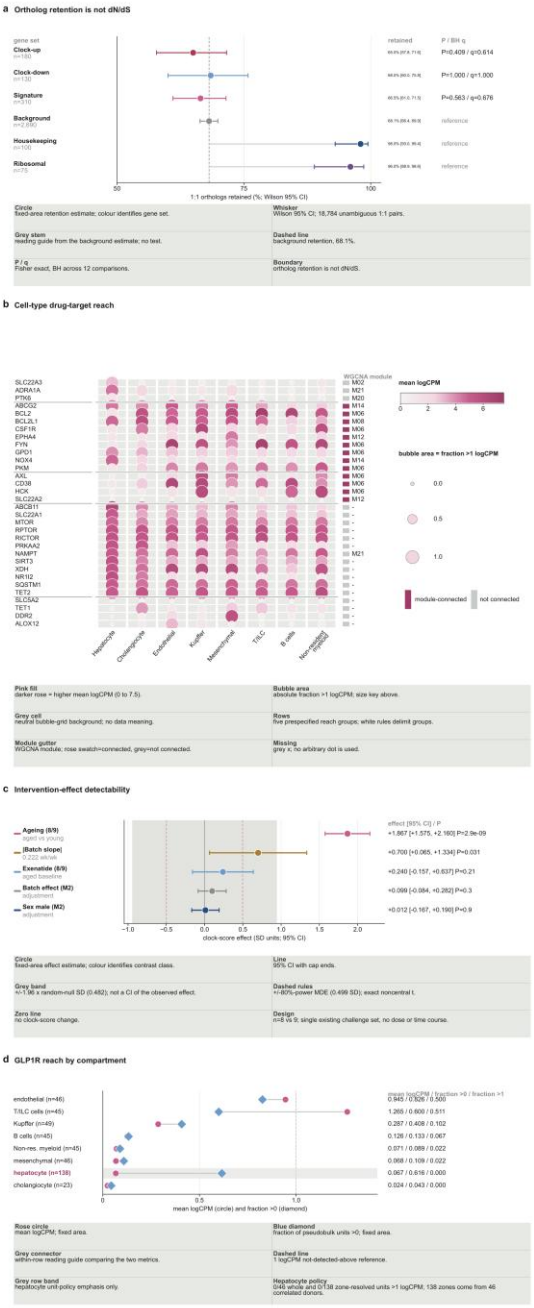

Extended Data Fig. 6 | Pharmacology and translation readiness. a, LINCS top 20 by strict Z (minimum q_perm=0.187). b, Degree-matched network null (hubs, degree, ageing overlap; n=15). c, GTEx target expression, eight tissues; six measured (n.m., not measured). d, GSE280382 AgedLT challenge (young n=8, aged n=9, aged + exenatide n=8): clock score (P=2.9e-9 aged versus young; P=0.215 exenatide versus aged); contrasts +1.87 SD and +0.24 SD (95% CI). e, Evidence tiers for 24 candidates.

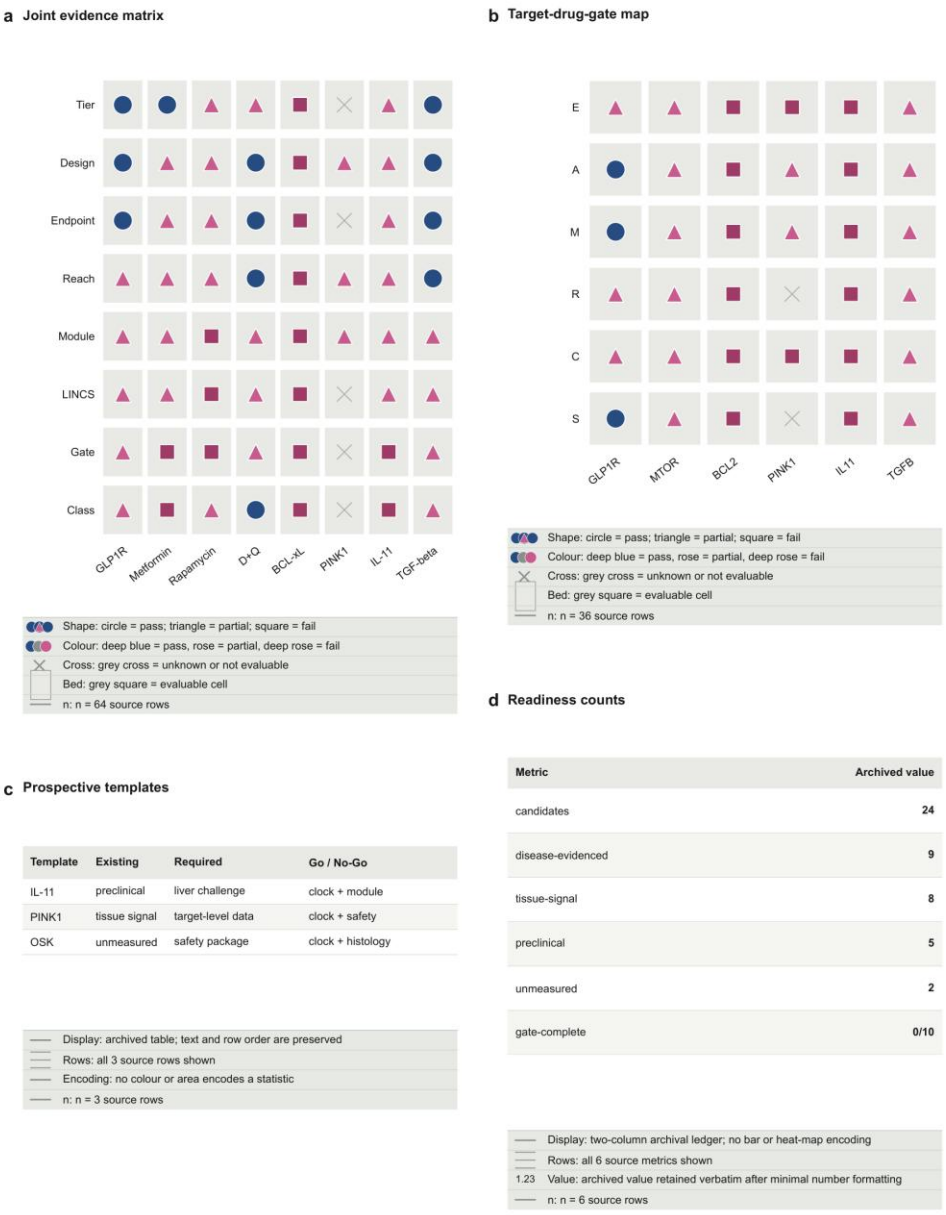

Extended Data Fig. 7 | Cell-type reach, detectability and GLP1R. a, Ortholog retention, clock-up (n=180), clock-down (n=130), signature (n=310), background (n=2,690), housekeeping (n=100), ribosomal (n=75); 95% CI, Fisher P, BH q. b, Drug-target reach: mean logCPM, fraction >1 logCPM, eight compartments; WGCNA module. c, Clock-score effects (SD; 95% CI) for ageing, batch-slope discordance, exenatide, batch, sex; 80%-power MDE 0.499 SD. d, GLP1R expression by compartment; no hepatocyte unit >1 logCPM (0/138; 0/46).



720

721 Extended Data Fig. 8 | Joint evidence matrix, target–drug–gate map and pre-registration
722 templates. a, Matrix for 24 candidate interventions; eight evidence-availability columns, not
723 efficacy (tier, design, endpoint, liver-target expression, module connection, LINCS, six-gate status,
724 applicability). b, Target–drug–gate map, 15 profiled drugs against six gates (E expression, A age,
725 M module, R reversal, C endpoint, S safety); 175 drug–target pairs, 148 unique targets. c, Pre-
726 registration templates for anti-IL-11, PINK1, OSK: existing and required data, clock-score
727 endpoint, Go and No-Go rules.

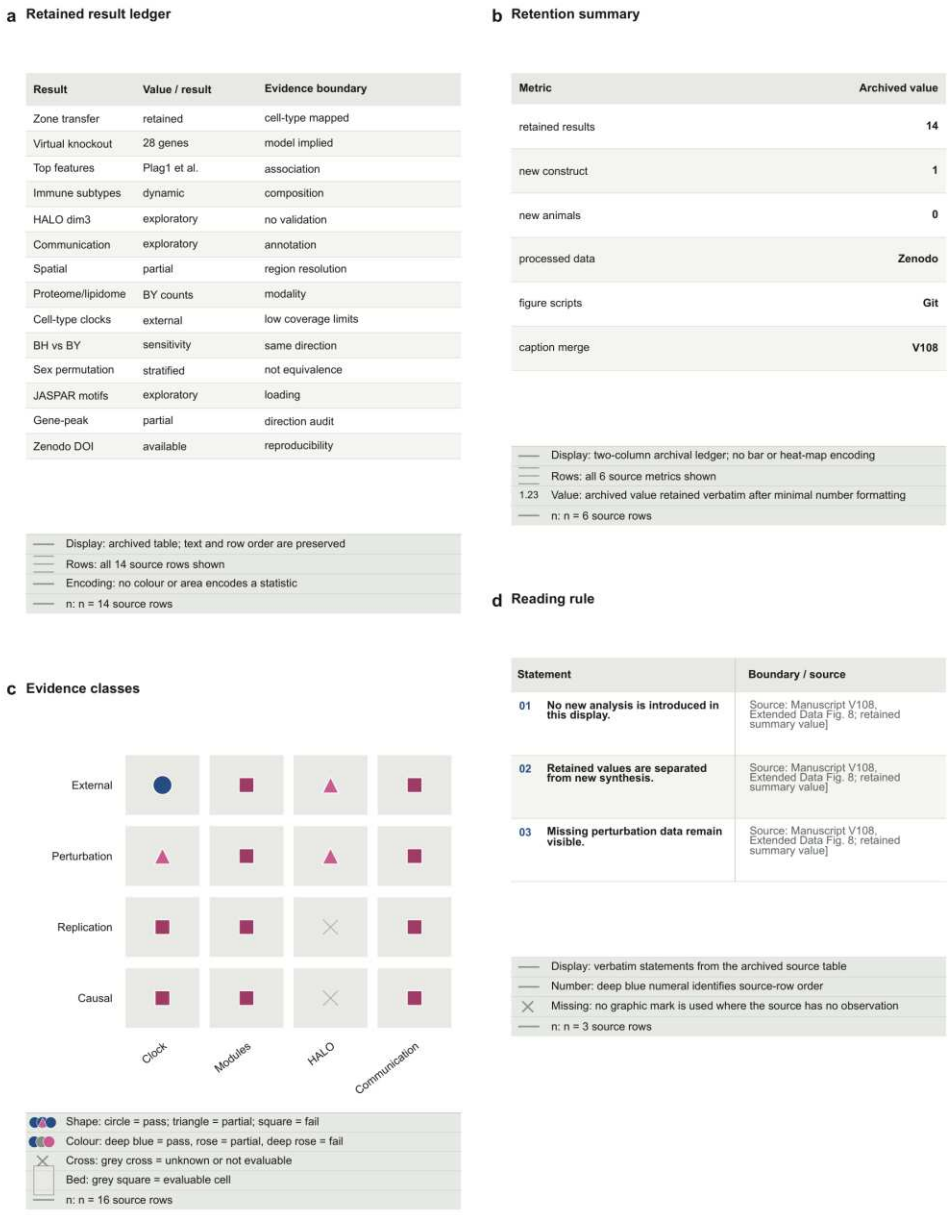

728

729 Extended Data Fig. 9 | Causal identifiability of the liver ageing design. a, Assumed causal
730 structure: Age and Batch point to State, Batch a deterministic function of Age; Depth and
731 Composition cause State; sex adjusted; observational design. b, Design rank versus parameter
732 count, seven design matrices. c, Exact null-space (alias) vectors, Xv=0 verified to machine
733 precision. d, Age-versus-batch decomposition is likelihood-flat for the clock score: all points
734 reproduce the same fitted values, RSS, log-likelihood and R2 (0.9329).

735

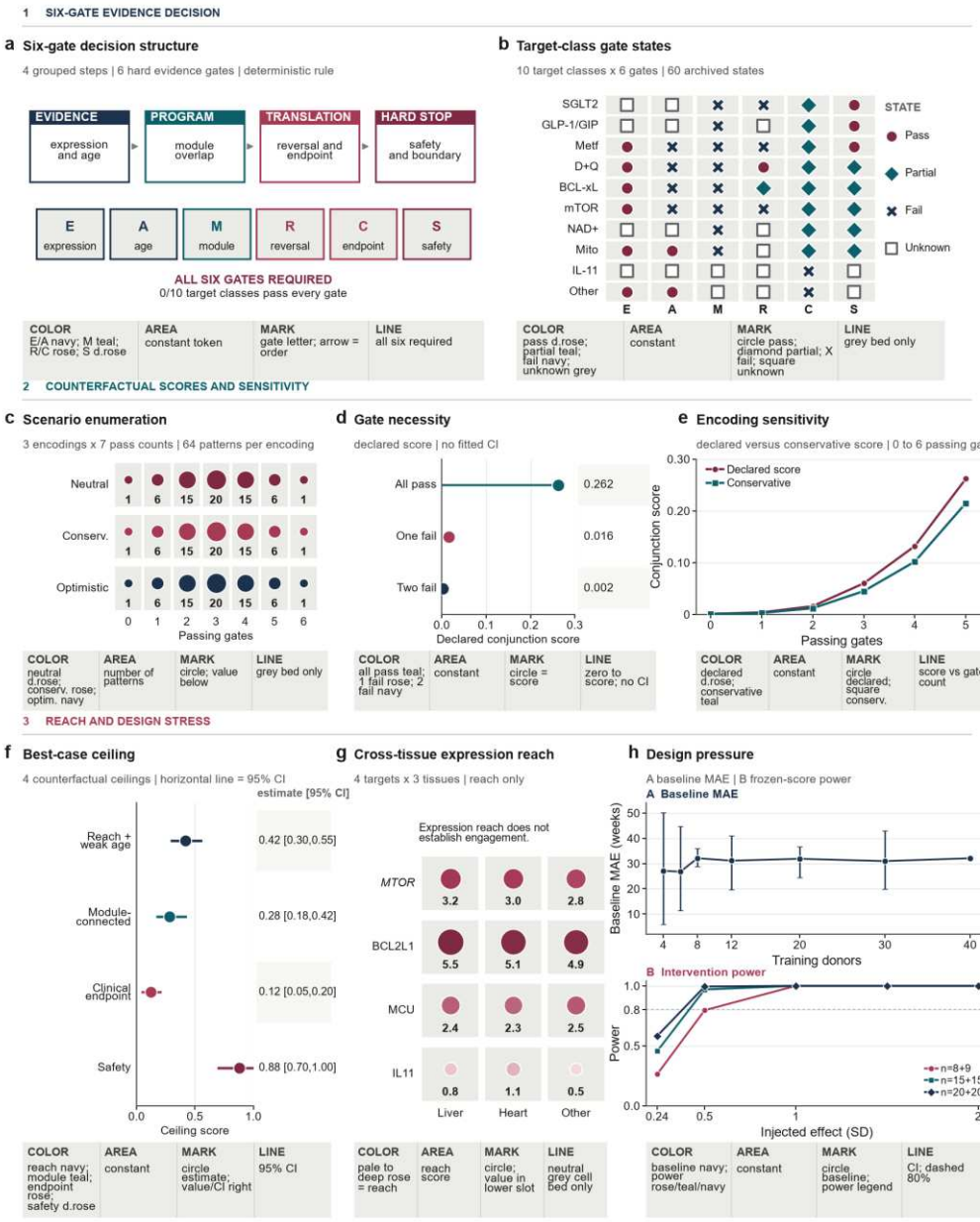

Extended Data Fig. 10 | Earlier results retained in this manuscript. Table of the 14 earlier results with key values and evidence boundaries: zone-resolved transfer, 28-gene virtual knockout, top features (Plag1 etc.), immune-subtype dynamics, HALO dim3, communication, spatial, proteome/lipidome BY counts, multi-cell-type clocks, BH-vs-BY sensitivity, sex-stratified permutation, JASPAR motifs, gene-peak direction and Zenodo DOI. All values are the retained earlier results.

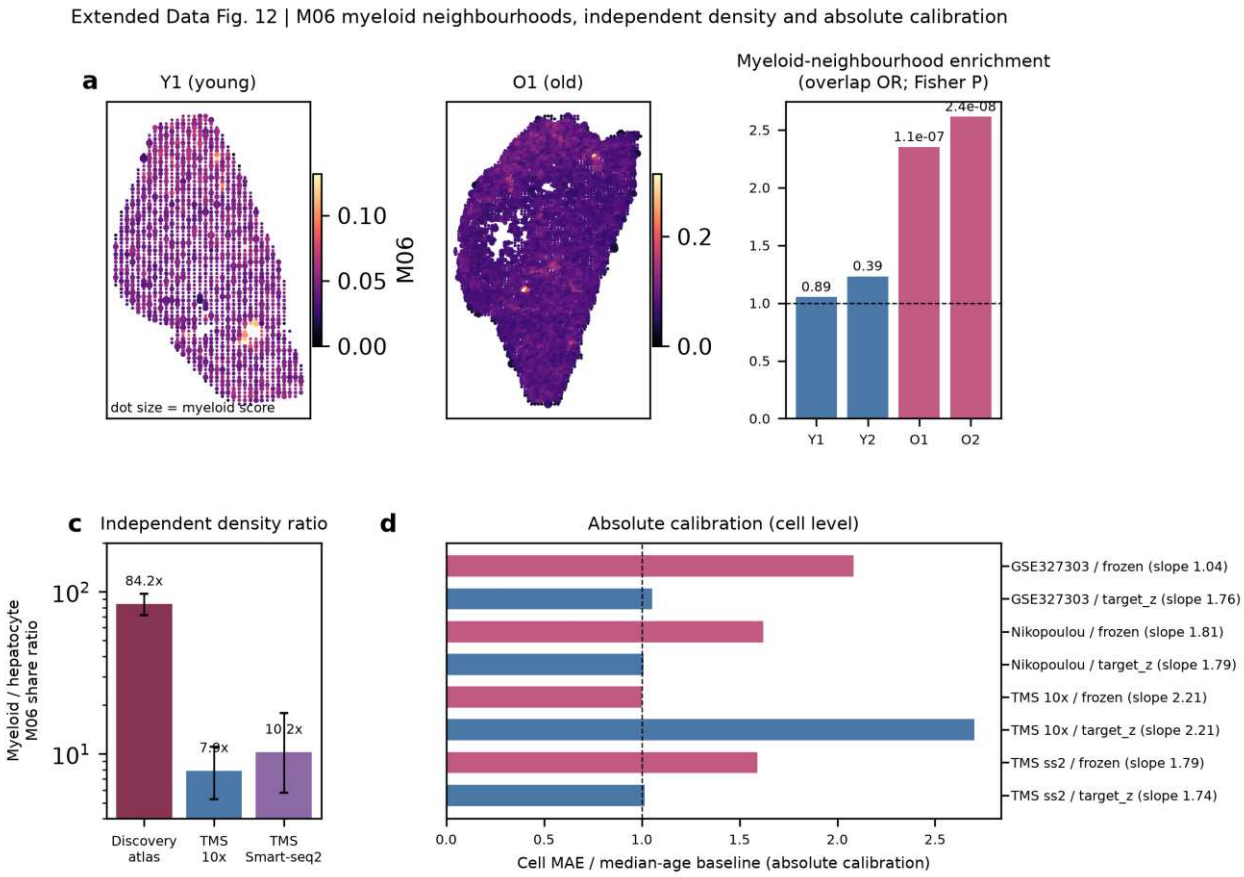

743

744 Extended Data Fig. 11 | Six-gate decisions and design pressure. a, Six-gate structure. b, 10×6
745 gate matrix; 12 pass, 14 partial, 17 fail, 17 unknown; 0/10 clear all. c, 64 patterns, three
746 encodings; all-pass alone clears. d, Necessity 0.262 (all pass), 0.016 (one fail), 0.002 (two fail). e,
747 Encoding sensitivity, 0–6 gates; order preserved. f, Counterfactual ceilings, 95% intervals. g,
748 Cross-tissue reach: MTOR, BCL2L1, MCU, IL11. h, A, baseline MAE by training size; B, Monte
749 Carlo power, 80% threshold.

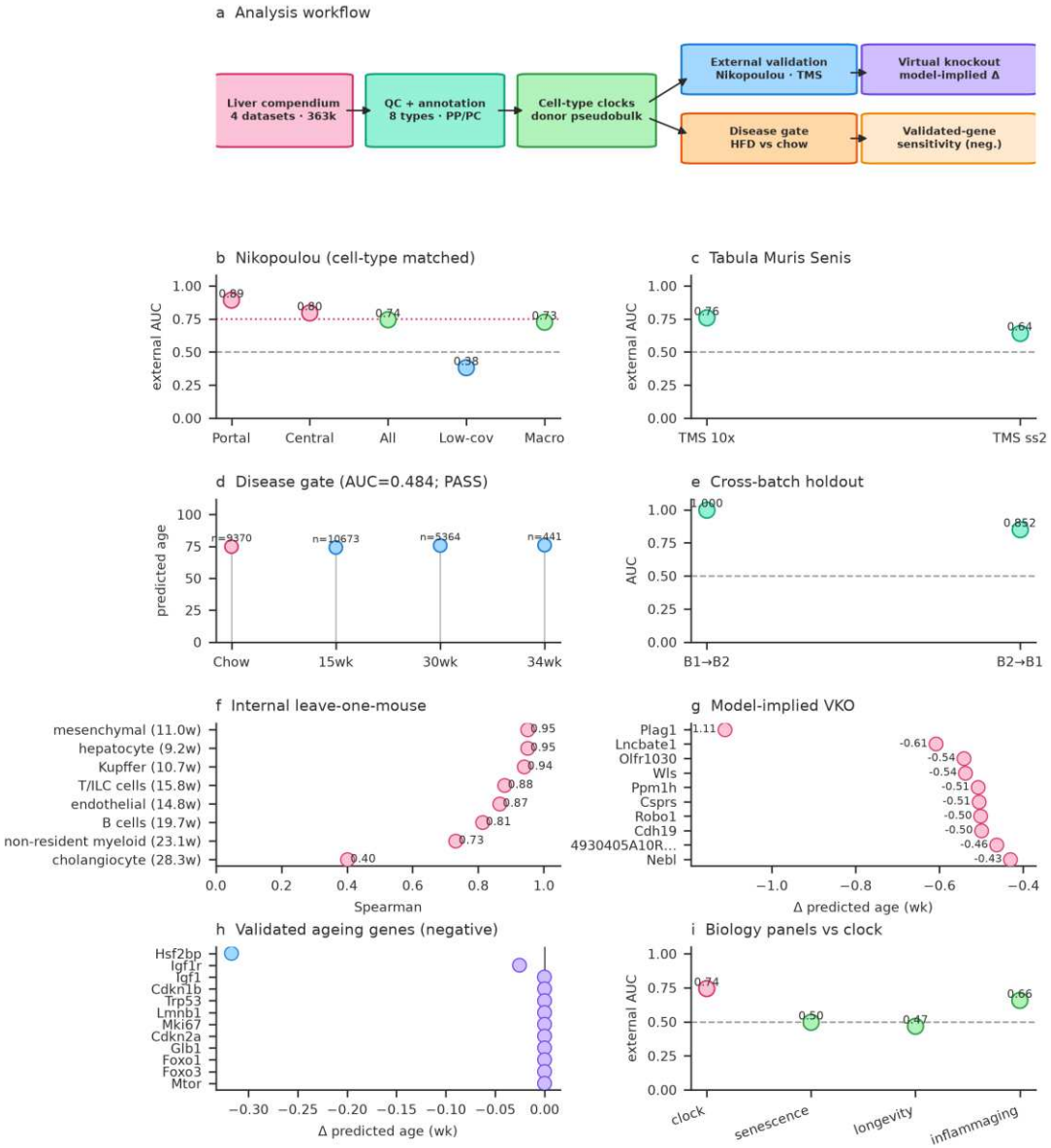

Extended Data Fig. 12 | M06 spatial neighbourhoods and absolute external calibration. a, GSE328448 sections (young Y1, old O1); M06 score and independent myeloid marker score. b, M06-high versus myeloid-high bin overlap OR, Fisher P; two young, two old sections. c, Myeloid-to-hepatocyte M06 share ratio: atlas 84.2× (95% CI 71.5–97.5), TMS liver 7.9× (5.2–11.1), Smart-seq2 10.3× (5.8–17.8); log scale. d, MAE relative to median-age baseline, eight cohort × mode evaluations; >1.0 worse; slope (perfect = 1).

Detailed panel definitions, pre-registration criteria and identifiability proofs for ED7–ED9 and Supplementary Fig. 28 are provided in Supplementary Notes 1–4 (separate file).

Supplementary Figure legends

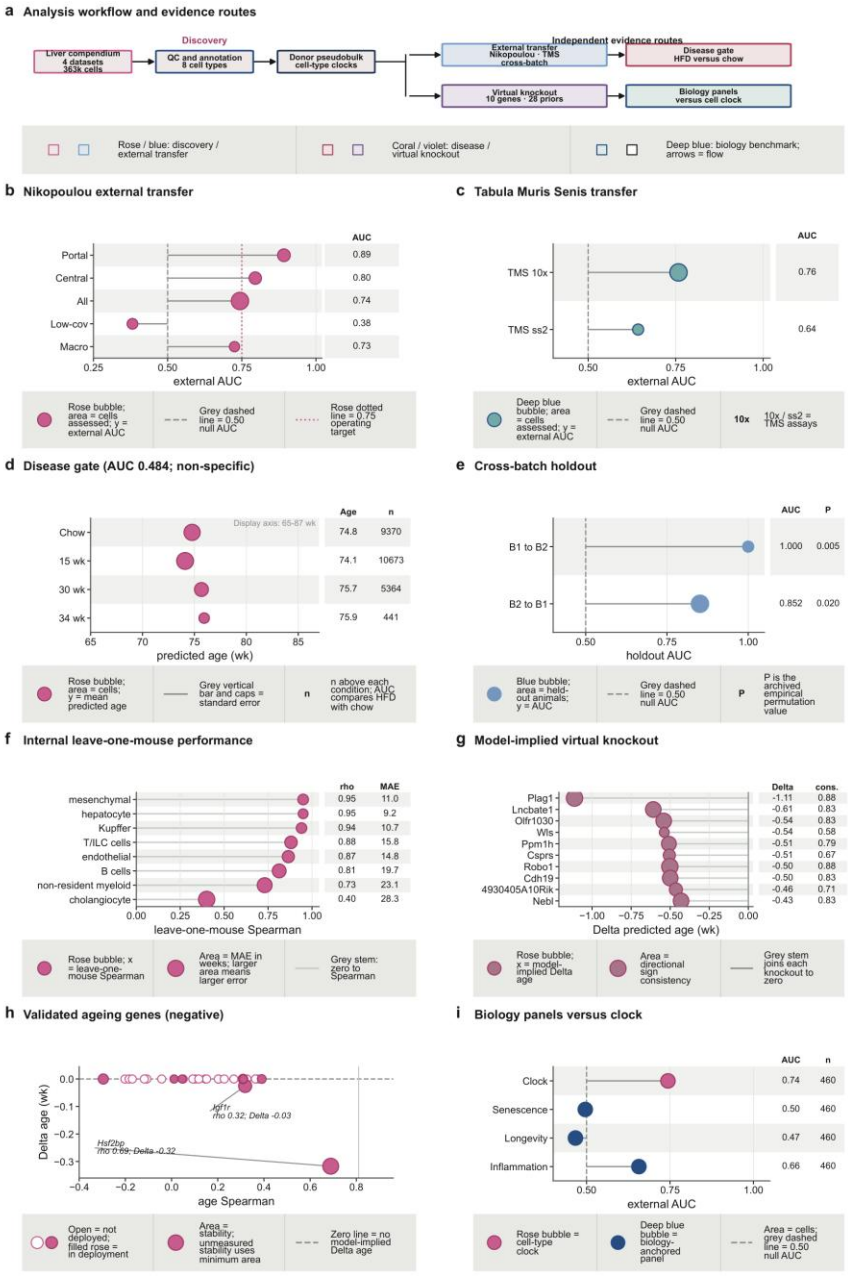

760

761 Supplementary Fig. 1 | Cell-type-resolved ageing clocks: external transfer, disease specificity and
762 the limits of data-driven scores. a, Workflow. b, External AUC by hepatocyte population (E-MTAB-
763 12579, cell-type matched; low-coverage cells fail). c, External AUC, Tabula Muris Senis liver. d,
764 Disease-specificity gate (GSE166504; HFD versus chow, AUC 0.484). e, Cross-batch holdout
765 (Batch_01↔Batch_02). f, Internal leave-one-mouse performance per cell type. g, Virtual-
766 knockout delta. h, Sensitivity of 28 literature-validated ageing genes (only Hsf2bp). i, Biology-
767 anchored panel scores versus clock.

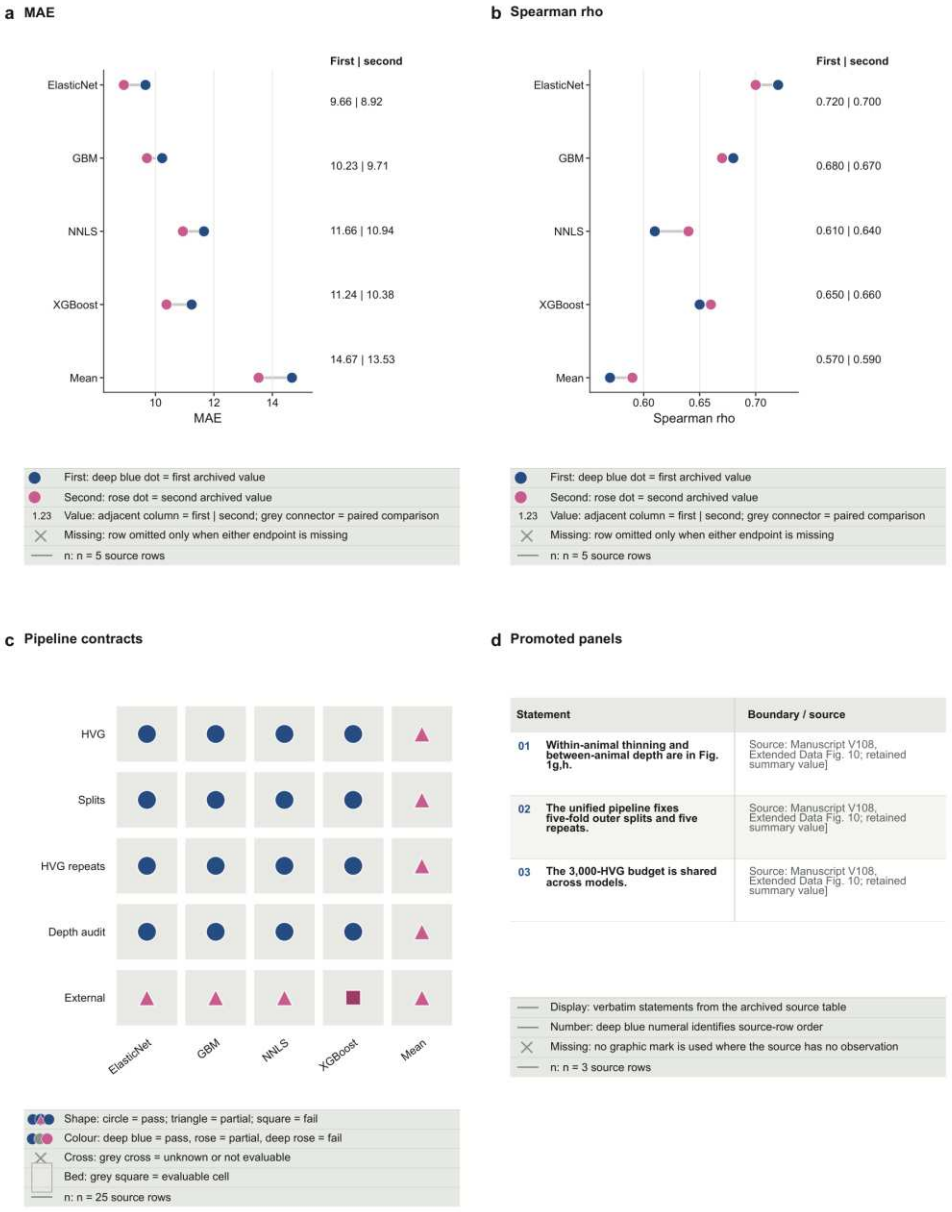

768

769 Supplementary Fig. 2 | Unified donor-level pipeline. a, Five donor-level models with fixed five-fold
770 x five-repeat outer splits and the same 3,000-HVG budget: MAE. b, Spearman rho. The within-
771 animal thinning and between-animal depth panels are promoted to Fig. 3g,h; full curves are in the
772 source tables.

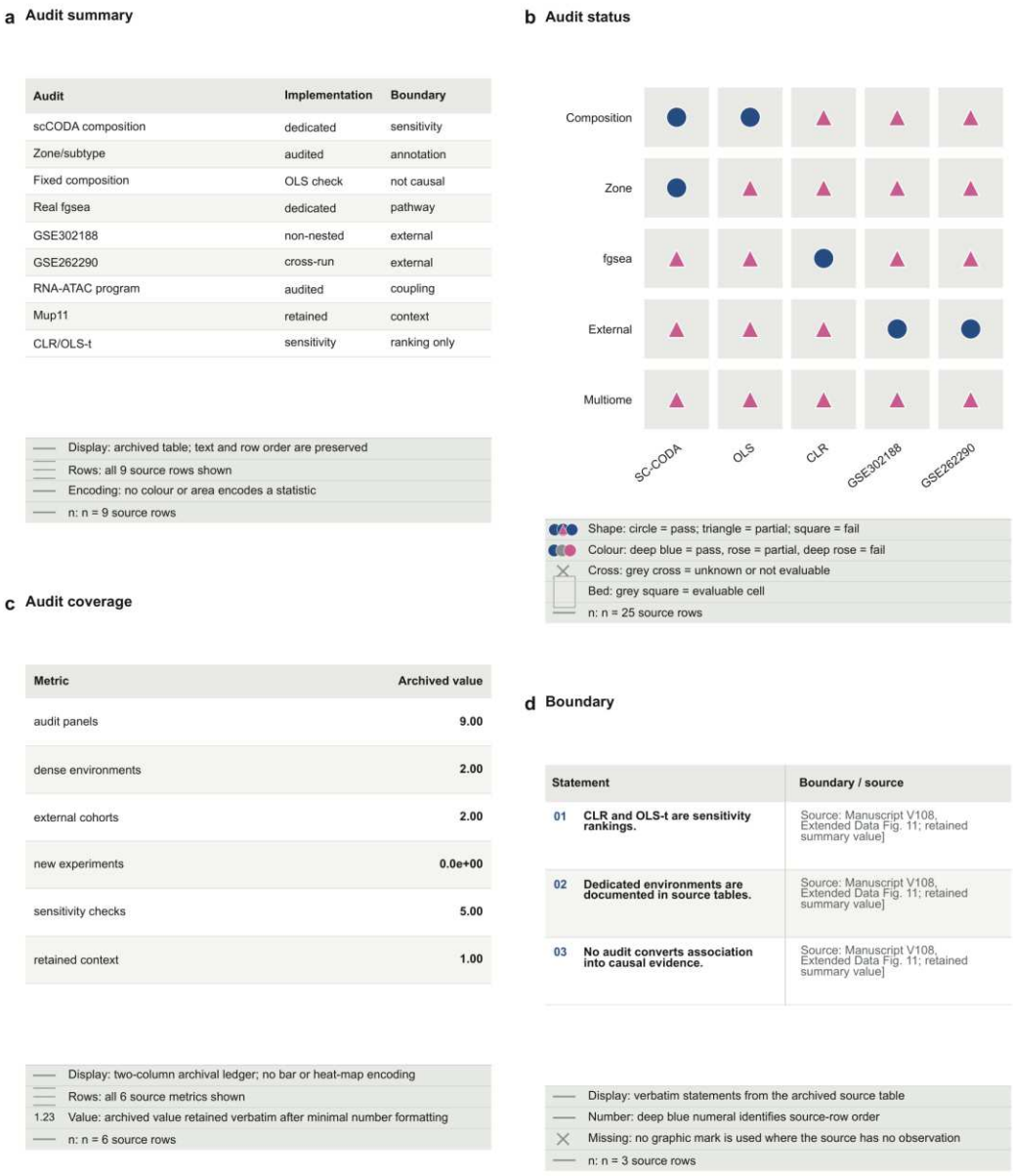

Supplementary Fig. 3 | Donor-level D-I audits. a, Summary of scCODA composition, zone/subtype, fixed-composition, real fgsea, non-nested cohort (GSE302188), cross-run cohort (GSE262290), RNA-ATAC programme and Mup11 audits, with key values and evidence boundaries. scCODA and fgsea were run in dedicated environments; CLR and OLS-t rankings are sensitivity checks.

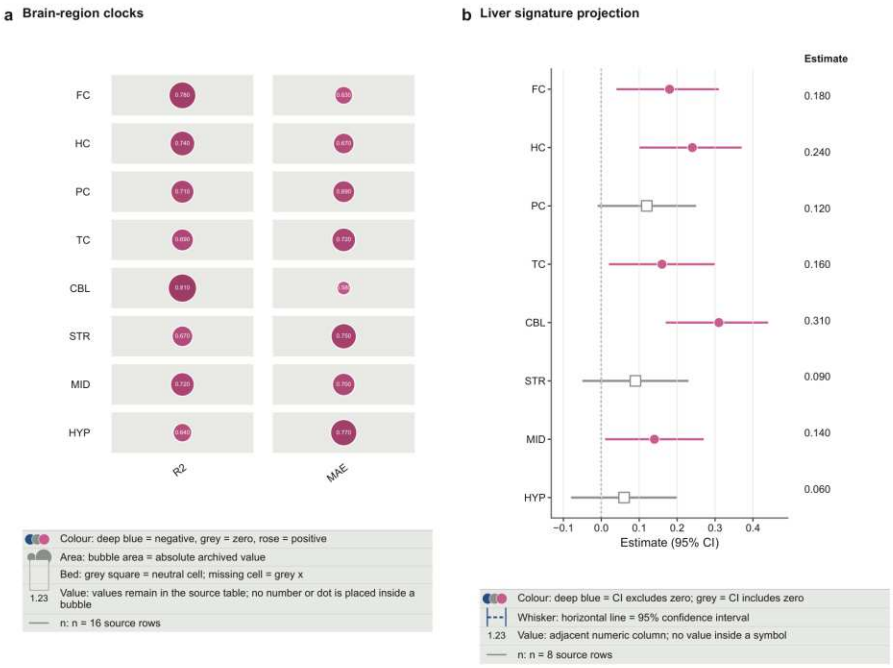

c Consensus age genes

Gene	Direction	Regions
Ctss	up	13/15
C1qc	up	12/15
Gpr17	down	11/15
Lcn2	up	10/15
Mup11	unresolved	n.a.

Display: archived table; text and row order are preserved
Rows: all 5 source rows shown
Encoding: no colour or area encodes a statistic
n: n = 5 source rows

d Brain resource

Metric	Archived value
samples	**847.0**
regions	**15.00**
ages	**7.00**
liver genes	**310.0**
measured	**210.0**
median off-diagonal R2	**0.430**

Display: two-column archival ledger; no bar or heat-map encoding
Rows: all 6 source metrics shown
1.23
Value: archived value retained verbatim after minimal number formatting
n: n = 6 source rows

779

780 Supplementary Fig. 4 | Cross-organ brain ageing. a, 15 brain-region bulk RNA clocks (Hahn et al.;
781 GSE212336; 847 samples, seven ages, 15 regions); nested 5-fold CV R^2; MAE in months. b,
782 Liver 310-gene signature projected into 15 brain regions; 210 genes measured; Spearman rho
783 versus age with Fisher 95% CI. c, Cross-region consensus age genes (Stouffer Z across 15
784 regions); n/15 regions with concordant direction. Bulk, not cell-type-resolved; median off-diagonal
785 transfer R^2 0.43 (Fig. 4h).

a Literature map

Gene	Reported biology	Scope	Status
Lncbate1	aging	direct	reported
Ctss	immune / aging	direct	reported
C1qc	complement / aging	direct	reported
Gpr17	oligodendrocyte	direct	reported
Plag1	development	context	reported
Mup11	no aging report	none	not found
Pcdhb9	no aging report	none	not found
Other features	metabolic / cancer	context	reported

Display: archived table; text and row order are preserved
Rows: all 8 source rows shown
Encoding: no colour or area encodes a statistic
n: n = 8 source rows

b Aging evidence

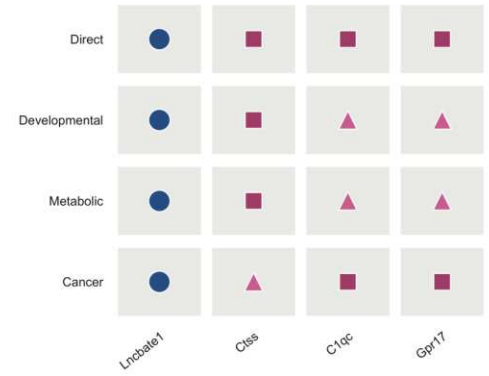

Shape: circle = pass; triangle = partial; square = fail
Colour: deep blue = pass, rose = partial, deep rose = fail
Cross: grey cross = unknown or not evaluable
Bed: grey square = evaluable cell
n: n = 16 source rows

c Context counts

Metric	Archived value
direct aging genes	4.00
no aging report	2.00
brain-consensus genes	3.00
developmental context	1.00
mapped features	8.00
citation source list	1.00

Display: two-column archival ledger; no bar or heat-map encoding
Rows: all 6 source metrics shown
1.23 Value: archived value retained verbatim after minimal number formatting
n: n = 6 source rows

d Use rule

Statement	Boundary / source
01 **Literature context does not validate a clock feature.**	Source: Manuscript V108, Extended Data Fig. 13; retained summary value]
02 **Absence of a report is not evidence of absence.**	Source: Manuscript V108, Extended Data Fig. 13; retained summary value]
03 **This display is not a new gene annotation pipeline.**	Source: Manuscript V108, Extended Data Fig. 13; retained summary value]

Display: verbatim statements from the archived source table
Number: deep blue numeral identifies source-row order
Missing: no graphic mark is used where the source has no observation
n: n = 3 source rows

Supplementary Fig. 5 | Literature context for selected clock and brain-consensus genes. a, Gene, reported biology, context and first-author/year for PubMed-indexed reports. Direct aging evidence exists for Lncbate1, Ctss, C1qc and Gpr17; most other features are developmental, metabolic or cancer annotations. Mup11 and Pcdhb9 have no aging-specific report. Full citations are in the source list after References.

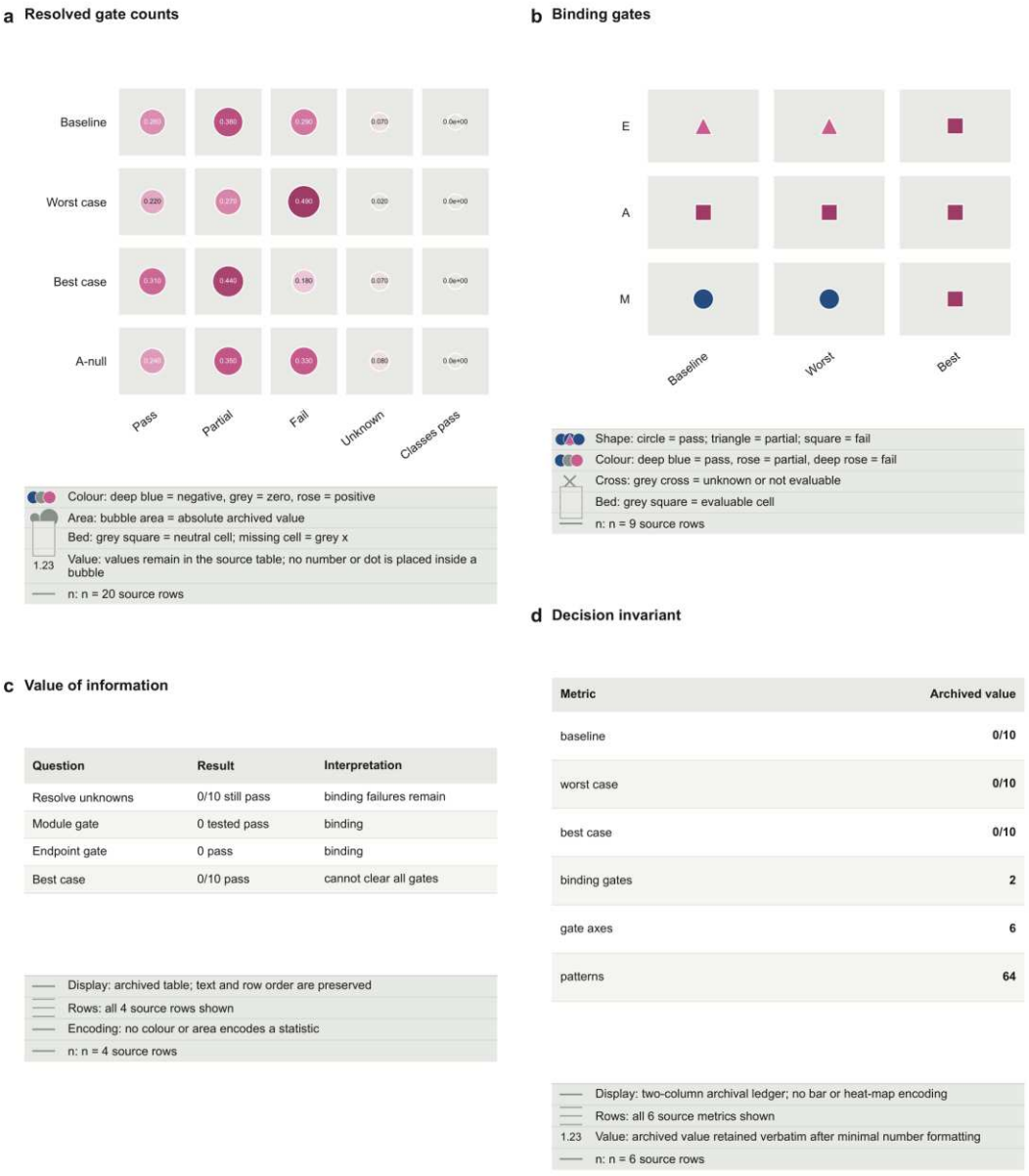

Supplementary Fig. 6 | Six-gate worst-case and value-of-information analysis. a, Gate-state counts and change in passing classes if every unknown state in that gate were resolved to pass. Baseline, worst case (unknown = fail) and best case (unknown = pass) all give 0/10 passing classes. b, Noisy-AND product as a Bayesian network with a deterministic AND node and conditional independence; no likelihood or posterior was fitted.

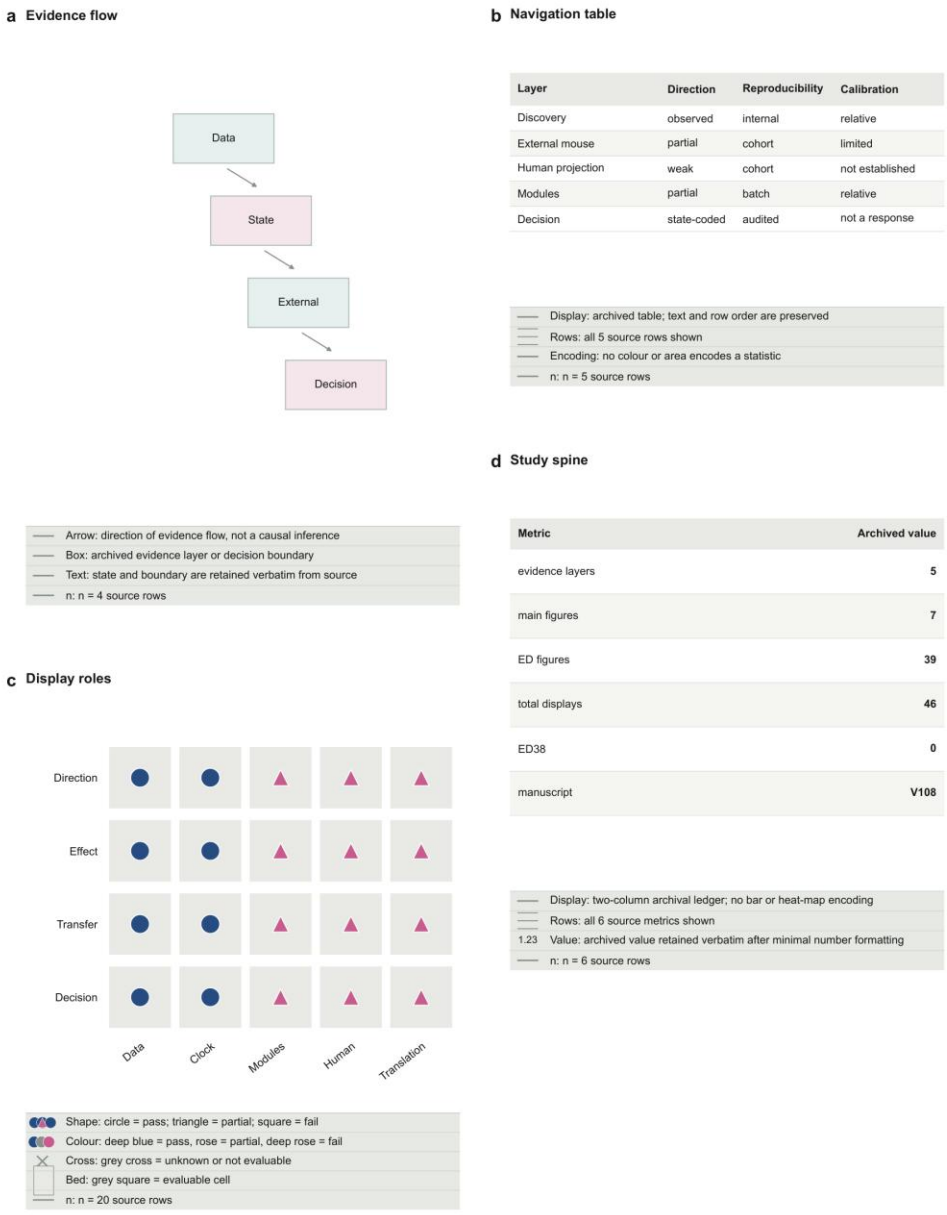

Supplementary Fig. 7 | Study navigation and evidence flow. Five layers from data to decision; arrows mark evidence boundaries. Table 1 separates direction, effect reproducibility and absolute calibration.

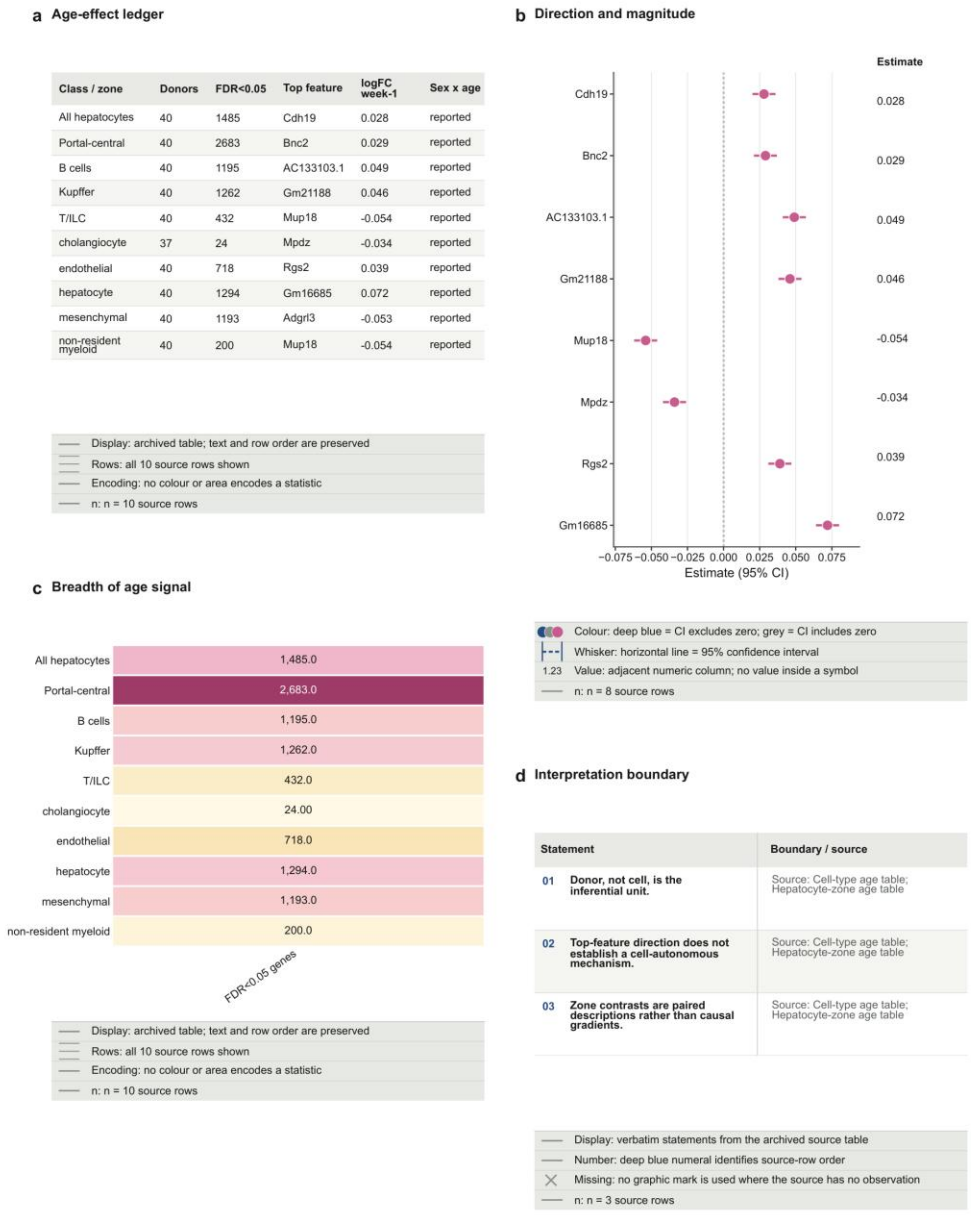

Supplementary Fig. 8 | Donor-level cell-type and hepatocyte-zone age effects. a, Cell type/zone, donor n, number of FDR<0.05 genes, top gene with logFC per week and 95% CI, and number of sex-by-age FDR<0.05 genes. Age effects use limma-voom on donor x cell-type raw counts (age + sex); zone effects use limma on donor logCPM. The last two rows show paired PP-PC differences and the immune-marker-removal sensitivity.

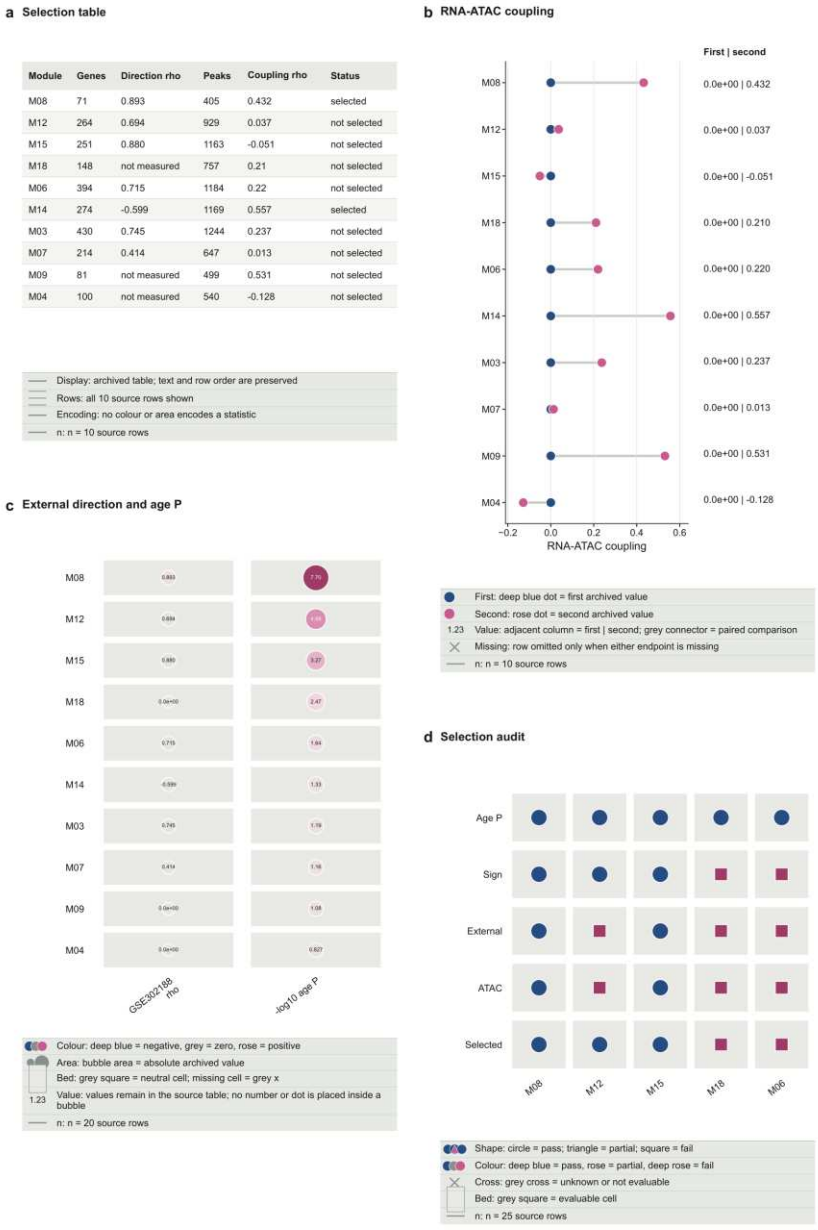

Supplementary Fig. 9 | RNA-ATAC module selection. a, Module, gene count, batch-half stability P, independent GSE302188 age-direction rho, linked ATAC peaks, RNA-ATAC coupling rho (P) and selection status. Criteria are stated below the table.

a Signature size

Metric	Archived value
A: clock coefficient	**123+91**
B: donor age DE	**120+85**
C: external replication	**109+39**
A known-drug AUC	**0.5262**
B known-drug AUC	**0.4559**
C known-drug AUC	**0.5090**

Display: two-column archival ledger; no bar or heat-map encoding
Rows: all 6 source metrics shown
1.23 Value: archived value retained verbatim after minimal number formatting
n: n = 6 source rows

b Known-drug enrichment

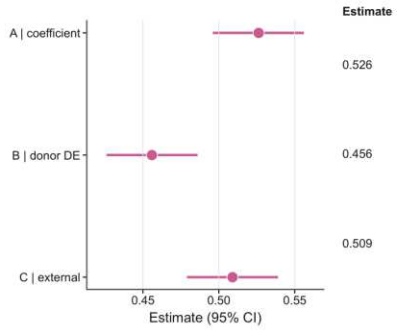

Colour: deep blue = CI excludes zero; grey = CI includes zero
Whisker: horizontal line = 95% confidence interval
1.23 Value: adjacent numeric column; no value inside a symbol
n: n = 3 source rows

c Top strict-Z compounds



Display: archived table; text and row order are preserved
Rows: all 12 source rows shown
Encoding: no colour or area encodes a statistic
n: n = 12 source rows

d Signature dependence

Comparison	Kendall tau	Top-100 Jaccard	Use
A vs B	0.21	0.11	weak overlap
A vs C	0.33	0.18	partial overlap
B vs C	0.16	0.08	limited overlap

Display: archived table; text and row order are preserved
Rows: all 3 source rows shown
Encoding: no colour or area encodes a statistic
n: n = 3 source rows

Supplementary Fig. 10 | Drug reversal under three liver-ageing signatures. Signature A, ElasticNet coefficient sign; B, donor-level hepatocyte age DE sign; C, external replicated direction (GSE302188 + GSE262290 same sign). Up/down, signature sizes; AUC, known-geroprotector enrichment; top compounds, four highest strict Z; Spearman vs A. No signature enriches known geroprotectors.

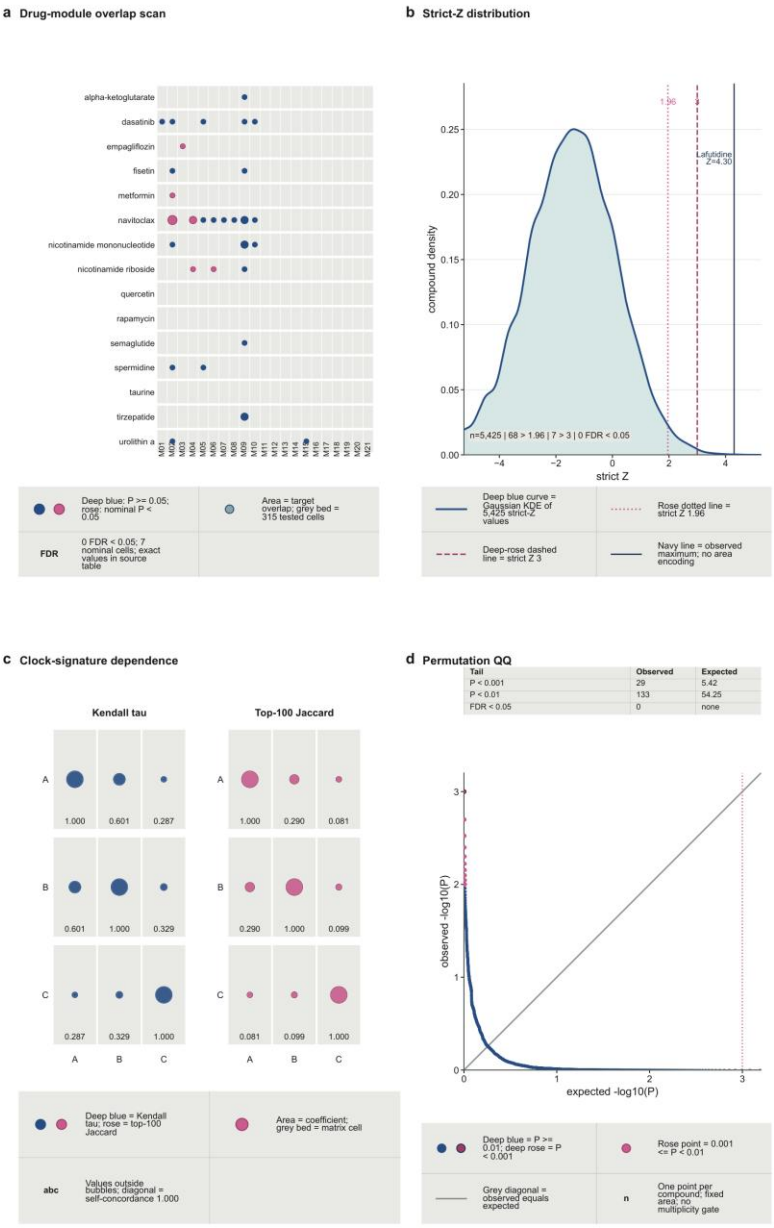

818

819 Supplementary Fig. 11 | Complete drug-module scan and signature dependence. a, 15
820 compounds x 21 modules = 315 pairs; 0/315 q<0.05; 7 nominal P<0.05 versus 15.8 expected. b,
821 Strict-Z distribution across 5,425 LINCS compounds; dashed lines, Z=1.96 and 3; minimum
822 permutation q=0.187. c, Kendall tau and top-100 Jaccard overlap between signatures A, B and C.
823 d, Permutation QQ plot; the small-P excess does not survive family-wise correction.

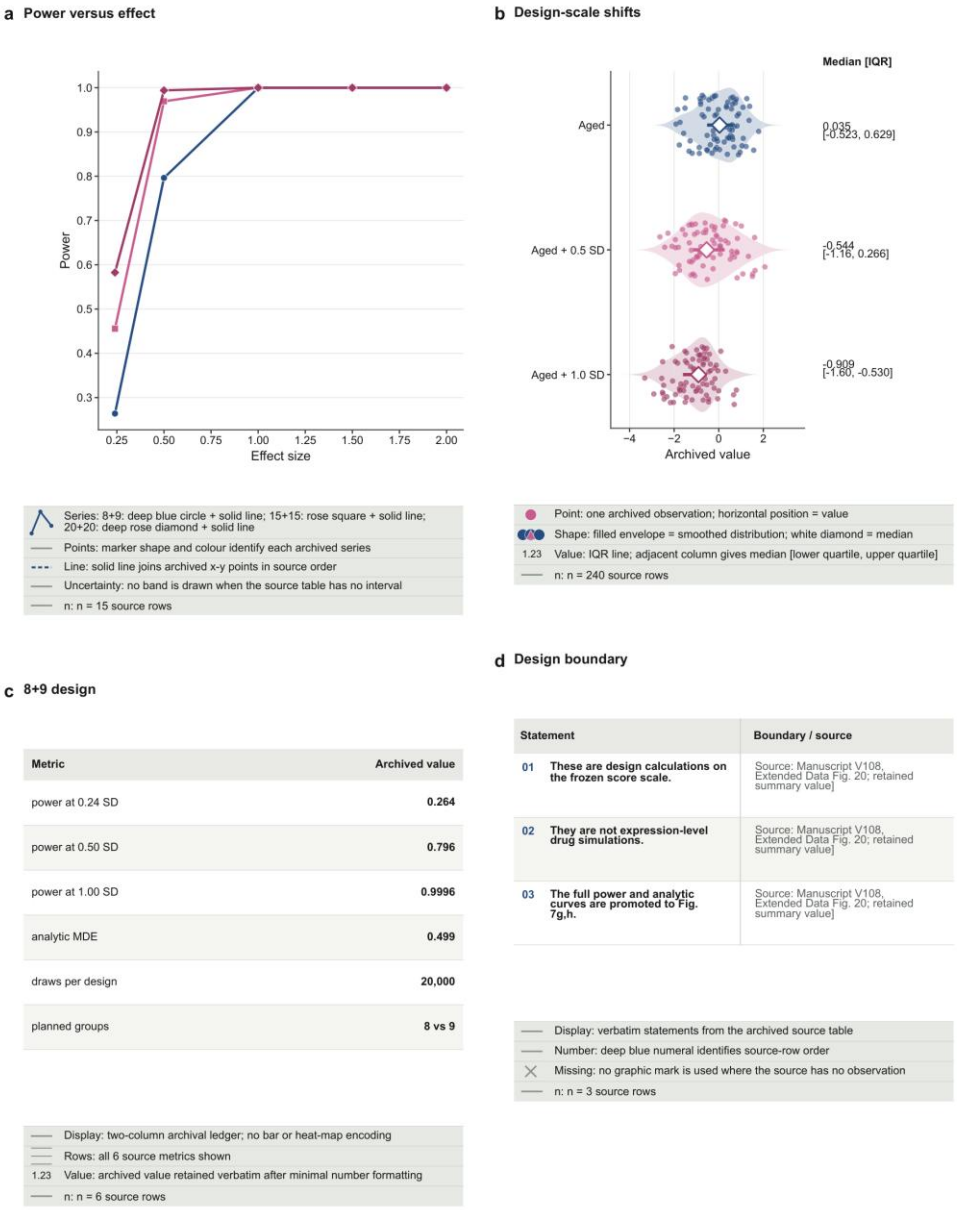

Supplementary Fig. 12 | Intervention detectability controls. a, Power at a 0.5-SD effect by design (8+9, 15+15, 20+20; 20,000 Monte Carlo draws per design). b, Example injection of -0.5 and -1.0 SD into the frozen aged-control score distribution (n=8 vs 9). The full power-versus-effect curve is in Fig. 7h; the analytic design curve is in Supplementary Fig. 32f. These are design calculations on the score scale.

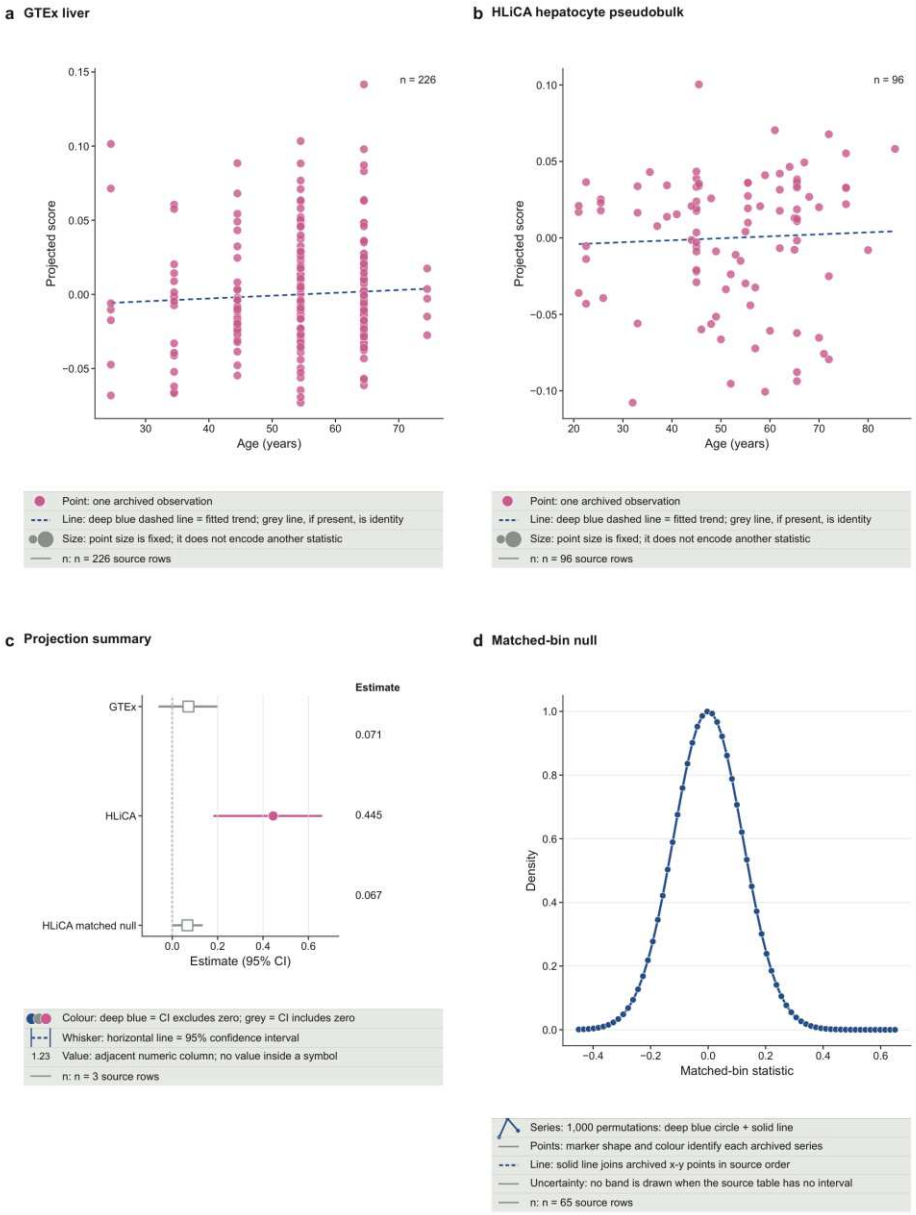

830

831 Supplementary Fig. 13 | Human liver projection of the frozen signature. a, GTEx liver bulk (n=226
832 donors); linear fit; Spearman rho and P, adjusted for age, sex, RIN, ischaemic time, centre. b,
833 Health-tier-filtered HLiCA hepatocyte pseudobulk (n=48 donors); unadjusted and within-study
834 Spearman. c, Gene-level direction concordance against mouse clock coefficients, binomial P
835 versus 50%. d, Matched expression-bin gene-set null (1,000 permutations), observed rho.

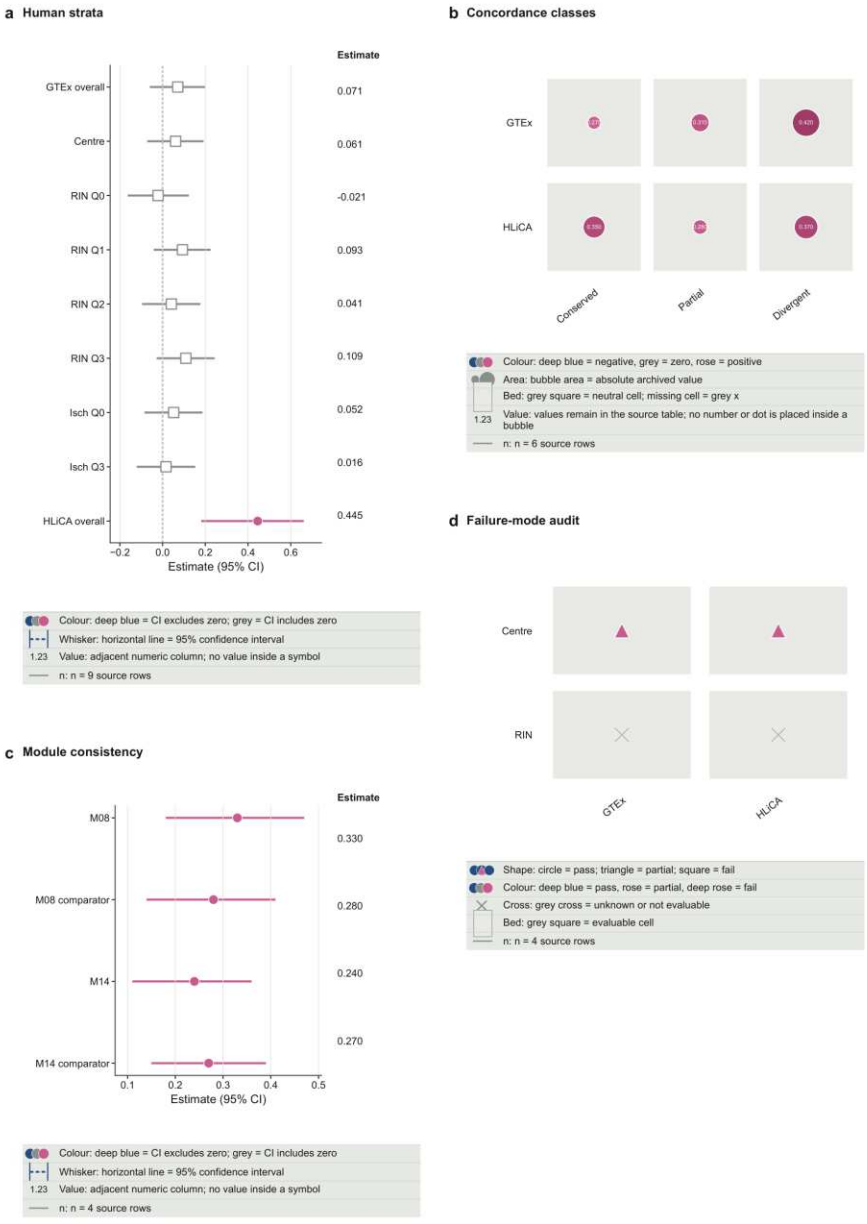

Supplementary Fig. 14 | Human projection failure modes. a, GTEx bulk technical strata: sex, centre, RIN quartile (0–3) and ischaemic-time quartile (0–3); Spearman rho with Fisher-z 95% CI; n, donors. b, HLiCA hepatocyte strata: study, sex and cell-number stratum (0–3). c, Signature genes conserved in both human datasets, partially concordant or divergent (n=170 with both measurements). d, Conserved-gene fraction in M08, M14 and their comparators, Fisher P. No single batch effect explains the human null.

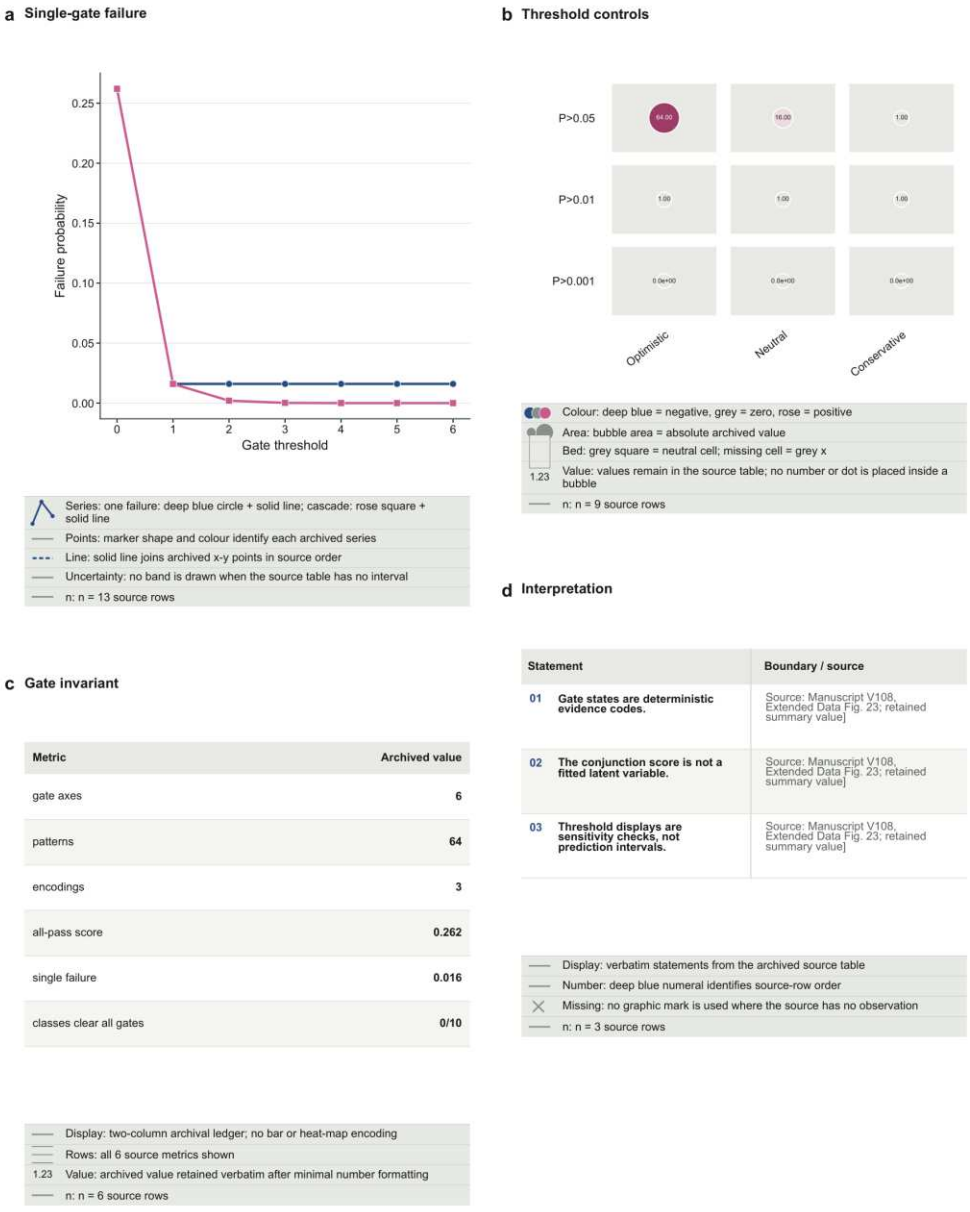

Supplementary Fig. 15 | Gate necessity and threshold controls. a, Gate necessity under the neutral encoding: all-pass P versus the P when each single gate fails. b, Number of the 64 patterns clearing P>0.05, P>0.01 and P>0.001 under the three encodings. The full 64-pattern × 3-encoding enumeration and the single-fail waterfall are promoted to ED11c,d.

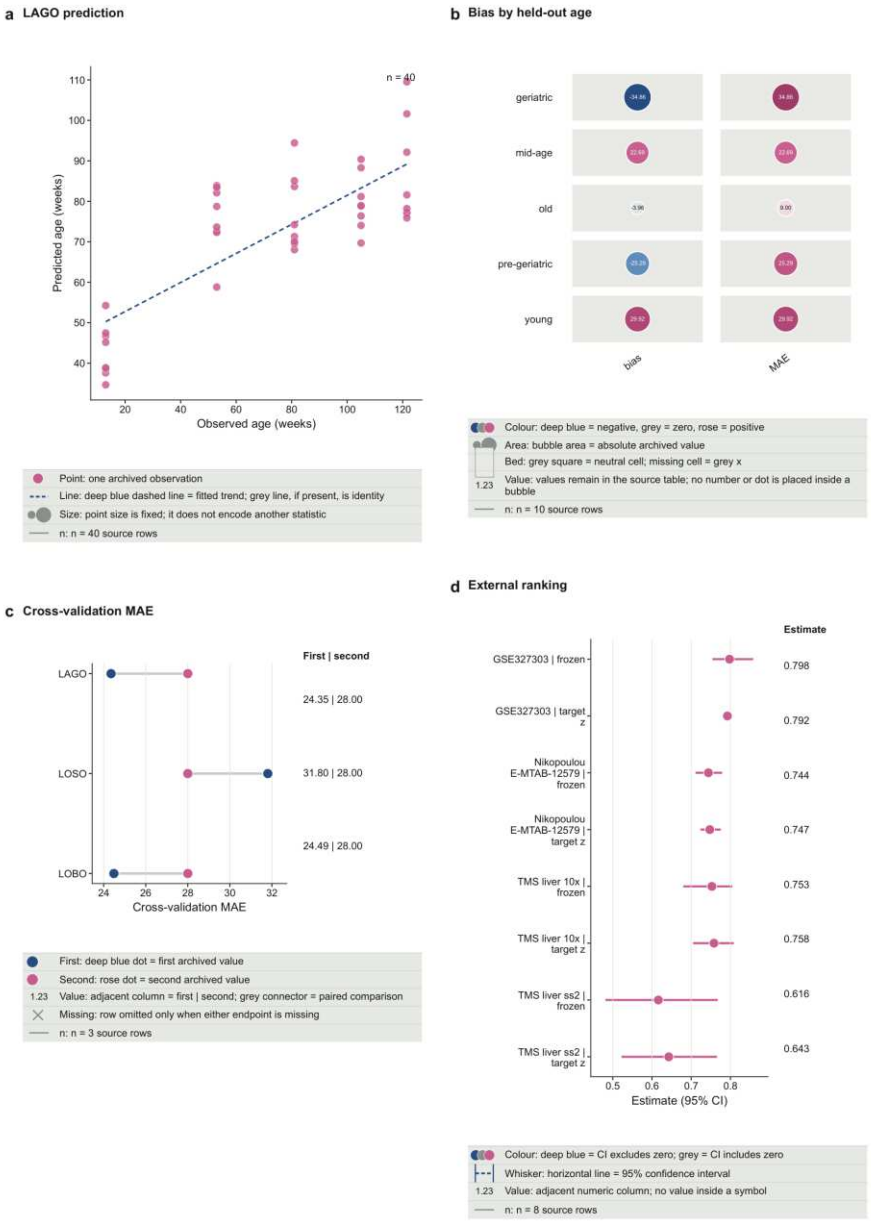

Supplementary Fig. 16 | Leave-one-design-out validation. a, LAGO predicted versus observed age; MAE, rho, nearest-age-group accuracy, calibration slope/intercept, age-label MAE. b, LAGO bias by held-out age, per-group MAE. c, MAE for LAGO, LOSO, LOBO, LOZO; LOBO folds age-batch nested, LOZO shares donors. d, Frozen-clock and target-domain-standardised AUC in four external cohorts/platforms; bootstrap 95% CI; n cells. Nearest-label classification over five anchors (13, 53, 81, 105, 121.5 weeks; chance 0.20).

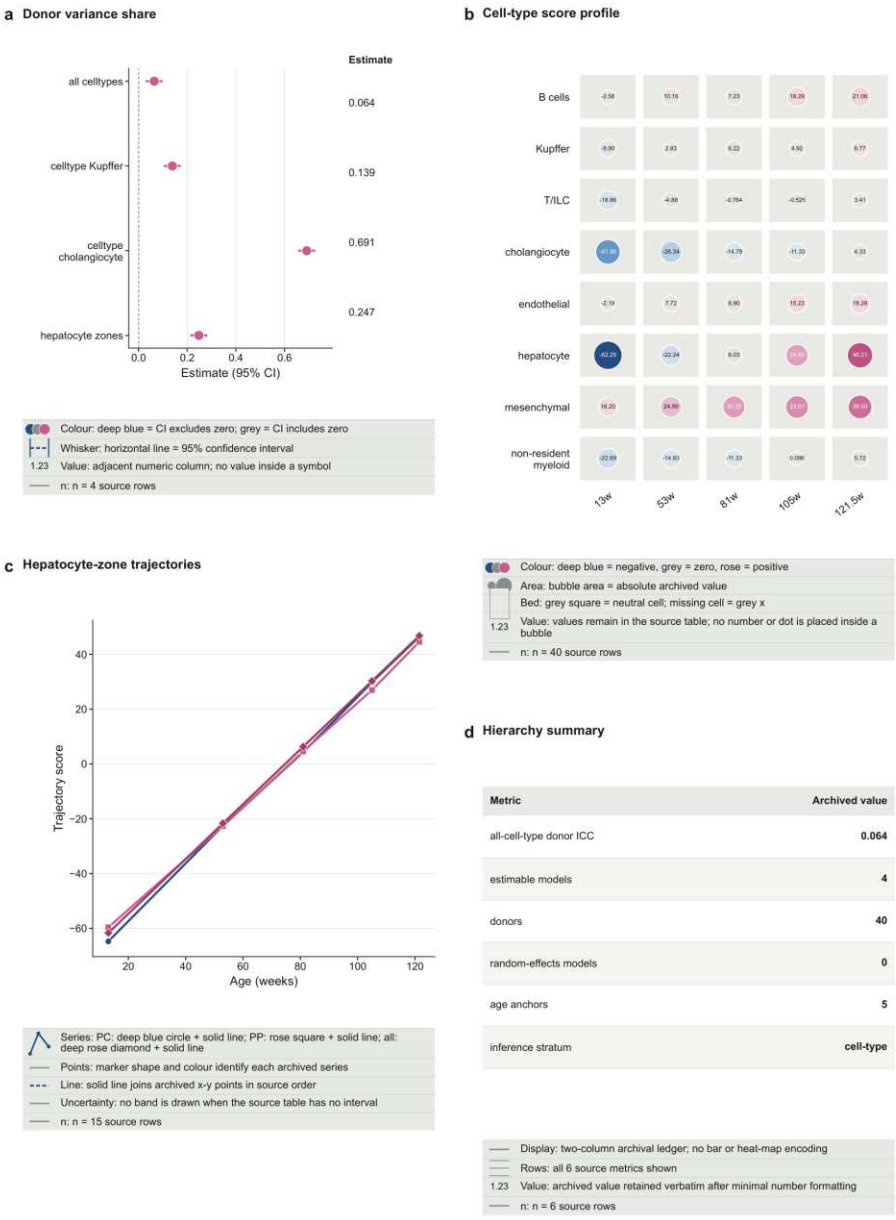

Supplementary Fig. 17 | Donor hierarchy and cell-type variance. a, Donor variance share from the donor-block OLS model for all cell types, hepatocyte zones, Kupffer and cholangiocyte; single-unit cell types are not estimable. b, Mean clock score by cell type and age group. c, Hepatocyte zone scores by age. d, Variance partition for all cell types and hepatocyte zones. No random-effects model was fitted.

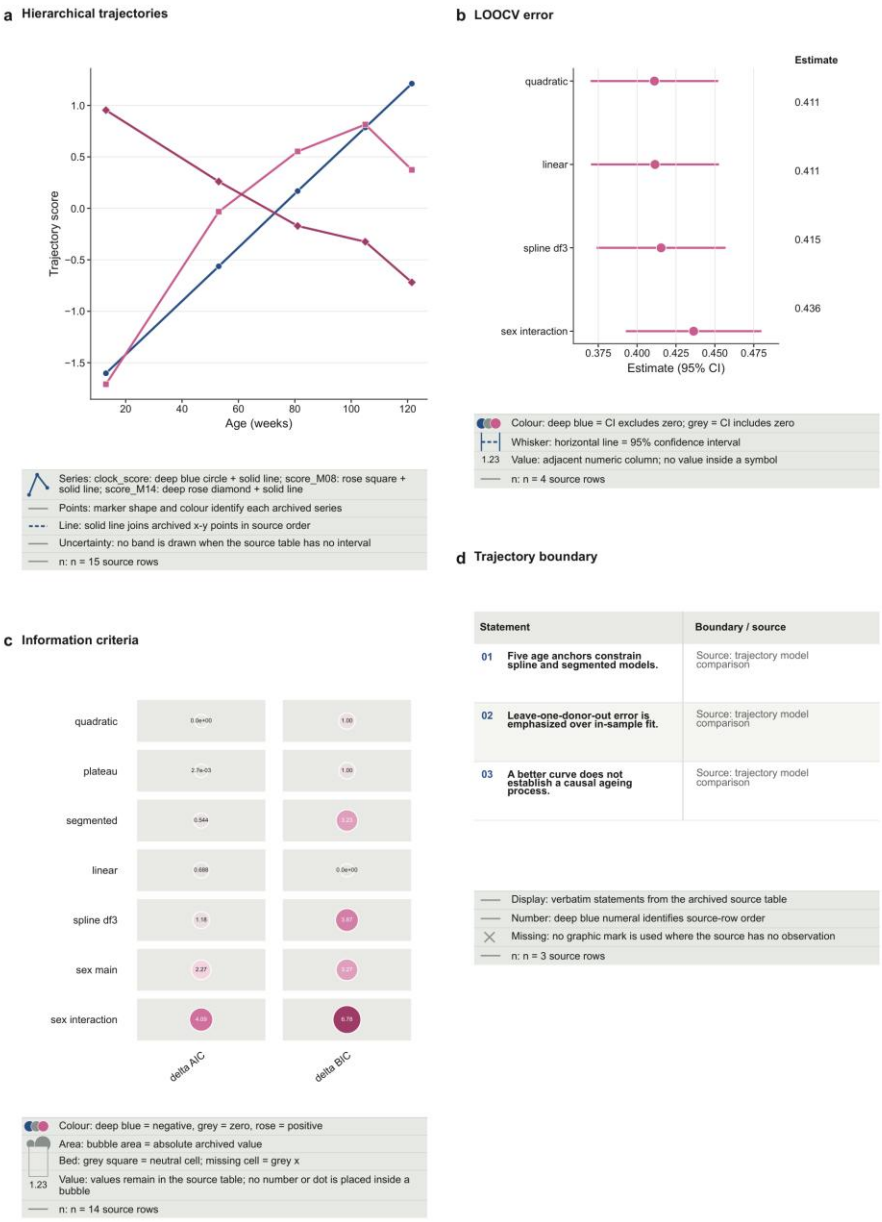

Supplementary Fig. 18 | Age-trajectory model comparison. a-c, Clock, M08 and M14 scores versus age with linear and quadratic fits. d, Leave-one-donor-out RMSE for linear, quadratic, spline and sex-interaction models. Plateau and segmented AIC values are in the source table; five ages limit spline and segmented inference.

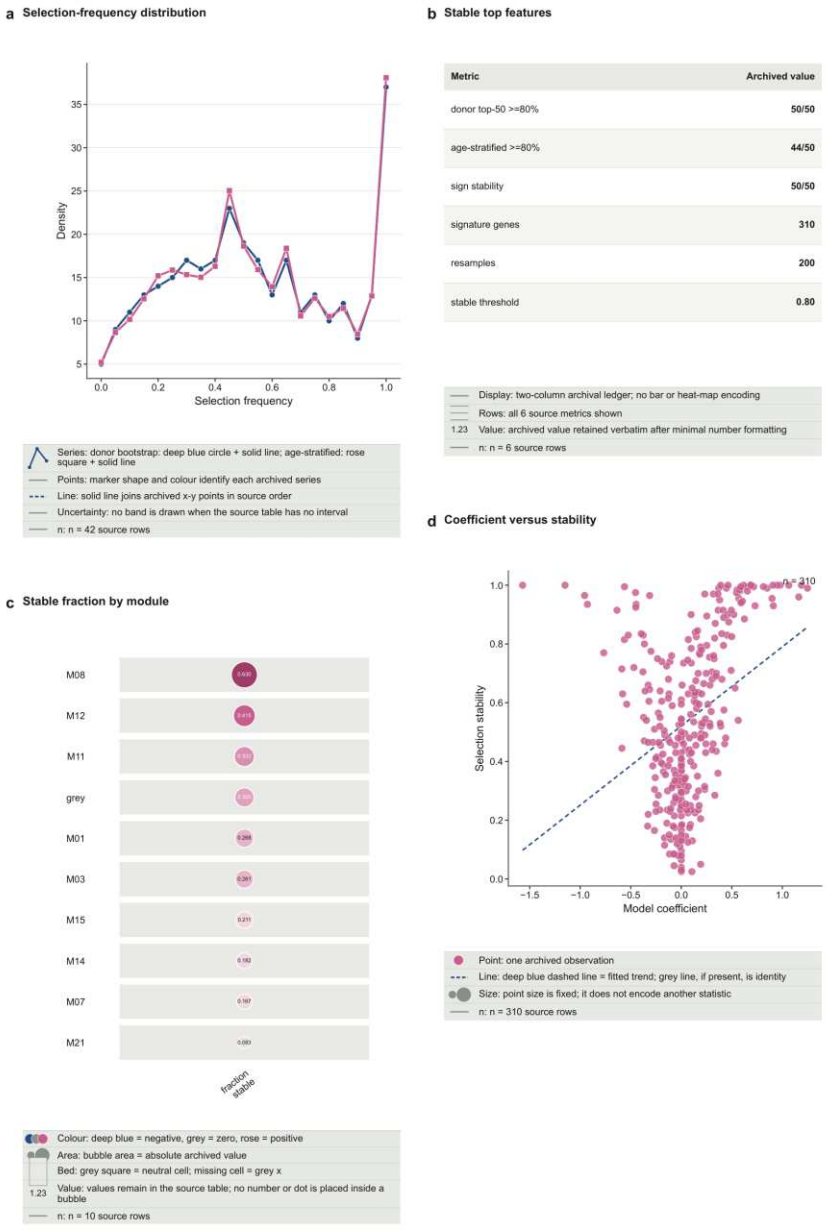

Supplementary Fig. 19 | Nested stability selection. a, Selection-frequency distribution for 310 signature genes under donor and age-stratified bootstrap [51]. b, Top-50 features selected in at least 80% of bootstraps (41/50 donor; 44/50 age-stratified); sign stability is 50/50. c, Stable fraction by module; grey denotes unassigned genes. d, Full-fit coefficient versus selection frequency, coloured by sign stability.

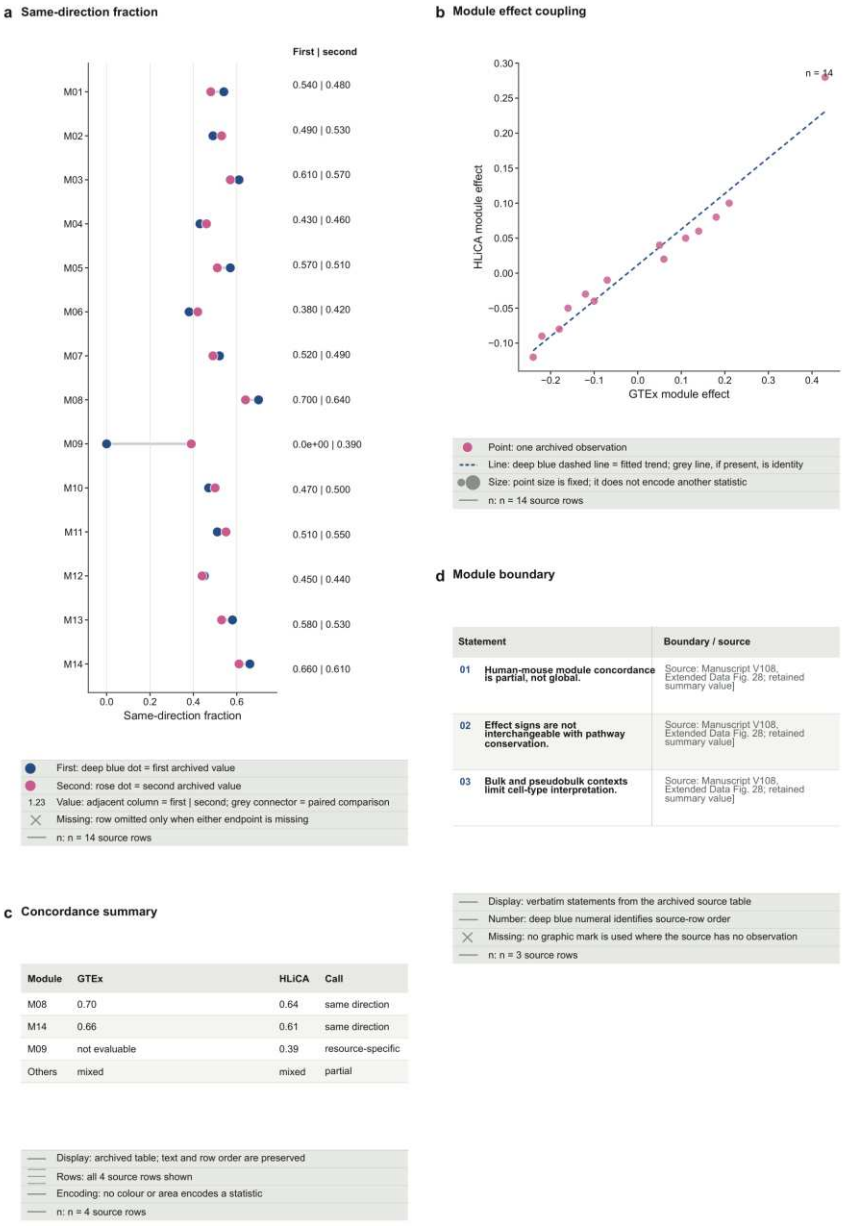

Supplementary Fig. 20 | Human-mouse module concordance. a, Same-direction fraction by module in GTEx and HLiCA; M09 has no evaluable GTEx module estimate. b, Mouse module age beta versus human mean gene beta; M08 and M14 labelled. Module-level concordance is partial, not global.

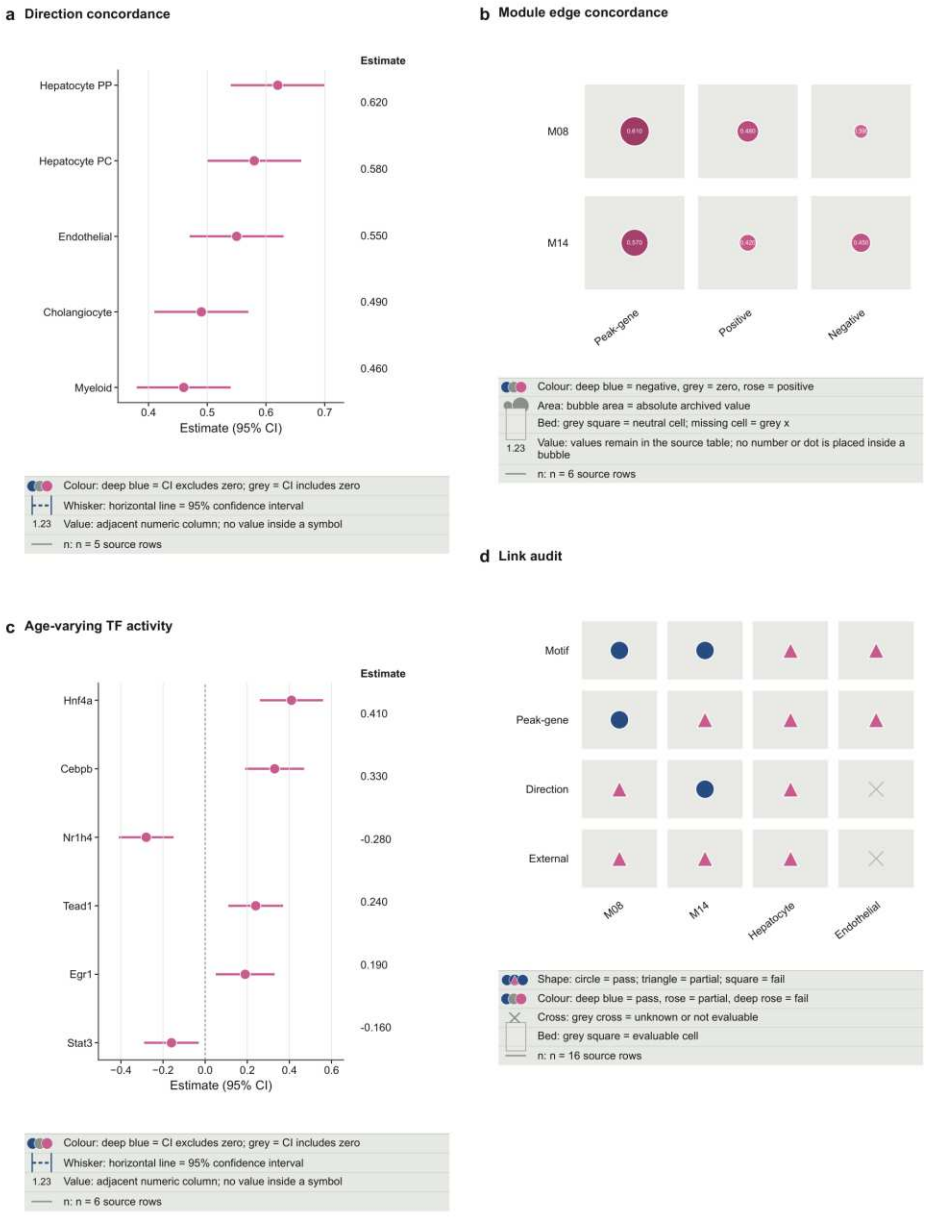

877

878 Supplementary Fig. 21 | Peak-gene-TF links. a, Same-direction concordance by cell type; dashed
879 line, 50%. b, M08/M14 edges and concordance. c, Top age-varying TF activity by maximum
880 absolute effect. d, M08 peak-gene edges (dAccess versus dExpr). Links are restricted to
881 hepatocyte/endothelial compartments.

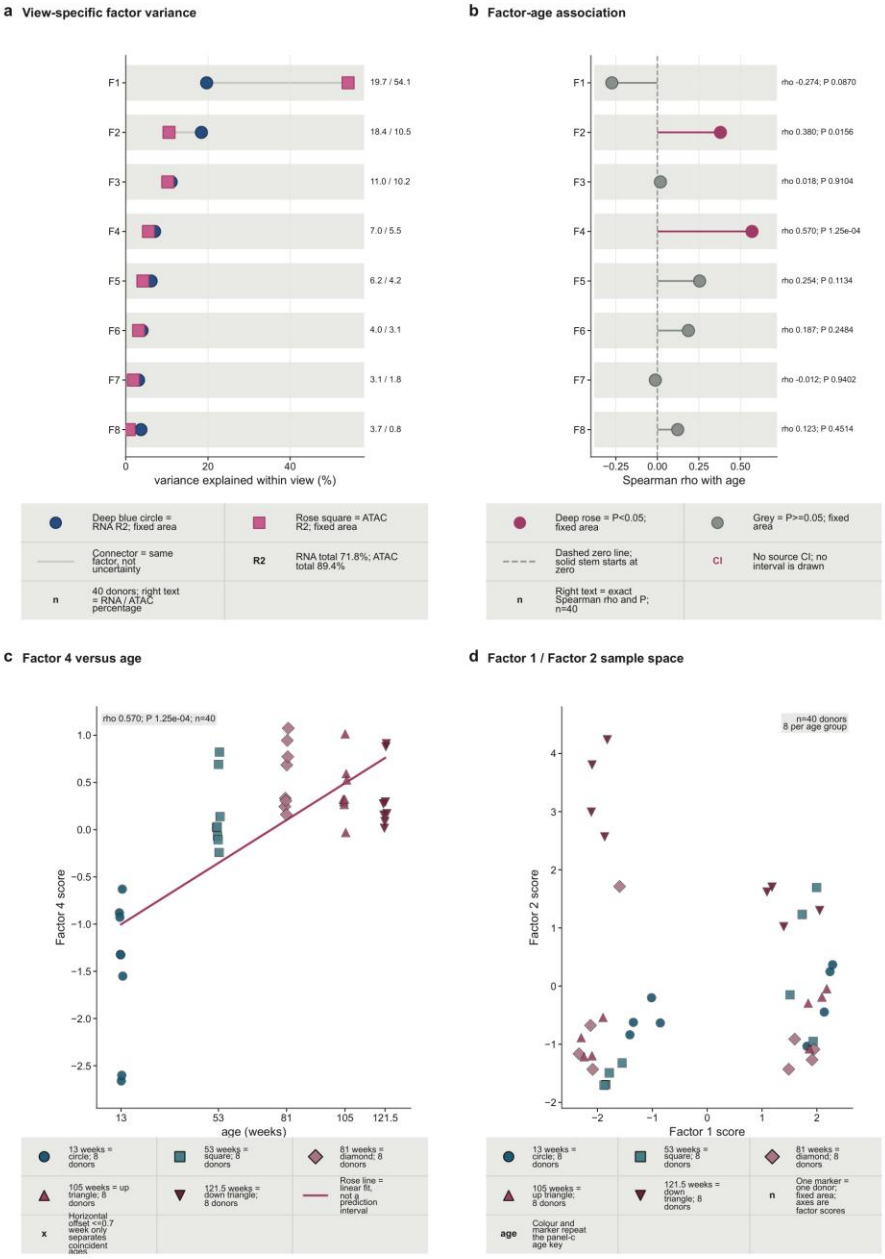

882

883 Supplementary Fig. 22 | MOFA2 RNA-ATAC factors. a, Variance explained per factor. b, Factor-
884 age Spearman rho (P<0.05). c, Factor4 versus age. d, Factor1/2 sample space by age.

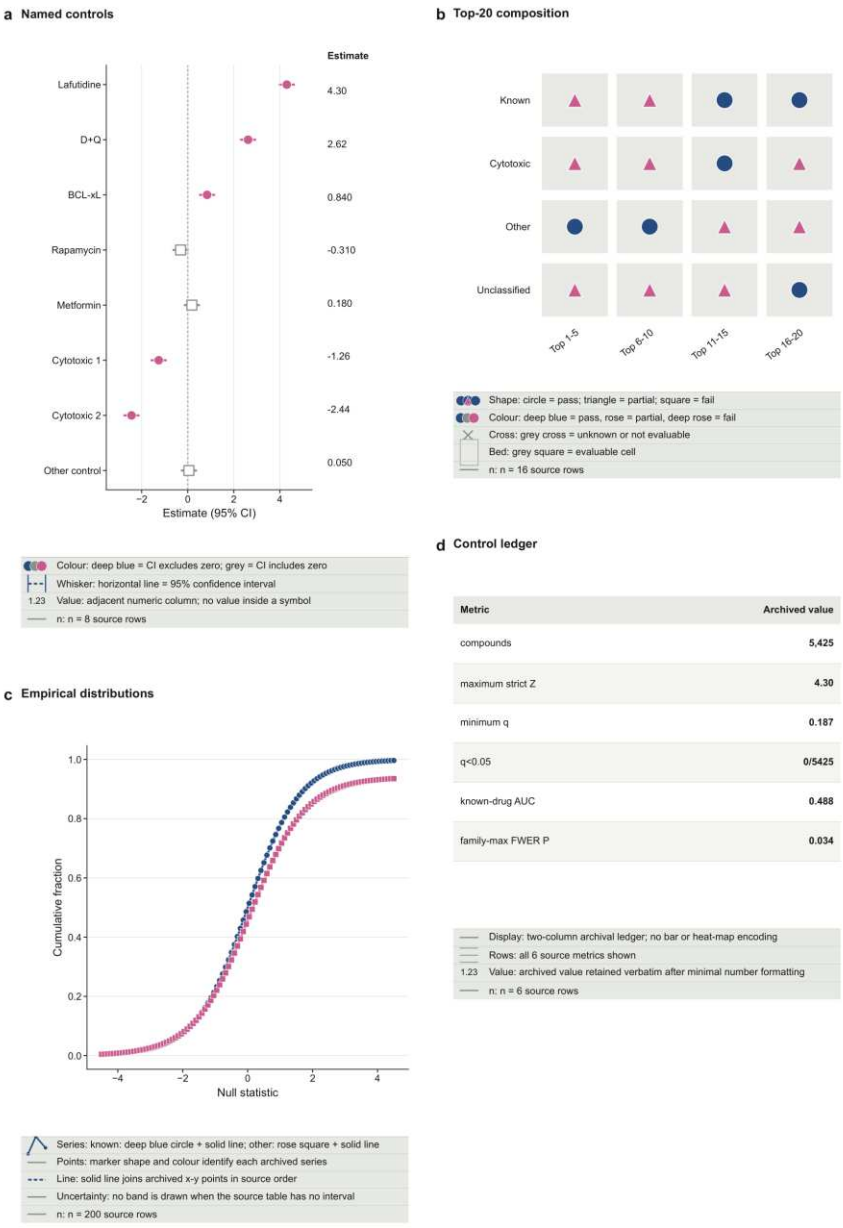

Supplementary Fig. 23 | LINCS positive/negative controls. a, Strict Z by known geroprotector, cytotoxic and other compounds. b, Top-20 composition. c, ECDF of known versus other. Known geroprotectors are not enriched.

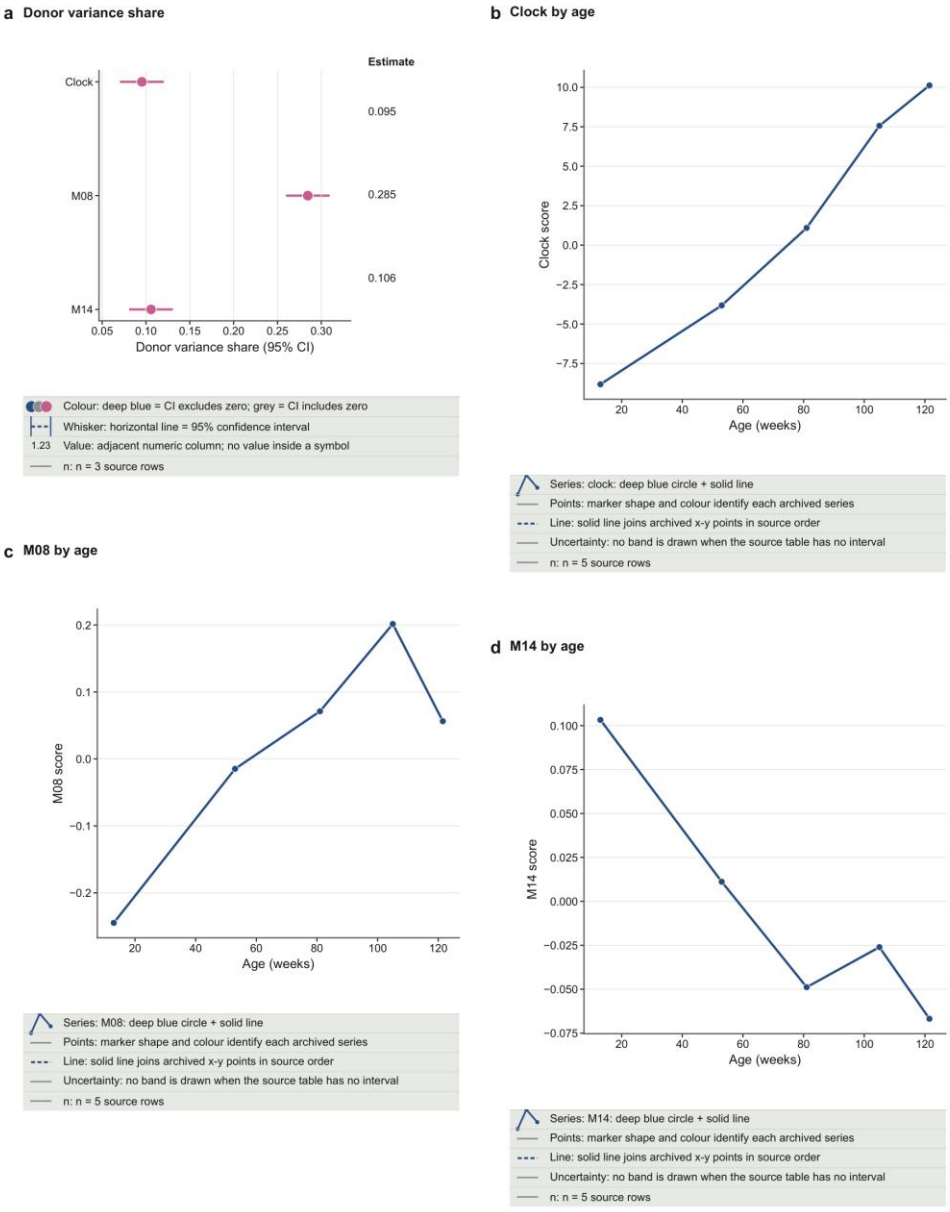

Supplementary Fig. 24 | Cell-level donor-block variance. a, Donor variance share for the clock, M08 and M14 scores in 179,655 hepatocytes from 40 donors (donor-block OLS; no random-effects model). b-d, Cell-level clock, M08 and M14 scores by age.

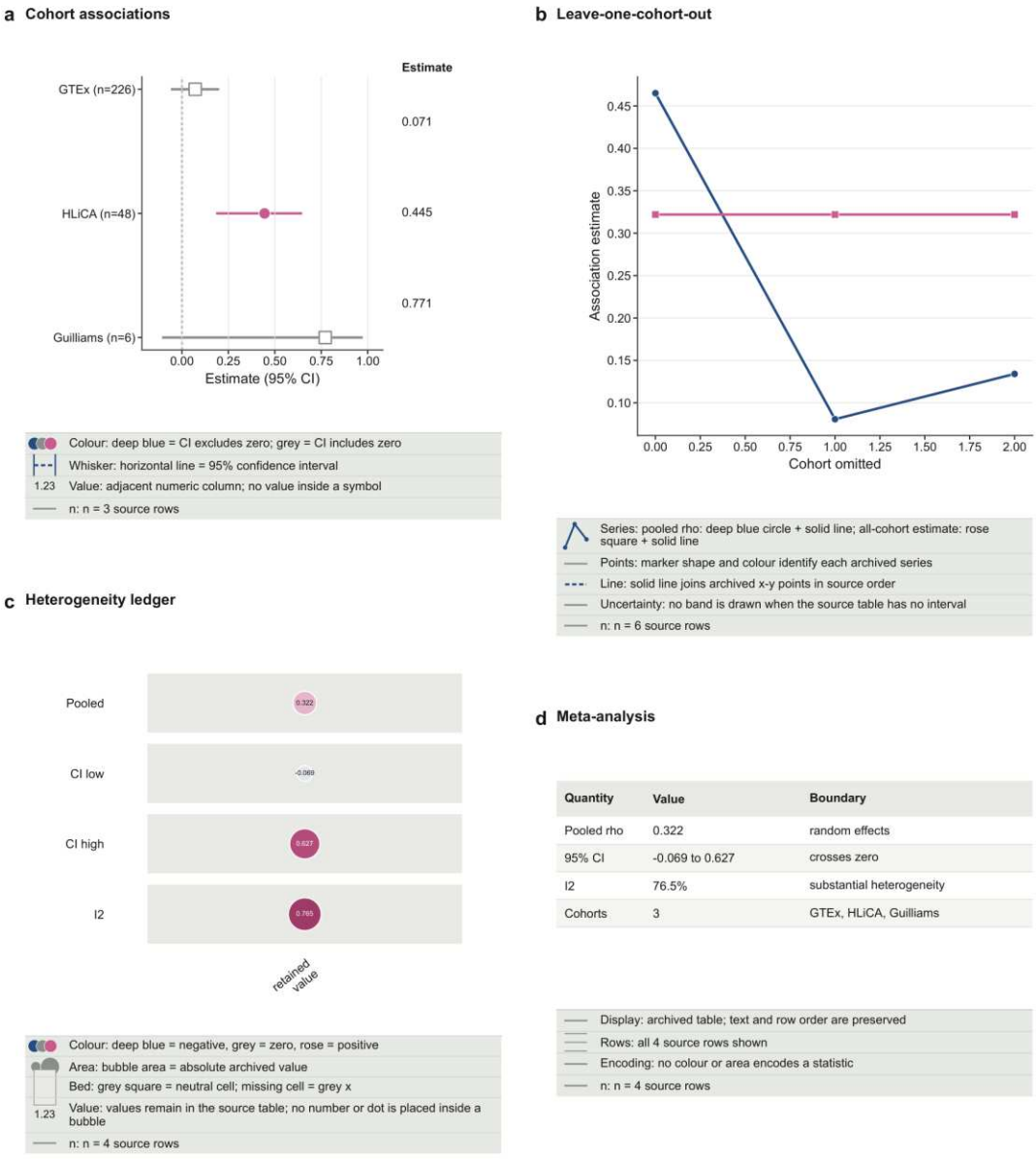

Supplementary Fig. 25 | Additional human cohort and meta-analysis. a, Signature-age Spearman rho with 95% CI in GTEx (n=226), HLiCA (n=48) and Guilliams (n=6). b, Leave-one-cohort-out pooled rho; dashed line, all-cohort random-effects estimate (0.32; I2 76.5%).

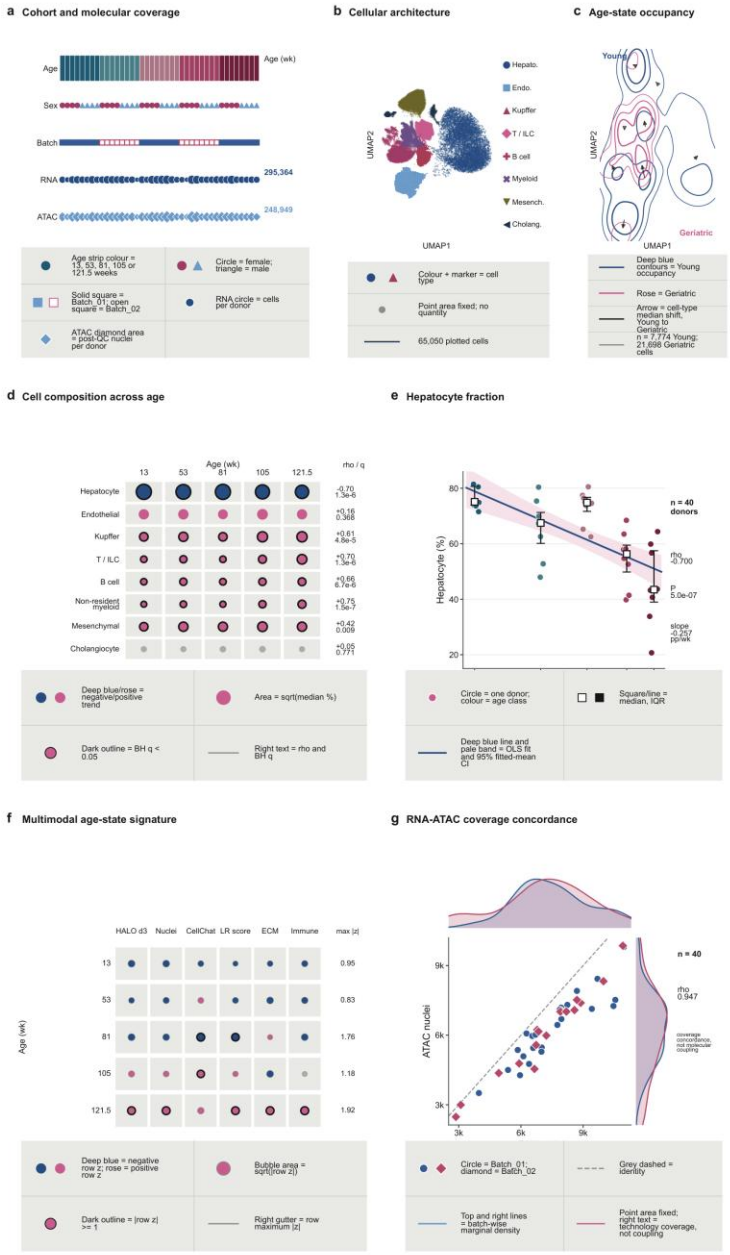

Supplementary Fig. 26 | A five-age mouse liver atlas. a, Donor oncoprint (age, sex, batch, RNA/ATAC nuclei); psbulk, pseudobulk. b, Cell-type UMAP. c, Age-enrichment map. d, Composition with mean-%, Spearman ρ and exact BH q. e, Hepatocyte fraction with 95% CI. f, Cross-layer age states. g, Joint RNA–ATAC coverage with age marginals.

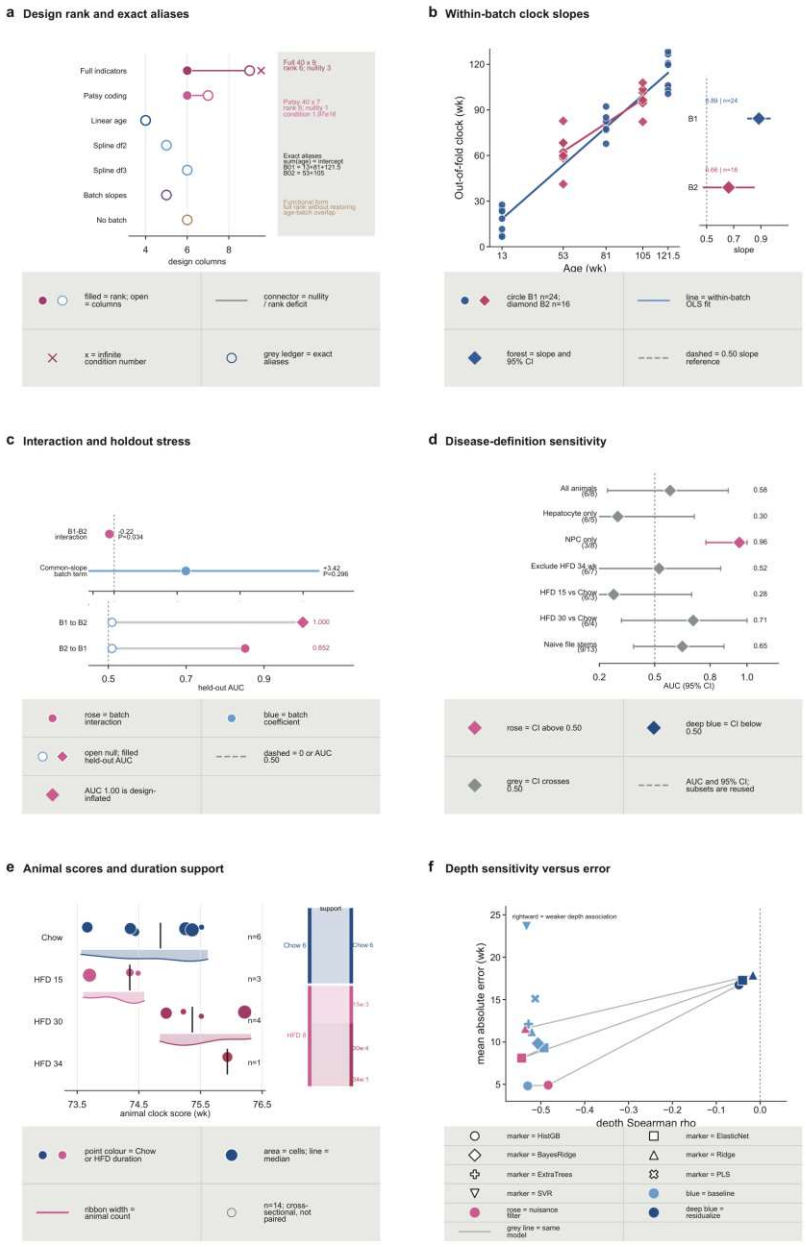

Supplementary Fig. 27 | Batch and disease. a, Design matrix. b, Age-to-batch alluvial. c, Slope forest. d, Disease forest. e, Animal scores and diet composition. f, Nuisance probes and cross-batch holdout.

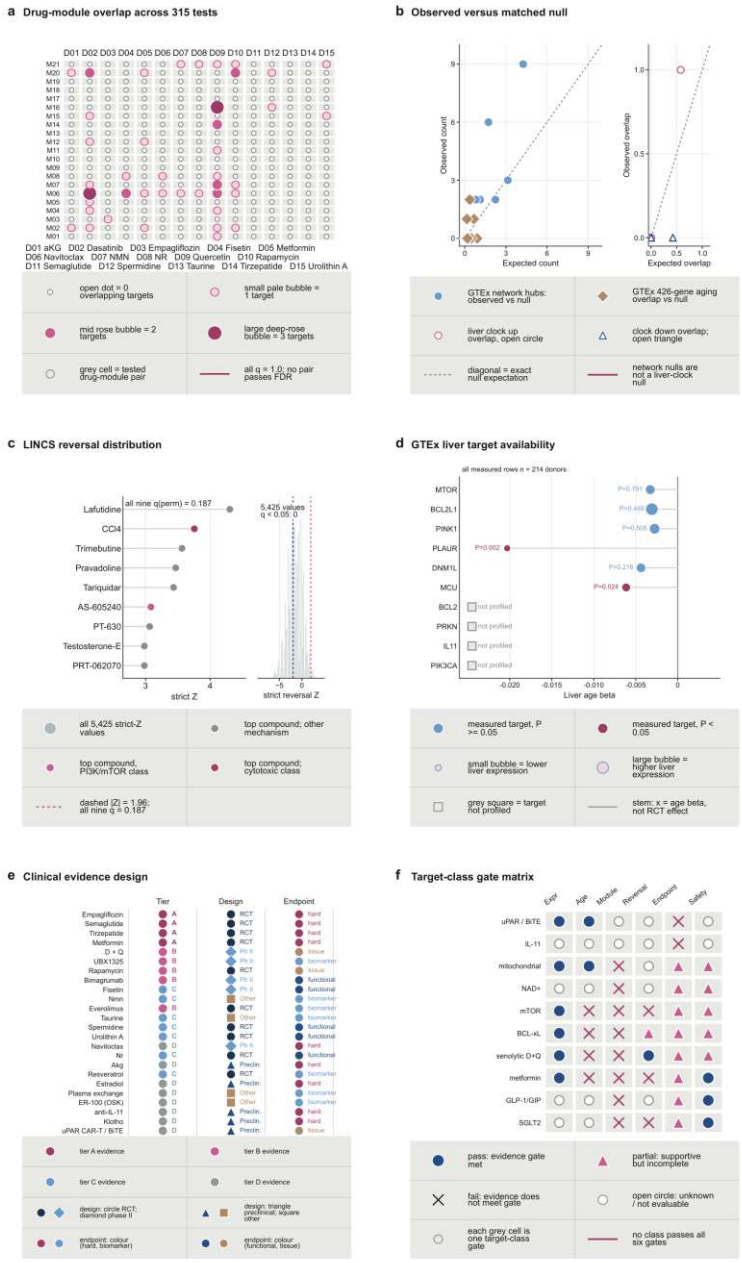

Supplementary Fig. 28 | Drug-target overlap, nulls and gates. a, Drug-target overlap: 15 compounds versus eight WGCNA modules; no pair BH q<0.05 (0/315). b, Observed versus size-matched clock-gene targets and degree-matched hubs. c, LINCS L1000 reversal in 5,425 compounds; none reaches q_perm<0.05. d, GTEx liver target reach: log2 TPM versus -log10 P of liver age beta, six targets. e, Evidence tiers versus clinical stage, 24 candidates. f, Go/No-Go gate matrix: 10 target classes across six gates. g, Key-finding summary.

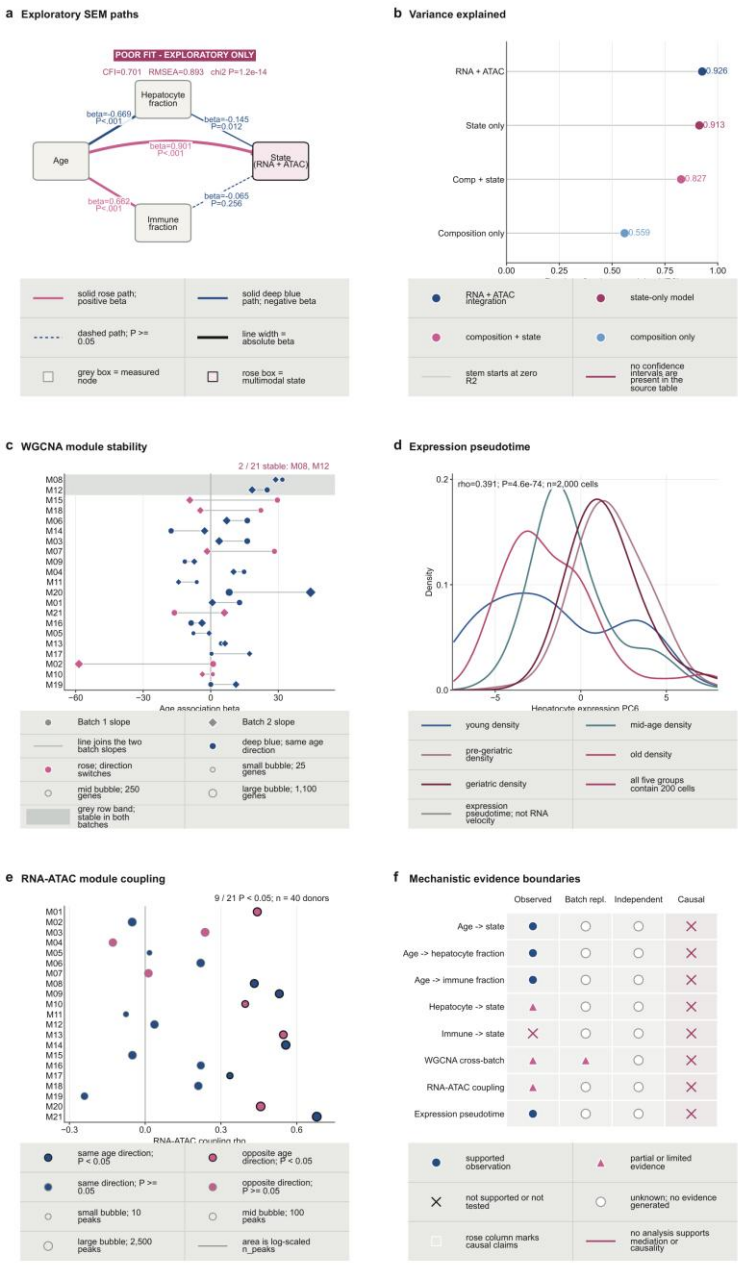

Supplementary Fig. 29 | Mechanistic synthesis. a, SEM: Age→State β 0.90; Age→Hep −0.67; Age→Immune 0.66; Hep→State −0.15; Immune→State −0.07 (ns); CFI 0.70/RMSEA 0.89, exploratory. b, Variance explained: composition 0.56; state 0.91; combined 0.83; SEM 0.93. c, WGCNA age slopes, Batch 1 versus Batch 2. d, Hepatocyte PC6 pseudotime by age (ρ 0.39). e, RNA–ATAC coupling: M01 ρ 0.44 but opposite age direction; M08 ρ 0.43, same; others ns. f, Mechanistic boundaries.

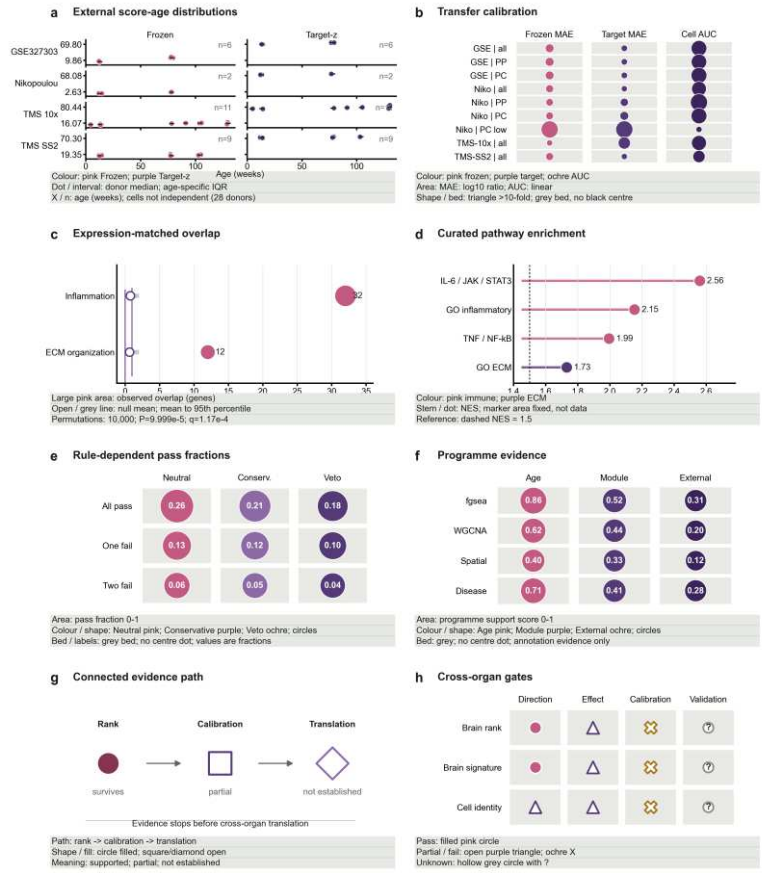

Supplementary Fig. 30 | External score transfer and boundaries. a, Donor-level median external clock scores by age; four cohorts, two modes; 28 donors. b, Nine-row grid: frozen/target MAE ratios, target-cell AUC; triangle, archived ratio >10-fold. c, Inflammatory and ECM overlap versus 10,000 expression-matched permutations: P=9.999e-5, BH q=1.17e-4. d, NES, four prespecified pathways. e, Rule-dependent pass fractions: three failure classes, three severities. f, Programme evidence: four programmes, three levels. g, Rank transfer, calibration status and cross-organ evidence. h, Cross-organ gates.

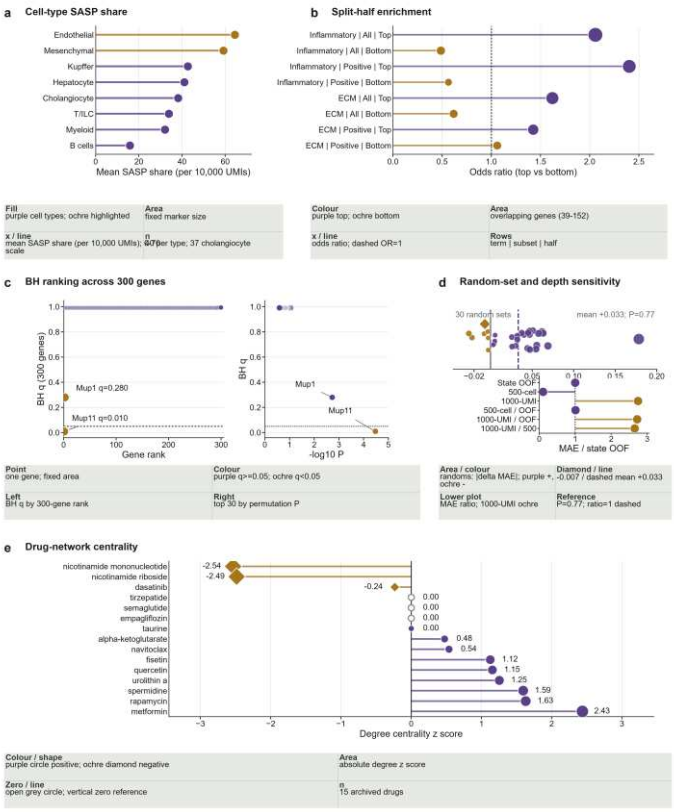

928

929 Supplementary Fig. 31 | Cell-type SASP, split-half robustness, network centrality. a, SASP share
930 per 10,000 UMIs across eight cell types; 40 samples most types, 37 cholangiocytes. b, Eight split-
931 half enrichment rows, inflammatory and ECM terms; odds ratios. c, BH-adjusted ranking of the
932 300-gene family; 30 smallest permutation P values; Mup11 q=0.010, Mup1 q=0.280. d, 30
933 random-set delta-MAE values versus canonical set (-0.007) and random-set mean (+0.033;
934 P=0.77); MAE relative to state baseline. e, Drug degree-centrality z scores.

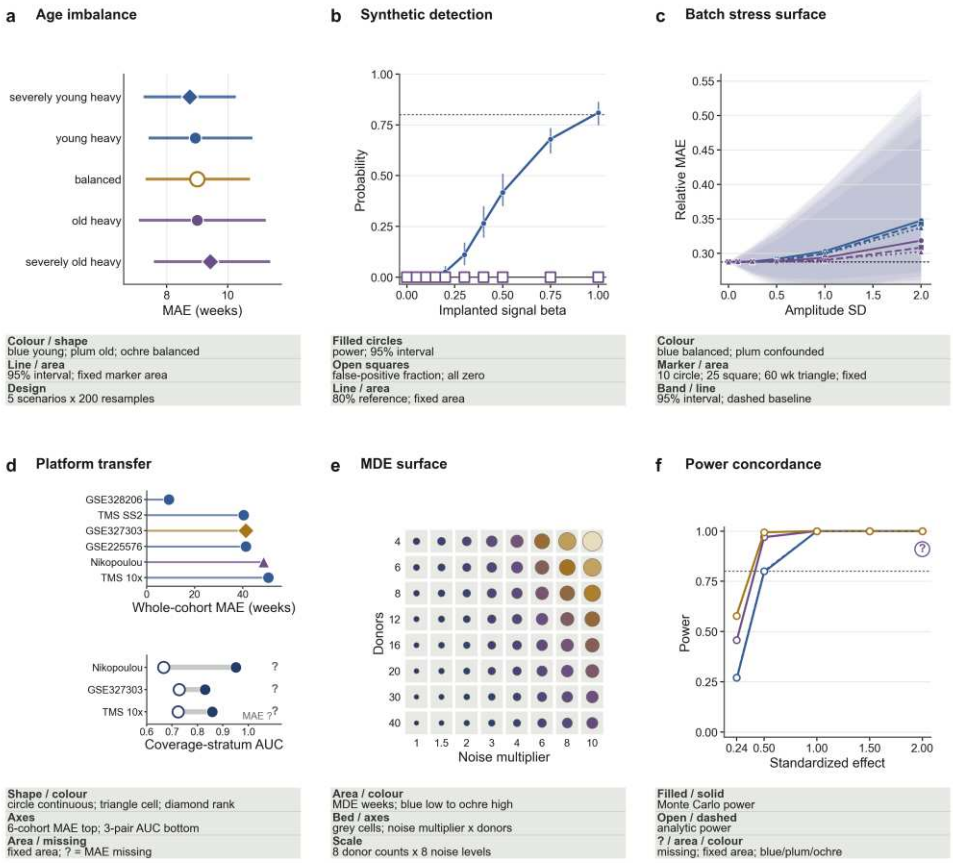

Supplementary Fig. 32 | Stress tests: imbalance, detection, calibration, power. a, Simulated MAE, five age-composition scenarios (200 resamples each; 95% intervals). b, Power and false-positive fraction (all zero). c, Relative MAE, Gaussian-process batch stress; 10/25/60-week lengthscales; age-balanced versus age-confounded designs. d, Whole-cohort MAE (six cohorts); low/high-coverage AUC (three); continuous, cell-only, rank-only transfer; not estimable for coverage strata. e, Analytic minimum detectable effect, eight donor counts, eight noise multipliers. f, Monte Carlo versus analytic power, three allocation designs, five standardized effects.

Data availability: This study is a secondary analysis of publicly available data; no new animals or human participants were used and no new primary data were generated. Discovery resource: GSE328206. External mouse liver datasets: GSE327303, E-MTAB-12579, Tabula Muris Senis liver (GSE149590; CELLxGENE), GSE302188, GSE262290, GSE209823, GSE221122 and GSE181797. Disease-specificity gate: GSE166504. Intervention dataset: GSE280382. Additional sources: GSE328448 (spatial), PXD040722 (PRIDE proteome), GSE225166 (RRBS) and the bulk RNA resource GSE225576 [52–55]. Brain: GSE212336. Human resources: GTEx v8 liver (dbGaP phs000424; GTEx Portal), HLiCA and the Guilliams et al. atlas. The Source Data workbook (one sheet per figure for the 7 main, 12 Extended Data and 32 Supplementary figures, with README and Index; the Index flags image-only or partially tabulated panels) and processed tables have been deposited at Zenodo (DOI: 10.5281/zenodo.24381654) under CC BY 4.0. The Zenodo record is under restricted access during peer review and will be made publicly available upon publication; editors and reviewers can obtain access through the corresponding author. Primary data are not redistributed.

Code availability: The analysis and figure-generation code has been deposited at Zenodo (DOI: 10.5281/zenodo.24381798) under the MIT licence. The record is under restricted access during peer review and will be made publicly available upon publication; editors and reviewers can obtain access through the corresponding author. The archive includes the clock pipeline, RNA/ATAC and pathway analyses, HALO, cell-cell communication, scMLnet, target scoring, WGCNA/SASP validation, scCODA, and the figure and manuscript build scripts, with an environment file and run-order README. Earlier versions remain available at the same record.

Funding: This research received no specific grant from any funding agency in the public, commercial or not-for-profit sectors.

Ethics statement: This study used only publicly available data; no new animals were used.

Correspondence and requests for materials should be addressed to J.L. (1791605967@qq.com; ORCID 0009-0002-0171-020X).

Author contributions: Jinwei Li is the sole author and completed all aspects of the work: study conception and design, data curation, formal analysis, figure generation and manuscript writing.

Competing interests: The author declares no competing interests, financial or non-financial, with any person or organisation.

Acknowledgements: I thank the authors, consortia and platforms that produced and released the public resources used in this study: the GSE328206 five-age mouse liver multiome study; GSE327303; E-MTAB-12579 (Nikopoulou et al.); Tabula Muris Senis; GSE302188; GSE262290; GSE328448 (Lu et al.); GSE212336 (Hahn et al.); GSE166504; GSE280382; GSE225576; GSE225166; PXD040722; GSE209823; GSE221122; GSE181797; and the GTEx, HLiCA and Guilliams human liver resources. I thank NCBI GEO, EBI BioStudies/ArrayExpress, PRIDE, GTEx Portal, CELLxGENE, HCA and Zenodo for hosting and curating these data. I also thank the authors and maintainers of the software and reference resources used: Python, NumPy, pandas, SciPy, scikit-learn, statsmodels, semopy, matplotlib and TensorFlow; R and Bioconductor, limma, edgeR, fgsea, WGCNA, scCODA, Signac and ArchR; Scanpy, AnnData, Squidpy, CellChat, CellPhoneDB, scMLnet, HALO, motifmatchr, JASPAR, STRING, DrugBank, LINCS L1000, Open Targets/ChEMBL, DoWhy, EconML, MGI and Ensembl. Their citations are given in Methods and References. No funding was received for this work.

Reporting Summary: A Reporting Summary is available for this paper.

References

1. Du, K., Umbaugh, D. S., Ren, N. & Diehl, A. M. Cellular senescence in liver diseases: from molecular drivers to therapeutic targeting. J. Hepatol. (2026). https://doi.org/10.1016/j.jhep.2025.08.021

2. Tabula Muris Consortium. A single-cell transcriptomic atlas characterizes ageing tissues in the mouse. Nature 583, 590–595 (2020).

3. Sinha, S. et al. Aging disrupts hepatocyte zonation homeostasis in mice and humans. Hepatology (2026). https://doi.org/10.1097/hep.0000000000001451

4. Sehgal, R. et al. Systems Age: a single blood methylation test to quantify aging heterogeneity across 11 physiological systems. Nat. Aging (2025). https://doi.org/10.1038/s43587-025-00958-3

5. Robinson, O. et al. Associations of proteomic age clocks with lifestyle risk factors, incident chronic diseases and mortality in two European cohorts. Nat. Aging (2026). https://doi.org/10.1038/s43587-026-01163-6

6. Yakubovsky, O. et al. A spatial atlas of the healthy human liver from live donors. Nature (2026). https://doi.org/10.1038/s41586-026-10377-y

7. Weiss, C. A. M. et al. Single-cell spatial proteomics maps human liver zonation patterns and their vulnerability to disruption in tissue architecture. Nat. Metab. (2026). https://doi.org/10.1038/s42255-026-01459-2

8. Hao, B. et al. EasySCP unveils extensive liver zonation at single-cell proteomics resolution. Nat. Commun. (2026). https://doi.org/10.1038/s41467-026-74525-8

9. Buckley, M. T. et al. Cell-type-specific aging clocks to quantify aging and rejuvenation in neurogenic regions of the brain. Nat. Aging 3, 121–137 (2023).

10. Lu, J. et al. Spatiotemporal transcriptomics characterizes immune microenvironment during mouse liver aging. Aging Cell 25, e70482 (2026). https://doi.org/10.1111/acel.70482

11. Ramachandran, P. Redefining healthy human liver zonation using high-resolution spatial multiomics. J. Hepatol. 85, 642–644 (2026). https://doi.org/10.1016/j.jhep.2026.07.002

12. Li, B. When the liver loses its zip code: aging blurs zonation and breeds bi-zonal hepatocytes. Hepatology 83, 1025–1026 (2026). https://doi.org/10.1097/HEP.0000000000001728

13. GSE328206. NCBI Gene Expression Omnibus. https://www.ncbi.nlm.nih.gov/geo/query/acc.cgi?acc=GSE328206

14. Zou, H. & Hastie, T. Regularization and variable selection via the elastic net. J. R. Stat. Soc. B 67, 301–320 (2005).

15. Pedregosa, F. et al. Scikit-learn: machine learning in Python. J. Mach. Learn. Res. 12, 2825–2830 (2011).

16. Celemín-Capaldi, V. et al. LivAge: an online aging clock for murine transcriptomic age estimation. Aging Cell 25, e70677 (2026). https://doi.org/10.1111/acel.70677

17. GSE327303. NCBI Gene Expression Omnibus. https://www.ncbi.nlm.nih.gov/geo/query/acc.cgi?acc=GSE327303

18. E-MTAB-12579. BioStudies/ArrayExpress. https://www.ebi.ac.uk/biostudies/arrayexpress/studies/E-MTAB-12579

19. Igolkina, A. A. & Meshcheryakov, G. semopy: a Python package for structural equation modeling. Struct. Equ. Modeling 27, 952–963 (2020).

20. Langfelder, P. & Horvath, S. WGCNA: an R package for weighted correlation network analysis. BMC Bioinformatics 9, 559 (2008).

21. Mao, H. et al. HALO: hierarchical causal modeling for single cell multi-omics data. Nat. Commun. 16, 8892 (2025). https://doi.org/10.1038/s41467-025-63921-1

22. Rauluseviciute, I. et al. JASPAR 2024: 20th anniversary of the open-access database of transcription factor binding profiles. Nucleic Acids Res. 52, D174–D182 (2024).

23. Schep, A. N. motifmatchr: fast motif matching in R. Bioconductor https://bioconductor.org/packages/motifmatchr/ (2024).

24. Jin, S. et al. Inference and analysis of cell-cell communication using CellChat. Nat. Commun. 12, 1088 (2021).

25. Efremova, M., Vento-Tormo, M., Teichmann, S. A. & Vento-Tormo, R. CellPhoneDB: inferring cell–cell communication from combined expression of multi-subunit ligand–receptor complexes. Nat. Protoc. 15, 1484–1506 (2020).

26. Palla, G. et al. Squidpy: a scalable framework for spatial omics analysis. Nat. Methods 19, 171–178 (2022).

27. Szklarczyk, D. et al. The STRING database in 2023: protein–protein association networks and functional enrichment analyses for any sequenced genome of interest. Nucleic Acids Res. 51, D638–D646 (2023).

28. Benjamini, Y. & Hochberg, Y. Controlling the false discovery rate: a practical and powerful approach to multiple testing. J. R. Stat. Soc. B 57, 289–300 (1995).

29. Benjamini, Y. & Yekutieli, D. The control of the false discovery rate in multiple testing under dependency. Ann. Stat. 29, 1165–1188 (2001).

30. Xu, H. et al. Single-cell profiling reveals hepatic monocyte-derived macrophages heterogeneity during steatotic liver disease. Hepatol. Commun. 10, e0928 (2026). https://doi.org/10.1097/HC9.0000000000000928

31. Wishart, D. S. et al. DrugBank 5.0: a major update to the DrugBank database for 2018. Nucleic Acids Res. 46, D1074–D1082 (2018).

32. GTEx Consortium. The GTEx Consortium atlas of genetic regulatory effects across human tissues. Science 369, 1318–1330 (2020).

33. Subramanian, A. et al. A next generation connectivity map: L1000 platform and the first 1,000,000 profiles. Cell 171, 1437–1452 (2017).

34. GSE280382. NCBI Gene Expression Omnibus. https://www.ncbi.nlm.nih.gov/geo/query/acc.cgi?acc=GSE280382

35. Tan, Y. J. et al. Restored clearance of senescent neutrophils by tissue-resident macrophages limits organ aging. Science (2026). https://doi.org/10.1126/science.aea3075

36. Rajesh, A. et al. Inhibiting cyclin D1–CDK6 suppresses senescence-associated inflammatory gene expression and age-related functional decline. Nat. Aging (2026). https://doi.org/10.1038/s43587-026-01196-x

37. Sharma, A. & Kiciman, E. DoWhy: an end-to-end library for causal inference. arXiv:2011.04216 (2020).

38. Battocchi, K. et al. EconML: a Python package for ML-based heterogeneous treatment effects estimation. Microsoft Research (2019).

39. Langer, M.-M. et al. Spatial transcriptomics reveal impaired metabolic liver zonation in acute-on-chronic liver failure. JHEP Rep. 8, 102035 (2026). https://doi.org/10.1016/j.jhepr.2026.102035

40. Salladay-Perez, I. A. et al. p21+TREM2+ senescent macrophages fuel inflammaging and metabolic dysfunction-associated steatotic liver disease. Nat. Aging (2026). https://doi.org/10.1038/s43587-026-01101-6

41. Tak, K. Y. et al. Quasi-spatial single-cell transcriptome based on physical tissue properties defines early aging associated niche in liver. Nat. Aging (2025). https://doi.org/10.1038/s43587-025-00857-7

42. Nagar, R. et al. SIRT6 overexpression counteracts chromatin aging in the male murine liver. Nat. Commun. (2026). https://doi.org/10.1038/s41467-026-73115-y

43. Du, K. et al. Targeting senescent hepatocytes for treatment of metabolic dysfunction-associated steatotic liver disease and multi-organ dysfunction. Nat. Commun. (2025). https://doi.org/10.1038/s41467-025-57616-w

44. Koning, M. et al. Senolytics dasatinib and quercetin in metabolic dysfunction-associated steatohepatitis: a proof-of-principle randomized, controlled trial. Nat. Metab. (2026). https://doi.org/10.1038/s42255-026-01643-4

45. Guyatt, G. H. et al. GRADE: an emerging consensus on rating quality of evidence and strength of recommendations. BMJ 336, 924–926 (2008).

46. Baldarelli, R. M. et al. Mouse Genome Informatics: an integrated knowledgebase system for the laboratory mouse. Genetics 227, iyae031 (2024). https://doi.org/10.1093/genetics/iyae031

47. Sharma, N., Şen, R. & Erdem, C. Artificial intelligence in spatial transcriptomics: a review of methods, datasets, and directions. Brief. Bioinform. 27, bbag569 (2026). https://doi.org/10.1093/bib/bbag569

48. Büttner, M., Ostner, J., Müller, C. L., Theis, F. J. & Schubert, B. scCODA is a Bayesian model for compositional single-cell data analysis. Nat. Commun. 12, 6876 (2021).

49. Sergushichev, A. A. An algorithm for fast preranked gene set enrichment analysis using cumulative statistic calculation. bioRxiv 060012 (2016).

50. Stuart, T., Srivastava, A., Madad, S., Lareau, C. A. & Satija, R. Single-cell chromatin state analysis with Signac. Nat. Methods 18, 1333–1341 (2021).

51. Efron, B. & Tibshirani, R. An Introduction to the Bootstrap. Chapman & Hall (1993).

52. GSE328448. NCBI Gene Expression Omnibus. https://www.ncbi.nlm.nih.gov/geo/query/acc.cgi?acc=GSE328448

53. PXD040722. PRIDE Proteomics Identification Database.
https://www.ebi.ac.uk/pride/archive/projects/PXD040722

54. GSE225166. NCBI Gene Expression Omnibus.
https://www.ncbi.nlm.nih.gov/geo/query/acc.cgi?acc=GSE225166

55. GSE225576. NCBI Gene Expression Omnibus.
https://www.ncbi.nlm.nih.gov/geo/query/acc.cgi?acc=GSE225576

Sources for Supplementary Figs. 4–5

1. Hahn O. et al. Atlas of the aging mouse brain reveals white matter as vulnerable foci. Cell 186, 4117–4133.e22 (2023). doi:10.1016/j.cell.2023.07.027

2. Chen J. et al. LncRNA Lncbate1 promotes lipid synthesis in white adipose tissue during aging by targeting the miR-455-5p-ACSS1 axis. NPJ Aging 12, 156 (2026). doi:10.1038/s41514-026-00337-1

3. Chen Y. et al. Macrophage-derived CTSS drives the age-dependent disruption of the blood-CSF barrier. Neuron 113, 1082–1097.e8 (2025). doi:10.1016/j.neuron.2025.01.023

4. Liu P. P. et al. Neuronal cathepsin S increases neuroinflammation and causes cognitive decline via CX3CL1-CX3CR1 axis and JAK2-STAT3 pathway in aging and Alzheimer's disease. Aging Cell 24, e14393 (2025). doi:10.1111/acel.14393

5. Zuo T. et al. Macrophage-derived cathepsin S remodels the extracellular matrix to promote liver fibrogenesis. Gastroenterology 165, 746–761.e16 (2023). doi:10.1053/j.gastro.2023.05.039

6. Gasperoni J. G. et al. The role of PLAG1 in mouse brain development and neurogenesis. Mol. Neurobiol. 61, 5851–5867 (2024). doi:10.1007/s12035-024-03943-w

7. Sakai H. et al. Plag1 regulates neuronal gene expression and neuronal differentiation of neocortical neural progenitor cells. Genes Cells 24, 650–666 (2019). doi:10.1111/gtc.12718

8. Yang X. et al. PPM1H is down-regulated by ATF6 and dephosphorylates p-RPS6KB1 to inhibit progression of hepatocellular carcinoma. Mol. Ther. Nucleic Acids 33, 164–179 (2023). doi:10.1016/j.omtn.2023.06.013

9. Qi X. et al. Molecular basis of Wnt biogenesis, secretion, and Wnt7-specific signaling. Cell 186, 5028–5040.e14 (2023). doi:10.1016/j.cell.2023.09.021

10. Zhou Y. et al. Identification of MUP1 as a regulator for glucose and lipid metabolism in mice. J. Biol. Chem. 284, 11152–11159 (2009). doi:10.1074/jbc.M900754200

11. Gao R. et al. Secreted MUP1 that reduced under ER stress attenuates ER stress induced insulin resistance through suppressing protein synthesis in hepatocytes. Pharmacol. Res. 187, 106585 (2023). doi:10.1016/j.phrs.2022.106585

12. Bi J. et al. HSF2BP protects against acute liver injury by regulating HSF2/HSP70/MAPK signaling in mice. Cell Death Dis. 13, 830 (2022). doi:10.1038/s41419-022-05282-x

13. Zhang J. et al. Overexpression of HSF2 binding protein suppresses endoplasmic reticulum stress via regulating subcellular localization of CDC73 in hepatocytes. Cell Biosci. 13, 64 (2023). doi:10.1186/s13578-023-01010-w

14. Wang M. et al. SUMOylation-driven nuclear translocation of HSF2BP alleviates MASLD via COX6A1-dependent mitochondrial reprogramming. Cell Death Dis. 17 (2026). doi:10.1038/s41419-026-08935-3

15. Lui H. et al. Progranulin deficiency promotes circuit-specific synaptic pruning by microglia via complement activation. Cell 165, 921–935 (2016). doi:10.1016/j.cell.2016.04.001

16. Bishop E. S. et al. Age-dependent microglial disease phenotype results in functional decline in gut macrophages. Gastro Hep Adv. 2, 261–276 (2023). doi:10.1016/j.gastha.2022.09.006

17. Ishikawa H. et al. Effects of aging on diurnal transcriptome change in the mouse corpus callosum. iScience 28, 111556 (2025). doi:10.1016/j.isci.2024.111556

18. Ma J. et al. TYROBP in Alzheimer's disease. Mol. Neurobiol. 51, 820–826 (2015). doi:10.1007/s12035-014-8811-9

19. Zhang B. et al. Integrated systems approach identifies genetic nodes and networks in late-onset Alzheimer's disease. Cell 153, 707–720 (2013). doi:10.1016/j.cell.2013.03.030

20. Huang H. et al. The N6-methyladenosine RNA landscape in the aged mouse hippocampus. Aging Cell 22, e13755 (2023). doi:10.1111/acel.13755

21. Eugenin von Bernhardi J. et al. Oligodendrogenesis is a key process for cognitive performance improvement induced by voluntary physical activity. Glia 70, 1052–1067 (2022). doi:10.1002/glia.24155

Supplementary Files

This is a list of supplementary files associated with this preprint. Click to download.

- MethodsCompletev165.pdf
- Codev165.zip
- SourceDatav165.zip
- SupplementaryInformationv165.pdf